HIGH PRECISION SPECTROSCOPY USING STABILIZED FABRY-PEROT ETALON

(Corrected Copy)

A Thesis

Submitted for the Degree of

Doctor of Philosophy (Technology)

Submitted by

Tanya Das

Department of Applied Optics & Photonics

University of Calcutta

2021

To my Family,

Friends and Teachers...

List of Publications

1. **Refereed Journal Articles**

   (a) **Tanya Das**, Ravinder K. Banyal, T. Sivarani, B. Ravindra, *Development of a stabilized Fabry–Perot etalon based calibrator for Hanle echelle spectrograph*, Applied Optics, 59, 5464-5472, 2020. [1]

   (b) **Tanya Das**, Ravinder K. Banyal, *Method for tilt correction of calibration lines in high-resolution spectra*, Applied Optics, 60, 9906-9914, 2021. [2]

2. **Refereed Conference Proceedings**

   (a) **Tanya Das**, Ravinder K. Banyal, S. Kathiravan, T. Sivarani, Ravindra B., *Development of a stabilized Fabry-Perot based wavelength calibrator for precision Doppler spectroscopy*, Proc. SPIE 10702, Ground-based and Airborne Instrumentation for Astronomy VII, 107026A, 2018. [3]

   (b) **Tanya Das**, Ravinder K. Banyal, T. Sivarani, S. Sriram, *Using a passively stabilized Fabry-Perot etalon for determining instrumental artifacts in a spectrograph*, Proc. SPIE 11447, Ground-based and Airborne Instrumentation for Astronomy VIII; 1144748 (2020). [4]

---

[1] Presented in Chapter 1, Chapter 3, Chapter 4 and Chapter 5
[2] Presented in Chapter 6
[3] Presented in Chapter 3, Chapter 4 and Chapter 5
[4] Presented in Chapter 5

Presentations

1. **Tanya Das**, Ravinder K. Banyal, S. Kathiravan, T. Sivarani, B. Ravindra, *Development of a Fabry-Perot etalon stabilization system for Doppler Spectroscopy*, 36th Annual Meeting of the Astronomical Society of India (ASI), Osmania University, Hyderabad, 5-9 February 2018, Poster presentation.

2. **Tanya Das**, Ravinder K. Banyal, S. Kathiravan, T. Sivarani, Ravindra B., *Development of a stabilized Fabry-Perot based wavelength calibrator for precision Doppler spectroscopy*, SPIE conference on Astronomical Telescopes + Instrumentation, Austin, 2018, Poster presentation.

3. **Tanya Das**, Ravinder K. Banyal, Himal Bhatt, M. N. Deo, *Characterization of a Fabry-Perot calibrator with high resolution Fourier Transform spectrograph*, 7th International Conference in Perspectives of Vibrational Spectroscopy, BARC, Mumbai,2018, Poster presentation.

4. **Tanya Das**, Ravinder K. Banyal, T. Sivarani, S. Sriram, S. Kathiravan, *Using a stabilized Fabry-Perot etalon for determining instrumental artifacts in a spectrograph*, 38th Annual Meeting of the Astronomical Society of India (ASI), IISER, Tirupati, 13-17 Feb 2020, Oral presentation.

5. **Tanya Das**, Ravinder K. Banyal, T. Sivarani, S. Sriram, *Using a passively stabilized Fabry-Perot etalon for determining instrumental artifacts in a spectrograph*, SPIE conference on Astronomical Telescopes + Instrumentation (online), Dec 2020, Poster presentation.

Abstract

Accurate wavelength calibration is an important factor for any measurement with high resolution spectrographs. Stellar spectrum comprises of discrete absorption or emission lines whose position is precisely determined by calibrating the spectrographs using known reference lines generated from laboratory sources. For the spectrograph to measure small variations in Doppler shift, the wavelength calibration must be sufficiently stable during observation time. Instrument instability, mainly due to environmental factors like temperature and pressure variations, and limitations of traditional calibration methods, for example Th-Ar lamps, are the two challenges which limit high precision spectroscopy.

Through proper environmental control, by maintaining pressure at 1 mbar and temperature fluctuations at $\pm 0.05°$C, Fabry-Pérot etalons (FP) can yield a velocity precision of 1-10 m/s, when used for wavelength calibration. A passively stabilized FP based wavelength calibrator has been developed for Hanle Echelle Spectrograph (HESP) installed on the Himalayan Chandra Telescope (HCT). The etalon has been characterized using Fourier Transform Spectrograph (FTS) and tested with high resolution echelle spectrograph on Vainu Bappu Telescope (VBT). Initial test runs of the entire instrument with HESP have been conducted to study the performance of the FP instrument with the spectrograph.

Often, curvature and tilted lines are the observed artifacts in a high resolution spectra, arising due to the design of the respective spectrographs. Removal of these artifacts can help avoid wrong flux calculation and line centroid position misinterpretation, which can aid in a better prediction of the wavelength calibration model. As a part of this thesis work, a post processing technique for the correction of the observed curvature and tilt in the spectra has also been worked out. Curvature and tilt correction algorithm has been tested on the FP and Th-Ar calibration spectra obtained from different spectrographs.

Contents

List of Figures

List of Tables

Chapter 1

Introduction [1]

1.1 Introduction

Spectroscopy is a key method for monitoring and analyzing the physical and chemical properties of astronomical entities. Spectrographs are instruments used to observe the spectrum of astrophysical objects. It comprises of a slit, a collimating mirror, a dispersing element, a focusing setup, and a detector to record the spectrum. The light from the telescope is directed to the spectrograph using optical fibers through a slit, which is ultimately imaged onto the detector. Light through the slit is collimated and passed on to a dispersing element using a collimating mirror. A diffraction grating is used in most spectrographs, which disperses the light from the target object into its component wavelengths. The camera optics then focuses the dispersed light on to a charged coupled device (CCD), where it is recorded for further analysis.

In contrast to their low-resolution counterparts, high-resolution spectrographs employ echelle grating for use in higher diffraction orders, thereby providing more details about spectral features and giving a resolution of R =

---

[1] *Part of this chapter is published in Tanya Das et al., Applied Optics Journal 59, 2020.*

60,000 up to R = 150,000. Echelle gratings provide dispersion at higher angles and are blazed to concentrate maximum efficiency in a specific direction. At higher orders, they offer substantial overlap, causing the longer wavelength of a higher order to overlap with the following order's shorter wavelength. A cross-disperser, like a prism or a grating, is used to separate the overlapping orders.

Stellar spectra consist of both absorption and emission lines, whose precise position is determined by converting the pixels into the wavelength scale. This step is described as wavelength calibration, which utilizes known laboratory sources such as Th-Ar arc lamps for the purpose.

Measurement of the dark matter content of galaxies and their clusters (Napolitano *et al.*, 2010), estimation of the mass of stellar systems (Kelson *et al.*, 2000), determination of the age of old stars (A. Bik *et al.*, 2011), identification of chemical composition, temperature and other parameters by studying the strength of spectral features (Bhowmick *et al.*, 2020) and radial velocity measurements to determine the presence of planets around stars (Hatzes *et al.*, 2016) are the primary fields of application for spectroscopy.

1.2   Radial Velocity Method

The detection of extrasolar planet orbiting a main sequence star 51 Pegasi, in 1995 using Doppler Spectroscopy or Radial Velocity (RV) technique, is one of the most significant discoveries made in astrophysics (Mayor & Queloz, 1995). Since then, technological advancement has led to improved high precision photometric and spectroscopic techniques for detection of planets. To this date, the number of confirmed planets have crossed 4420 count from various ground based observations and space missions[2]. The RV technique is a powerful tool that contributed in many exoplanet discoveries before transit data from NASA's Kepler mission and later from Transiting Exoplanet Survey

---

[2]NASA Exoplanet Archive

Satellite (TESS) became available. High precision radial velocity technique measures the Doppler shifts in the spectrum of the star. Apart from detection of extra solar planets, this technique finds application in areas such as, detection of g-mode oscillations in the Sun (Appourchaux *et al.*, 2010), investigating expansion rate of the universe (Liske *et al.*, 2008), measuring variability of fundamental constants (Reinhold *et al.*, 2006), study of stellar interiors using astro-seismology (Bazot *et al.*, 2007) and characterization of binary and pulsating stars (Butler *et al.*, 2003).
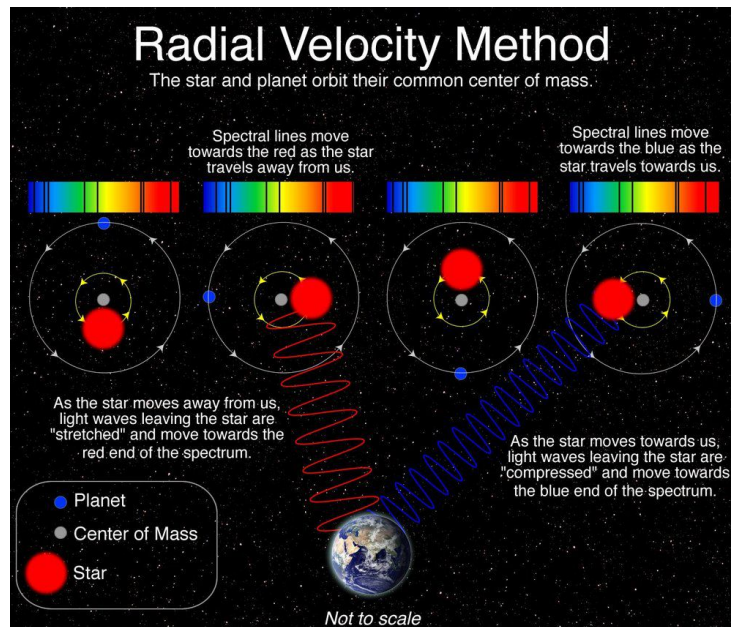
Figure 1.1: Radial Velocity method for detection of an orbiting planet around the star. Credit: Las Cumbres Observatory

The concept behind using radial velocity measurements in extrasolar planet detection is shown in Fig. 1.1. In a gravitationally bound system, the star-planet pair orbits their common center-of-mass. Hence, the star is not completely stationary and appears to wobble slightly, causing a wavelength shift in the spectrum. The spectrum appears red or blue shifted depending upon the movement of star away from or towards us. If there are periodic wavelength shifts in the star's spectrum, it ascertains the presence of an invisible companion around the star. The amplitude of the wavelength shift

depends on the mass and distance of the planet from the host star and the inclination angle that orbit makes with observer's line of sight. This method helps in determining the eccentricity, semi-major axis, orbital period and the minimum mass of the orbiting planet.

Doppler shifts can be converted into radial velocity using the following equation,

$$\frac{V_{RV}}{c} = \frac{\Delta\lambda}{\lambda} \, , \tag{1.1}$$

where, V_{RV} is the radial velocity, c is speed of light, λ is the wavelength in the rest frame and $\Delta\lambda$ is the change in wavelength due to Doppler motion.

The RV signal is usually small due to high mass ratio between the star and the planet. For example, a Jupiter-size planet would induce a radial velocity shift of 11.2 m/s in the spectra of a sun-like star from an orbital distance of 5.4 AU, while an Earth-sized object at 1 AU would induce a shift of $\sim$10 cm/s (Hatzes *et al.*, 2016). In case of binary systems, due to large mass of orbiting stars, the radial velocity variation of several kilometers per second are easily observed. Highly stable spectrographs dedicated to planet search programs have been able to reach a Doppler precision of 1 m/s, allowing detection of super earths ($5 - 8$ $M_\oplus$) (Dittmann *et al.*, 2017).

1.3   Wavelength Calibration

A charge coupled device (CCD) is used for recording the spectra of star after dispersion from spectrograph grating. However, the CCD doesn't record the wavelength but only the intensity information. Stellar spectrum consists of series of discrete absorption and emission lines produced due to a variety of chemical compositions and physical conditions prevailing in the star. The wavelength position of these lines can be precisely determined by referencing the spectrograph with known lines generated from laboratory sources like hollow cathode lamps (Bauer *et al.*, 2015). The spectral intensity is recorded

as a function of pixel position on a 2D grid. Grating being a non-linear device requires correct wavelength to be assigned to each pixel position on the CCD grid and hence the calibration is done by using a well characterized laboratory source. An empirical relation, known as wavelength solution, is used to map a discrete wavelength to each pixel position. This process is called wavelength calibration, whose accuracy is of paramount importance for any measurement with high resolution spectrographs.

The wavelength calibration must be sufficiently stable during observation time to measure small variations in Doppler shift. Environmental fluctuations can easily induce errors of few 10-100 m/s in the spectrograph data. Even if the environmental variations are controlled, wavelength calibration errors would still remain (Halverson *et al.*, 2016). A meaningful comparison of the spectra taken at different times is often a difficult and non-trivial task. These challenges have inspired researchers to build highly stabilized spectrographs and explore innovative wavelength calibration techniques. Traditional techniques using emission lamps such as Th-Ar or advanced techniques such as Fabry-Perot (FP) etalon (Wildi *et al.*, 2010), Iodine cell (Marcy & Butler, 1992), and laser frequency comb (Murphy *et al.*, 2007) are the methods that are commonly used for wavelength calibration.

1.4 Methods of wavelength calibration

1.4.1 Emission lamps

Emission lamps are the traditionally used technique of wavelength calibration, Thorium-Argon (Th-Ar) lamp being the most widely used since they provide a wide wavelength coverage from UV to NIR. Hollow cathode lamps produce a dense set of emission lines, which can be used as a wavelength calibration source to generate wavelength solution models. Bright lines created by the lamp's lighter fill gases can be used to calibrate wavelengths with moderate

precision, but they cause significant error in high resolution equipment that require high precision calibration. Emission lamps do not provide a homogeneous line distribution and intensities, the density and relative strength of these lines leading to blending. Thorium does not have enough bright lines in the NIR region, whereas Argon emission lines can saturate the detector during typical exposure periods. High susceptibility of Argon lines to ambient condition (Lovis *et al.*, 2006), along with spectrum contamination from different sources and aging of the lamp, further adds to the disadvantages. The uncertainty in determining line positions in a Th-Ar spectrum is estimated to be around 10 m/s (Lovis & Pepe, 2007). When used in simultaneous calibration, the RV precision achievable with emission lamps can be improved, attaining sub-m/s precision in spectrographs like HARPS (Lovis *et al.*, 2006). Fig. 1.2 shows an example of Th-Ar spectra taken from Hanle Echelle Spectrograph (HESP).
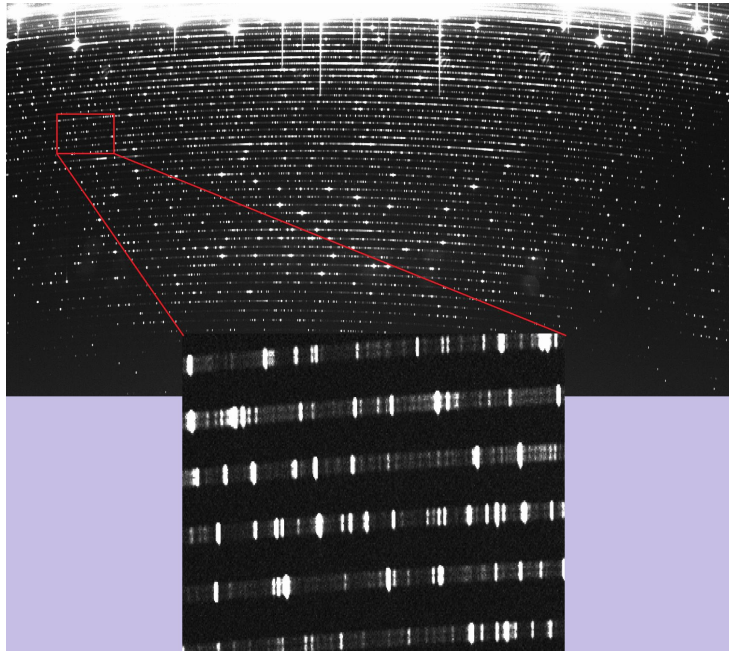
Figure 1.2: Th-Ar calibration spectra taken with HESP, showing the over-saturated and blended lines.

1.4.2 Molecular Absorption Cells

Iodine absorption cell technique was developed for precision spectroscopy by Marcy & Butler (1992). The iodine gas exhibits absorption features between 500-600 nm and is transparent in the rest of the star's spectrum. Simultaneous calibration using molecular iodine (I_2) can achieve a RV precision of a few m/s (Butler *et al.*, 1996). When incident starlight passes through a temperature-controlled absorption cell, a dense forest of I_2 molecular lines is imprinted on the stellar spectrum. Along with simultaneous wavelength calibration, this method also allows for determination and correction of instrumental drifts. Iodine absorption cells provide a very narrow wavelength coverage (500-630 nm). This technique also suffers from disadvantage of loss of light within the absorption cell. Disentangling iodine lines from stellar absorption lines also present as a challenge and requires complex modelling for de-convolution and retrieval of small Doppler shifts. Fig. 1.3 shows an example of iodine lines imprinted on solar spectra, obtained from high resolution Echelle spectrograph at VBT.
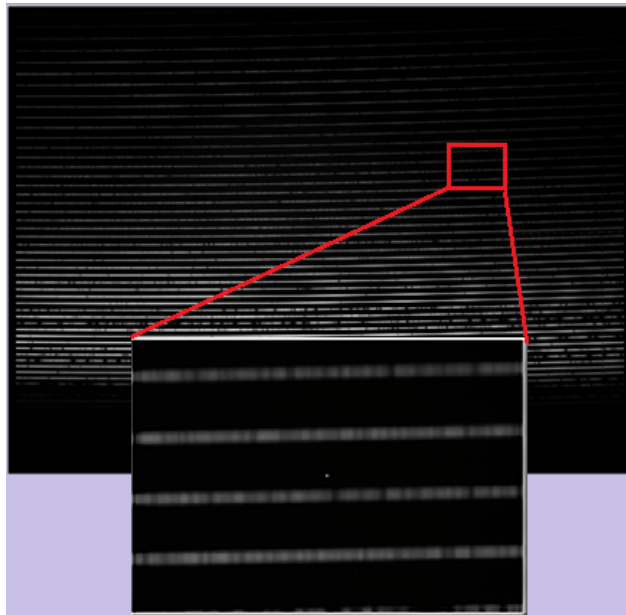
Figure 1.3: Solar spectra taken with VBT, with iodine lines imprinted on it. Credits: C. Sireesha (2019)

1.4.3 Laser Frequency Comb

A frequency comb is a state of the art technology, using a laser to generate spectrum consisting of discrete and equispaced frequency lines. Sharp emission lines are produced by LFC at frequencies that can be traced to a stable atomic transition. LFC is tuneable and can generate a large number of equidistant calibration lines of equal intensity. The frequency of the produced comb is stabilised by locking the absolute frequency and the laser repetition rate to a GPS-stabilized atomic clock. Using LFC as a wavelength reference, RV precision of the order of a few cm/s can be attained. LFC is promising technology but it comes with high costs and many operational difficulties since it is not just a turnkey instrument. The complexity of the design further limits the use of frequency combs. Another disadvantage of LFC is the difficulty to design a comb that can span the entire optical and NIR ranges while remaining stable over long time intervals. Output from a laser frequency comb is shown in Fig. 1.4.
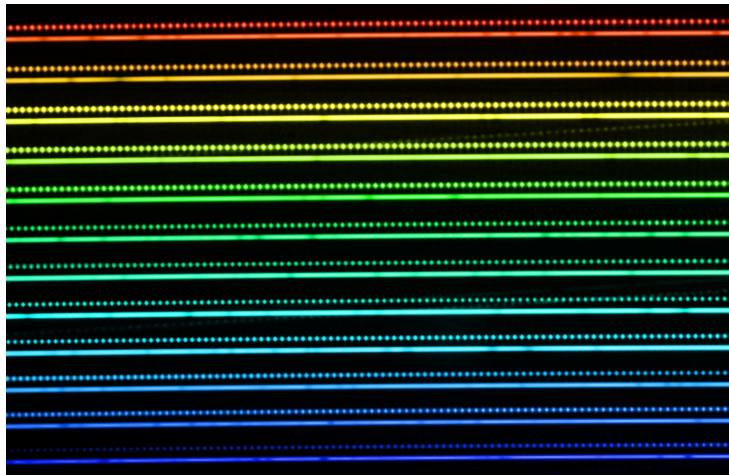
Figure 1.4: Laser Frequency Comb spectrum (top) with stellar spectrum of HD75289 (bottom) taken using HARPS. Credits: ESO

1.4.4 Fabry-Pérot Etalon

Fabry-Pérot (FP) etalon is a simple optical component that work on the principle of multiple beam interference. The output from the FP is a collection of interferometric Airy peaks that have been filtered from a broadband continuous source. Providing stable spectrum for referencing with nearly equispaced lines of uniform intensity and easily matched wavelength range of the spectrograph, FP etalon can give frequency comb-like properties at affordable costs and less complexity. FP etalons can help in achieving RV precision of a few cm/s with suitable environmental control. The disadvantage of using FP etalon for calibration is the lack of absolute referencing, which can be overcome by using external absolute reference like simultaneous calibration with Th-Ar lamps or laser. Aging of etalon spacers and coating degradation over time can cause intractable frequency drifts in a passively stabilized etalon, which can be actively tracked by locking the FP cavity with a frequency stabilized diode laser. FP calibration frame taken from HESP is shown in Fig. 1.5.
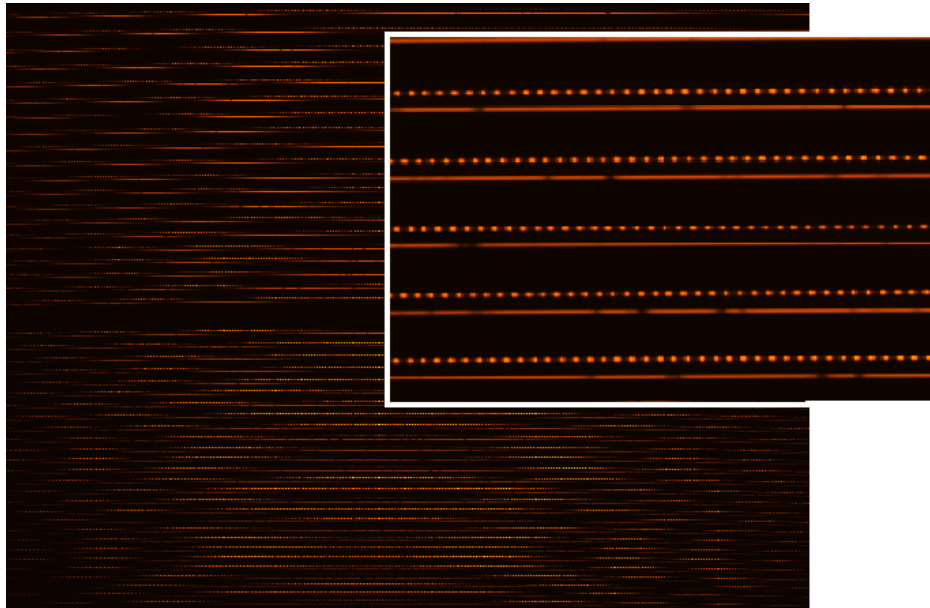
Figure 1.5: Raw spectrum recorded by HARPS in dual fiber mode. Upper fiber is illuminated by Fabry-Perot based calibration source (top spectrum) and lower fiber is illuminated by star (bottom spectrum) Credits: Cosentino *et al.* (2012)

1.5   Advantages of using Fabry-Pérot etalon

Instrument instability, induced by environmental factors like temperature and pressure variations, photon noise and limitations of traditional calibration methods are the major challenges to high precision spectroscopy, which together might account for errors of few hundreds of m/s (Murphy *et al.*, 2007). Even with a stabilized spectrograph, wavelength calibration can contribute to an error of around 11.5 cm/s (Halverson *et al.*, 2016). Although Th-Ar lamps are an affordable source of reference, they cannot be employed in the NIR with the same efficiency as they can be in the optical region. The lines provided are not evenly distributed across all orders, their brightness varies widely, and they suffer from line blending and spectrum contamination from different sources. The uncertainty in determining line positions in a Th-Ar spectrum is estimated to be around 10 m/s (Lovis & Pepe, 2007). Iodine cells provide a very limited wavelength range of operation and requires complex methods for post processing and reduction of the data. Laser frequency combs are ideal wavelength calibrators, but they have the disadvantage of having a narrow wavelength coverage, as well as being expensive and complicated to design. FP etalons are a less expensive and less complicated method that provides frequency comb-like properties.

Another important advantage of FP over traditional emission lamps is the large number of lines provided by the former. This is significant because the error in determining radial velocity drift (σ_{RV}) is,

$$\sigma_{RV} \propto (\sqrt{SNR})(\sqrt{No.\ of\ lines})\,, \qquad (1.2)$$

where, SNR is the signal to noise ratio of the data and no. of lines indicate the number of calibration lines available for marking the wavelength.

Resolution of a spectrograph is given by Equation 1.3

$$R = \frac{\lambda}{\Delta\lambda}\,, \tag{1.3}$$

where, λ is the wavelength.

Taking the example of HESP with a resolution of R=60000, at $\lambda = 6000$Å, Equation 1.3 gives $\Delta\lambda = 0.1$Å. This is covered in 2 pixels and corresponds to a RV shift of 5 km/s in HESP. This implies that a shift of 10 m/s will correspond to a shift of 0.004 pixels for a single line. Assuming an SNR of 1, having 500 lines for wavelength calibration can induce an error of 4.5% in measuring 0.004 pixel shift. If 5000 lines are available for calibrating the wavelength, then this error gets reduced to 1%, according to Equation 1.2. In our analysis, we have detected 6624 lines of FP across 22 orders of HESP, whereas the number of usable lines of Th-Ar detected in the same range were 854. Hence, we are using FP etalon as a source for wavelength calibration due to the numerous advantages offered by it. The aim is to attain RV precision of 10 m/s with HESP, across the visible wavelength range over the observation run ($\sim$10-12 hours).

The objectives of the thesis are as follows:

- Investigating the factors important to obtain a stable output from the FP that can be used for precise measurements.

- Development of a passively stabilized Fabry-Pérot based wavelength calibrator for HESP, in which the FP etalon, along with the illumination and collection optics will sit inside an evacuated and temperature controlled chamber.

- In comparison to the traditional calibration techniques, this method will be used in analysing design induced errors of the spectrograph, which can help in eliminating instrument artifacts like curvature and tilt in spectra.

- With space based mission like NASA's new all sky transit survey satel-

lite TESS, and older programs like Kepler, many extrasolar planets around bright stars have been detected. The ground based RV follow up observations is required to determine the mass and other important orbital parameters of new exoplanets. The FP instrument will act as an add-on calibration module for HESP to tap into the RV capabilities of the spectrograph and facilitate regular science observation.

1.6 Thesis outline

The thesis is divided into the following chapters. An overview of the contents of each chapter is presented below.

Chapter Two: Fabry-Pérot etalon for wavelength calibration

Fabry-Pérot is an optical component that works on the principle of multiple beam interference. In this chapter, the working of FP, types of FP, the applications apart from use in wavelength calibration, are discussed. The basic optical construction of FP is also discussed and the various terms associated with FP that will be used throughout the thesis, have been defined here. Existing observational facilities that use FP etalon based wavelength calibration system for their spectrographs have been mentioned here and the details of the FP setup design used by them is presented. Finally the design differences of our setup from the existing ones are summarised at the end of the chapter.

Chapter Three: Factors affecting Fabry-Pérot Etalon stability

The main requirement of using FP for wavelength calibration is that it should provide a stable output over the observation time period. To ensure the same, the factors that can cause fluctuations in the output of FP are studied in detail and presented in this chapter. Both pressure and temperature changes can cause the FP lines to shift and induce error in calibration. It is also important to illuminate the FP with a collimated beam of light, failing which the performance of the same is affected. Misalignent in fiber or finite fiber size lead to a divergence in the input light, causing errors in FP line position and

a loss in finesse. The acceptable values for each factor have been calculated to keep RV errors within the desirable limit. The requirements on the design of the FP based instrument has been summarised in this chapter.

Chapter Four: Design of instrument

Based on the design requirements discussed in previous chapter, the final design of the instrument is presented here. Different aspects of the design is described in detail. Pressure stability is achieved by operating the FP setup in a vacuum chamber. Temperature stability is achieved by using a temperature controller and proper insulation. The pressure and temperature limits achieved have been tested in the laboratory and the results have been presented in this chapter. The design of the optical feedthrough developed in house is discussed in detail. The opto-mechanical design of the setup is shown along with details about the optical components like lenses, fibers and light source used in the setup. The specifications of the FP being used in the setup is also given in this chapter.

Chapter Five: Performance test of Fabry-Pérot

The FP setup has been tested with three different spectrograph. Fourier Transform Spectrograph (FTS) has been used to test the various parameters of the FP like Free Spectral Range(FSR), finesse and cavity length. The detailed analsysis of the data obtained from the test is presented. The optical setup used for illumination of FP and light collection has been tested with the Echelle Spectrograph on VBT. The problems in collimation were observed and corrected with the help of results obtained from this test. The entire calibration setup, with pressure and temperature control, have been installed and tested on HESP. The results from the tests provided further insights on the instrument artifacts of the spectrograph. Analysis and results from all the three tests have been summarised and presented in this chapter.

Chapter Six: Curvature and tilt correction of high resolution spectra

Results from the FP spectra taken with HESP, showed an increase in the

line-width of the FP lines. On further analysis, the instrument artifacts were found to be one of the reasons behind it. Even though HESP design does not induce significant tilt in the spectra, the curvature of the orders introduces small tilt in the FP lines. If not taken care of in post-processing, the tilted line can lead to error in flux and wavelength caibration, along with reduction in spectral resolution. This was taken as a motivation to develop a simple algorithm to correct the curvature and tilt in spectra during post-processing. The algorithm of the code developed for this purpose is presented here (not made open-source yet). The results from application of the said algorithm on HESP data and improvement in the line-width is also shown. In order to benchmark the algorithm, data from spectrographs with tilted spectral lines were taken and the algorithm was applied on them. X-shooter and MIKE spectrographs are two such spectrographs know for their highly curved orders and tilted lines. The results from these spectrographs before and after performing the correction algorithm is shown for the purpose of comparison. Discussion on the importance and need of such corrections have been done in this chapter.

Chapter Seven: Summary and Future Work

The work done in the thesis and the results obtained have been summarised in this chapter. The future possibilities of this work have also been discussed in brief here.

Chapter 2

Fabry-Pérot etalon for wavelength calibration

2.1 Introduction

Interference is the phenomenon in which two or more waves having a phase difference interact, resulting in a consequent wave with a greater, equal, or lower amplitude. An interferometer is a device that allows light beams to interfere with one another. The interference pattern produced by local variations in phase difference across the beam's cross-section is known as interference fringes.

2.2 Multiple Beam Interference

When two coherent beams are combined based on their phase difference, an interference pattern is formed. Multiple beam interference occurs when multiple reflections of mutually coherent beams superimpose, which can be accomplished by placing glass plates with high reflection coating in close proximity (Hecht, 1975). Each time the light reaches the second surface,

a portion of it is transmitted, and the remainder is reflected, resulting in multiple offset beams that can interfere with one another. The intensity drops with each reflection following the reflectivity of the surface, and thus the final amount of light collected at the output is dependent on the reflectivity. The greater the number of multiple reflections of the beams, the finer and sharper are the resulting fringes. As a result, in multiple beam interferometry, the line-width of the interference fringes becomes extremely narrow. Because of the large number of interfering rays, an interferometer with extremely high resolution is produced.

2.3   Fabry-Pérot interferometer

A Fabry-Perot interferometer is a simple optical component made up of two reflecting surfaces that face each other and form the interferometer's cavity. It was developed in 1899 by Charles Fabry and Alfred Pérot (Pérot & Fabry, 1899) and works on the concept of multiple-beam interference. An FP interferometer is a device that allows the gap between the glass flats to be varied by mechanically moving one of the plates. An FP etalon is made up of glass flats that are fixed to a spacer material.

Based on the geometry of the cavity plates used for the construction, the FP interferometer can be plane-parallel, confocal, concentric or plano-concave. Apart from the shape of the cavity mirrors used, the FP can be classified into the following types:

- **Solid Fabry-Pérot:** A high reflectivity coating applied on the either sides of a glass window can form a solid cavity that can trap light. The effective cavity length is nL where n is refractive index of the glass material and L is thickness of the window. It is a rugged and compact setup that can be temperature tuned. Solid Fabry-Perot has several drawbacks, including material dispersion, coating mismatch, poor temperature stability and limited available thickness.

- **Air spaced Fabry-Pérot:** These etalons consist of two parallel plates with an air gap in the middle forming an air cavity with an effective cavity length of nd where n is refractive index of air and d is the distance between the plates. They are larger setups that can be tilt or pressure-tuned. They are less rugged as compared to solid FP but have superior thermal stability and better effective finesse. The mirrors are simultaneously coated to avoid any mismatch. Alignment of the reflecting surfaces is critical.

- **Fiber Fabry-Pérot:** A Fiber Fabry-Pérot is directly made from optical fibers and hence it is pre-aligned. Because of this, alignment issues are minimal, albeit material dispersion and birefringent properties can cause complications. Another issue with FFP is the small light output due to inefficient light coupling into single-mode fibers.

FP interferometers and etalons find application in a wide range of fields. In telecommunication, FP is used for wavelength division multiplexing (J. Yin *et al.*, 2013). FP is also used in the biomedical industry for ultrasound detection (H. Varu, 2014). In industrial and aeronautical instruments, FP is used for vibration sensing (Gangopadhyay, 2004) and strain measurements (S. Liu *et al.*, 2014). FP based sensors can also be used in temperature sensing (Choi *et al.*, 2008) and humidity sensing (D. Su *et al.*, 2013). Etalons can also be used for narrow-band imaging of extended objects in astronomy (S.K. Dhara *et al.*, 2016). Etalons are used in high-resolution spectroscopy as an optical spectrum analyzer and as dichroic filters in optical instruments such as cameras and light sources. FP based sensors can also be used to measure the chemical composition of liquid materials by changing the refractive index of the cavity (T. Wei *et al.*, 2008; Zhang *et al.*, 2010). In laser physics, FP finds application in controlling the line-width of the laser (Peterson & Yariv, 1966), for frequency stabilization of laser (Pan *et al.*, 2011) and for constructing single-mode lasers as optical resonators (Elkin & Napartovich,

1994). FP interferometers are also being used in gravitational wave detectors LIGO and Virgo for boosting the sensitivity (Abbott *et al.*, 2016).

2.4   Construction and working of Fabry-Pérot

A Fabry-Pérot etalon is an optical component consisting of two glass plates mounted parallel to each other, separated by a certain distance, with inner surfaces having high reflection coating (Born & Wolf, 1980). The reflecting surfaces are usually made of fused silica. The outer surfaces have anti-reflection coatings along with wedged plates to avoid reflection from outer surfaces. The two glass plates form a resonant cavity and produce a periodically varying transmission function due to the interfering multiple reflections of light in the cavity. The cavity length in an interferometer can be varied by using a piezoelectric device to change the position of one mirror. Because the glass plates are mounted on a spacer made of material with a low thermal coefficient of expansion, such as Zerodur or ULE glass, etalons have a fixed cavity spacing. A diagram representing the simple construction of an etalon is shown in Fig. 2.1.

The operation of an etalon according to multiple beam interference is shown in Fig. 2.2. The light is incident on the first mirror, part of which is reflected and the rest transmitted. The transmitted light is reflected by the second mirror placed at a distance d from the first.

The beam is reflected multiple times between the mirrors and is only transmitted out of the cavity when a specific condition for constructive interference is met. Otherwise, destructive interference suppresses the light almost completely. When a diverging or converging light passes through FP plates, it produces concentric rings as an interference pattern, corresponding to the light rays entering the FP at different angles. These sharp fringes are referred to as Haidinger rings or fringes of equal inclination.

If the cavity's refractive index is assumed to be n and there is no light ab-
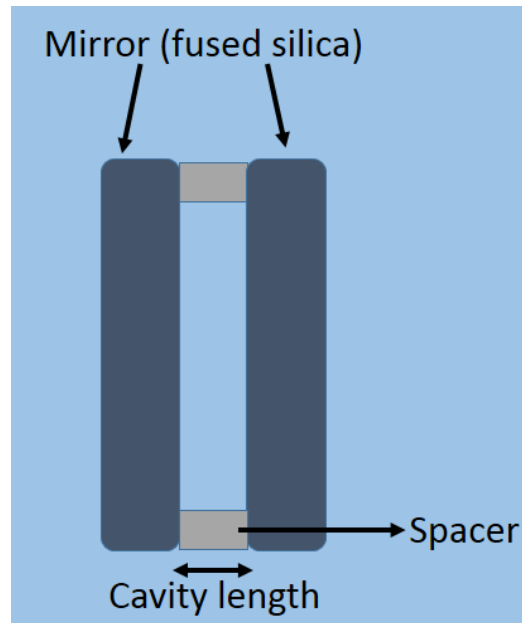
Figure 2.1: Illustration depicting the basic construction of a Fabry-Pérot etalon.
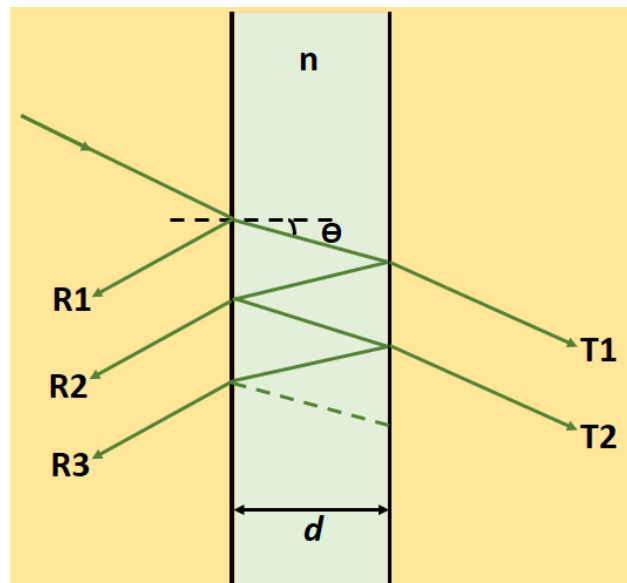
Figure 2.2: Multiple beam interference within a Fabry-Pérot etalon.

sorption by the mirror, light can only be transmitted outside the cavity when all reflected waves are in phase, and the resonance requirement is fulfilled, which is given by Equation 2.1.

$$nd\cos(\theta) = m\lambda/2 \, , \qquad (2.1)$$

where, m is the interference order number, and θ is the angle of incidence on the second surface, d is the cavity length, and λ is the wavelength.

The phase difference (δ) required for constructive interference is given by Equation 2.2.

$$\delta = \frac{4\pi n d \cos(\theta)}{\lambda} \qquad (2.2)$$

2.5 Fabry-Pérot Parameters

In this section, we define the FP parameters and characteristics that will be used throughout the thesis.

2.5.1 Fabry-Pérot transmission function

Interference between multiple light reflections between the two reflecting surfaces results in a varying transmission function, which is represented by Equation 2.3.

$$I_T = \frac{I_0}{1 + F sin^2(\delta/2)}, \qquad (2.3)$$

where,

$$F = \frac{\pi\sqrt{R}}{1 - R}, \qquad (2.4)$$

Here, F is coefficient of finesse, R is mirror reflectivity, n is refractive index of cavity and δ is the phase difference as defined by Equation 2.2.

The transmitted intensity is a periodic function of δ and the maximum and minimum values are obtained according to Equation 2.5,

$$\begin{aligned} [I_T]_{max} &= I_0; & \delta &= m\pi \\ [I_T]_{min} &= \frac{I_0}{1 + F}; & \delta &= (m + 1/2)\pi \end{aligned} \qquad (2.5)$$

where, m is an integer.

As the mirror reflectivity (R) increases, the peaks become narrower. A high reflectivity coating of >90% produces sharp cavity lines, but it can be realized only over a small wavelength range. The variation in cavity lines with different values of R is depicted in Fig. 2.3.
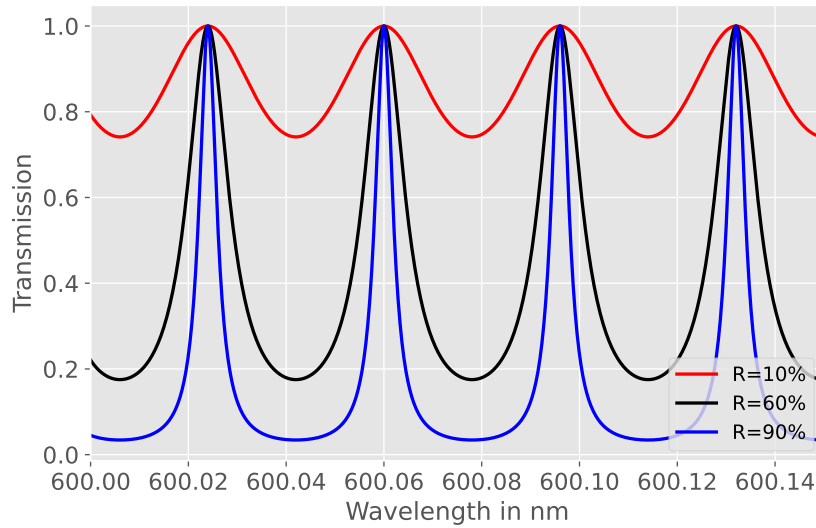
Figure 2.3: Simulated curve of Fabry-Pérot transmission function for different values of reflectivity coating R. As the R increases, the FP transmission peaks become sharper.

The transmission spectra of FP with a cavity length of d=5 mm and different reflection coating values has been simulated, as shown in Fig. 2.4.

2.5.2 Free Spectral Range

Free Spectral Range (FSR) is defined differently for a spectrograph and for FP. In case of a spectropgraph, FSR is the wavelength range in a spectral order without overlap from the adjacent orders. FSR of an etalon is the separation between the neighbouring transmission peaks, measured in optical frequency or wavelength. It is a parameter used in the characterization of the FP interferometer/etalon. The FSR has been marked in Fig. 2.4. FSR is inversely proportional to the refractive index of the cavity medium and the cavity length.

FSR in terms of frequency is given as:
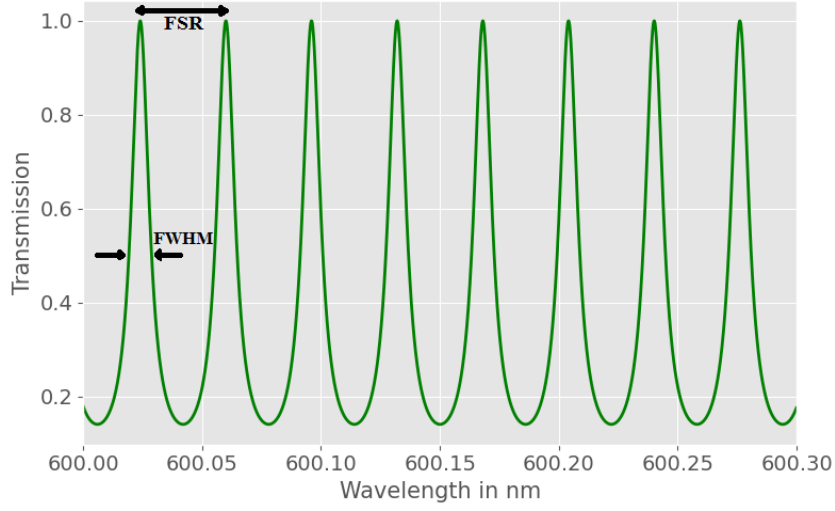
Figure 2.4: Transmission spectra of the Fabry-Pérot simulated over a short wavelength range. FSR is the free spectral range of the FP, and FWHM is the line-width.

$$FSR = \Delta\nu = \frac{c}{2nd}, \tag{2.6}$$

where, c is speed of light, n is refractive index of cavity and d is the cavity length.

FSR can be expressed in terms of wavelength (λ) as,

$$FSR = \Delta\lambda = \frac{\lambda^2}{2nd}. \tag{2.7}$$

2.5.3 Finesse

Finesse is a quantitative measure of the etalon's ability to resolve closely spaced transmission peaks. It is a term used to describe the resolution of the etalon. Finesse describes the width of the peak and provides information about the sharpness of the maxima. Finesse can be defined as the ratio of the separation between fringes, i.e. the free spectral range to the resonant peak's full width at half maximum (FWHM), as given in Equation 2.8. The FWHM of the transmission peaks of FP is shown in Fig. 2.4.

$$F = \frac{FSR}{FWHM} \tag{2.8}$$

The reflectivity R of the cavity mirrors can also be used to characterize finesse, as shown in Equation 2.9.

$$F = \frac{\pi\sqrt{R}}{1 - R} \tag{2.9}$$

Because the surface of the mirrors cannot be made perfect reflective, a peak with zero width, or a delta function for the transmission peaks, cannot be obtained, thereby limiting the resolution of the FP.

2.5.4 Resolution

The resolution of an etalon is defined as the minimum wavelength separation that the instrument can resolve. For the two peaks to be fully resolved, the separation between them must be at least equal to the full width at half the maximum of the peaks, thereby satisfying the Rayleigh criterion. The chromatic resolving power is defined as the ratio of wavelength to the least resolvable wavelength difference. The resolving power of FP is given by Equation 2.10.

$$R = \frac{\lambda}{\Delta\lambda} \tag{2.10}$$

2.6 Using Fabry-Pérot etalon in wavelength calibration

A wavelength calibrator based on FP etalon should have the following characteristics (Wildi *et al.*, 2010):

- FP can provide a stable reference spectrum and achieve 1-10 m/s RV stability precision.

- It should be designed to cover the full wavelength range of the spectrograph.

- Lines of nearly uniform spacing and intensity are obtained.

- FP lines should not be resolved by the spectrograph.

- For optimal sampling, the free spectral range of the FP can be designed to be 3–4 times the FWHM of spectrograph resolution. Narrow spacing gives poor contrast, whereas wider spacing leads to imperfect sampling.

- As the free spectral range is a function of cavity length, etalons can be manufactured to match the specification of the spectrograph.

A Fabry-Pérot based setup can act as an excellent wavelength calibration source for the spectrograph by providing continuous lines of uniform intensity. The transmission lines of the FP can be marked for wavelength by taking consecutive Th-Ar frames or using Th-Ar in simultaneous calibration. Another method for generating the wavelength solution model for FP lines is to use FTS spectra to determine the absolute interference order. The FP needs to be operated in a temperature-controlled vacuum chamber, which is termed passive stabilization. The output from the chamber can then be carried to the spectrograph calibration unit using optical fibers. Hence the FP based setup acts as a standalone system. This is an addition to the spectrograph, which can be easily incorporated without making any significant changes in the spectrograph design itself.

2.7 FP based calibration system designs used in existing facilities

2.7.1 CARMENES Spectrograph

Calar Alto high-Resolution search for M-dwarfs with Exo-Earths with Near-Infrared & optical Echelle Spectrograph (CARMENES) is an infrared planet-hunting spectrograph on the Calar Alto 3.5 m telescope with a spectral resolving power of R=82,000 (Quirrenbach *et al.*, 2010). This spectrograph aims to study mid to late M-dwarfs as they show an increase in the flux in Near Infrared Region (NIR). Since the spectrograph operates in the NIR region, Th-Ar lamps cannot be efficiently used due to the fewer number of lines it offers in this region, along with the other disadvantages discussed in section 1.4.1. Hence, FP provides a good alternative for wavelength calibration. Two passively stabilized FP etalons are used as reference calibration modules: 550-1050 nm for red visible wavelength range (FP1) and NIR region spanning 900-1700 nm (FP2). Both the FPs are optimized for operation in the separate arms and can produce 15000 lines of nearly homogeneous intensities in each arm. The FPs have been stabilized to achieve an RV precision of 10 cm/s in both arms.

The design of the setup used in both the arms is identical (Schäfer and Reiners, 2012). The FPs used are manufactured by SLS Optics. FP1 is optimized for 600-1000 nm wavelength range with a Zerodur spacer and cavity length of 9.990 mm with a wedge angle of 30 arcmin. FP2 is optimized for operation in 900-1300 nm wavelength range with Zerodur spacers and a cavity length of 12.334 mm. Effective finesse for both the FPs is 8 with FSR~0.03 nm. A halogen lamp is used as a light source, covering the entire wavelength range for both the arms and providing sufficient flux. Multimode fibers are used in the setup, which provides many different modes of transmission for light inside the fiber. Any movement or stress in the fiber can lead to

changes in the mode and hence, a change in the shape and position of output light. Using a very bright light source with smaller diameter fibers eliminates the need for using a scrambler for stabilizing the light output. An input fiber of 50 μm core diameter is used for illuminating the FP, the light from which is collimated using a parabolic mirror that directs the light through the FP. On the output side, a similar mirror is used to collect the light and couple it into the output fiber of 200 μm core diameter to ensure less light loss at coupling points. The mirrors used to allow direct plug-in of the fibers eliminating the need for any further alignment. An angular stability of $0.0015°$ is maintained. The output fiber carries the light into the spectrograph calibration unit. The entire FP unit is depicted in Fig. 2.5.
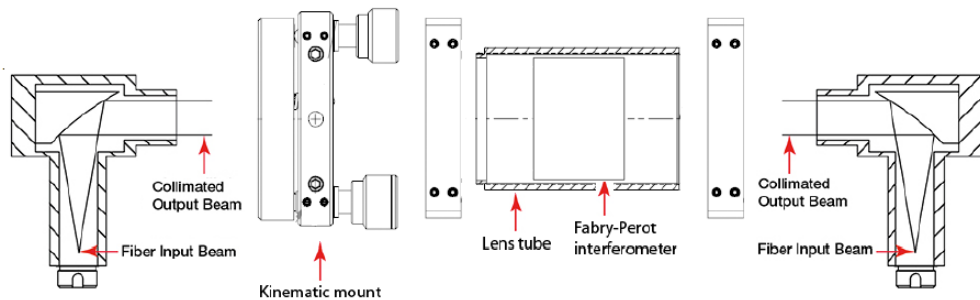
Figure 2.5: Sketch of the optical setup used for illumination and collection of light from FP etalon. Credits: Schäfer and Reiners (2012)

The FP unit is placed inside a vacuum tank to provide temperature and pressure stability. An optical stage with three legs, as shown in Fig. 2.6, holding the FP and parabolic mirrors, is used for mounting inside the tank. Fiber feedthroughs used in the setup are custom made designs with one fiber crossing through the feedthrough. The FP unit is operated at a pressure of 3×10^{-6} bar using Pfeiffer's HiPace300 Turbo Pump and Duo2.5 backing pump. Pfeiffer Pirani Gauge PKR251 is used for measuring the pressure inside the tank. The vacuum tank has two layers with a gap between which silicon oil coolant is pumped using a thermo-pump. The coolant temperature is controlled using Huber Ministat 230, which maintains the temperature at 15°C

with a stability of 15 mK. PT100 sensors with Lakeshore 224 temperature monitor are used for measuring the temperature. The coolant temperature is controlled, thereby adjusting the temperature of the vacuum tank to the coolant temperature and ensuring uniformity within the tank.
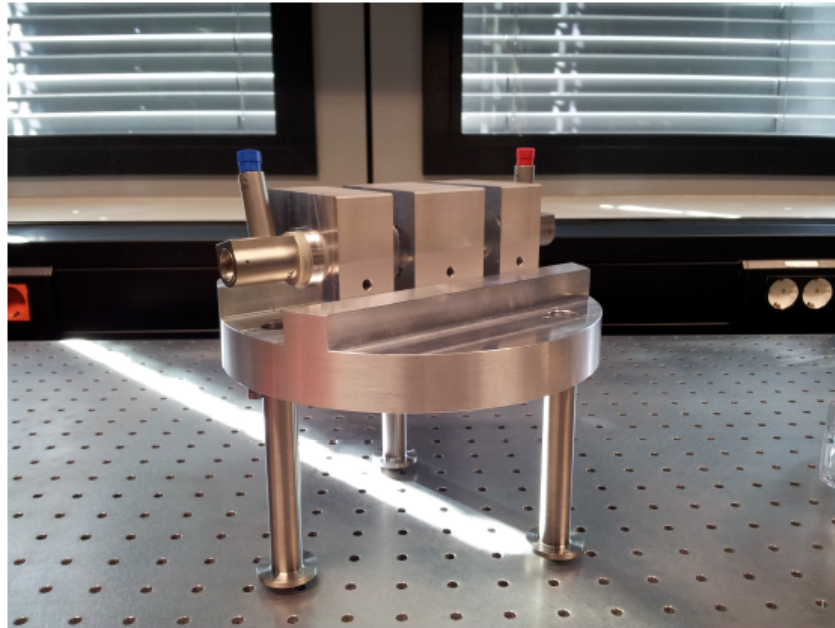
Figure 2.6: The optical bench holding FP and relaed optics, that is finally mounted inside vacuum enclosure for CARMENES. Credits: S. Schäfer (2014)

2.7.2 TRES Spectrograph

A passively stabilized FP etalon based calibration system is installed on Tillinghast Reflector Echelle Spectrograph (TRES) at the 1.5 m Tillinghast telescope in Fred Lawrence Whipple Observatory (FLWO). The spectrograph has a resolution R=45,000 and spans a wavelength range of 3800-9000 Å. Off the shelf, components have been used to construct an economic FP calibrator that can be developed on a smaller budget, suitable for small observatories, with the aim of reaching m/s level of accuracy in RV measurements (Főrész *et al.*, 2014). The absolute wavelength calibration of the FP lines is done by using Th-Ar reference frames.

A 1" diameter solid FP etalon from LightMachinery is used for the setup.

The FP is made of fused silica with 0.1 arcsec wedge, has a thickness of
1.686 mm and a reflective coating of 65% optimized over the 450-650 nm
wavelength range. The FP gives an FSR of 0.5 Å at 5000 Å, which is four
times the spectrograph resolution element 0.11 Å. A white LED source is
used as a light source, and a 200 μm core diameter optical fiber is used to
carry the light. The light from the fiber is collimated by a half-inch off-axis
parabolic mirror that directs the light to the etalon. Light at the output of the
FP is collected and coupled into output fiber by a similar off-axis parabolic
mirror. All reflective optics have been used to avoid chromatic aberration.
The components have been mounted on a cage based system. The fibers
are mounted on a flexure cut XY stage with translation capability to set
the focal distance from the mirror. The off-axis parabolic mirrors have the
option of being rotated in their holder using a micrometer screw for setting
their orientation. The etalon is mounted on a tip-tilt stage. The design of
the cage is shown in Fig. 2.7.
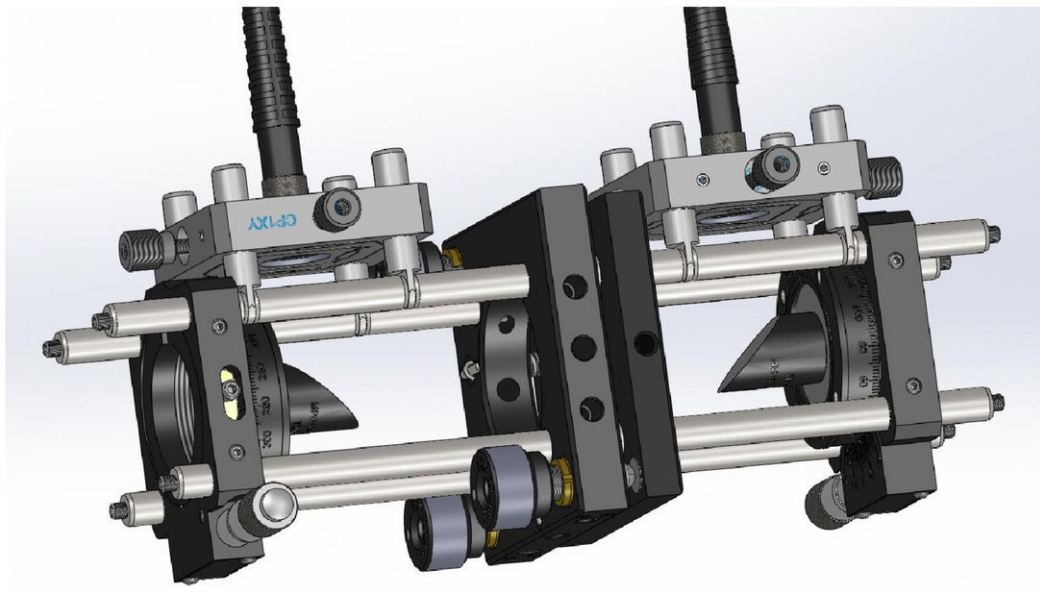
Figure 2.7: The opto-mechanical design of the cage based FP unit. Credits: Fűrész *et al.* (2014)

Since a solid etalon having a small thickness and volume is used, the
etalon is less prone to temperature and pressure variations. A drift of 1mK

is estimated at 5000 Å, which is equivalent to an RV drift of 2 m/s. Hence a temperature stabilization to mK level is implemented. The opto-mechanical setup is kept inside an 8" diameter and 10" tall vacuum cylinder that operates under a pressure of 10^{-2} mbar. The FP setup is suspended in the vacuum chamber using nylon wire to decrease the conductive path. A radiation shield between the chamber wall and FP system is used to avoid radiative coupling to the surrounding. A penetrating feedthrough has been designed and used to install the fibers in the chamber.

A 1 m × 1 m wooden crate is used to house the entire system with two layers of temperature control within it. The crate has Styrofoam insulation inside. Construction lumber has been used in the inner frame with embedded foam panels on the side. A liquid heat exchanger and a fan tray are placed above the inner frame. Air circulation within the box is provided by openings at the bottom of the frame. A liquid chiller connected with flexible pipes to the heat exchanger is used to maintain the temperature of the liquid at 17°C. The fan tray maintains the air temperature in the heat exchanger close to the liquid temperature. The entire crate sits in an air-conditioned room with temperature stability of 20°C ± 1°C. The inner frame contains another inner shell with 1 mm thick aluminium panels and heat tapes attached to them. RTD is used to measure the temperature within the shell and drive a PID loop for temperature control. The temperature inside the shell is maintained at 20°C with short bursts of heat. One RTD probe monitors the temperature of the etalon, and another sensor is used to measure the temperature in the outer shell, maintaining the final temperature in the entire setup within ±0.1°C. The schematic of the entire system is shown in Fig. 2.8.

2.7.3 HARPS & ESPRESSO Spectrographs

The High Accuracy Radial velocity Planet Searcher (HARPS) on the 3.6 m telescope at La Silla Observatory is a highly stabilized echelle spectrograph
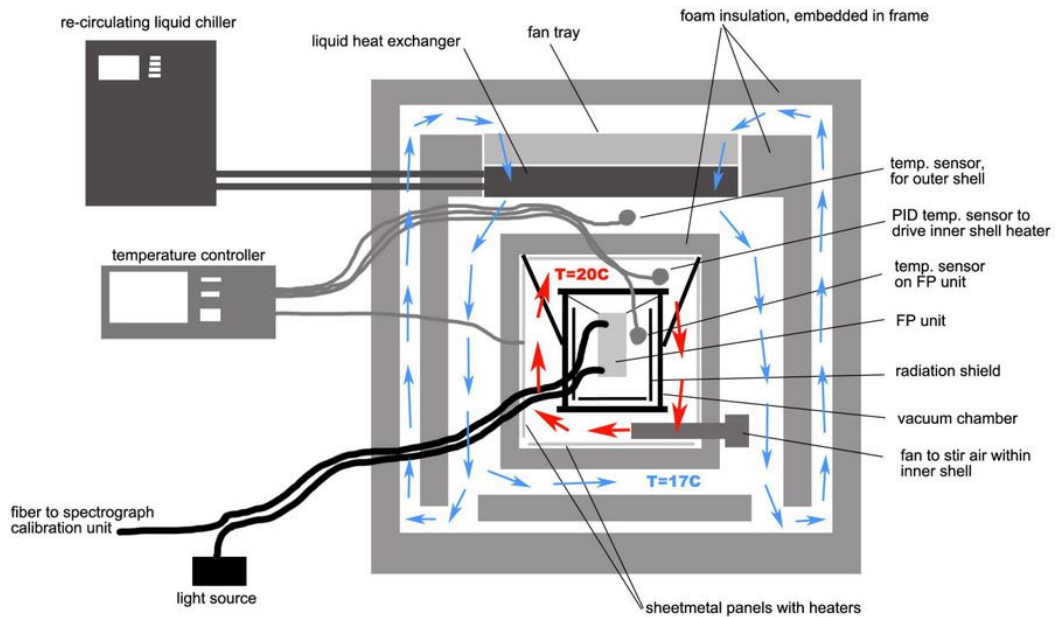
Figure 2.8: Schematic of the thermal control system being used for temperature stabilization of FP unit. Credits: Fűrész *et al.* (2014)

with a resolution of R=120,000 and covers a spectral range of 380-690 nm (Pepe *et al.*, 2000). The spectrograph is equipped with Th-Ar lamps for simultaneous calibration, Iodine cell, Fabry-Pérot etalon and LFC (Wildi *et al.*, 2009), for wavelength calibration. A two fiber system is used for simultaneous calibration: fiber A for stellar spectrum and fiber B for reference spectrum during science exposure. Both the fibers are illuminated with a calibration source to develop the wavelength calibration model. Comparing the calibration spectrum on fiber B between science exposure and calibration exposure gives the instrumental drift that can be corrected for in the science fiber.

For the FP based calibration setup, an air-spaced etalon is used with ring spacer consisting of a compound stack of thick Zerodur and thin BK7 that are optically contacted together (Wildi *et al.*, 2010). The FP used has a finesse of 6, an effective finesse of 4.3 and a cavity width of 7.3 mm. A laser-driven light source (LDLS) consisting of a Xe lamp that is excited by a pulsed pump laser is used as the primary light source for providing high brightness over the wavelength region (Wildi *et al.*, 2011). A 600 μm optical fiber is used for carrying the light from the source into the vacuum chamber. Initial

designs used collimating and focusing lens systems, which was replaced by reflective collimator in later design (for ESPRESSO). A 300 μm fiber carries light output from the FP to the spectrograph calibration unit. An expensive and complicated Zerodur support structure, with the elements optically contacted with each other, was used in the initial design. This was replaced by the opto-mechanical components being kept in an aluminium structure in subsequent designs like ESPRESSO. The vacuum tank is operated at a pressure of 10^{-3} mbar. Lakeshore temperature controller, along with silicon diode temperature sensors and a heater foil wrapped around the vacuum cylinder, provides temperature stability of 0.01K. The schematic of the entire instrument is shown in Fig. 2.9 The vacuum tank is placed in a thermally insulated box, and the entire setup is kept in a temperature-controlled spectrograph room. The image of the assembled vacuum enclosure is shown in Fig. 2.10.
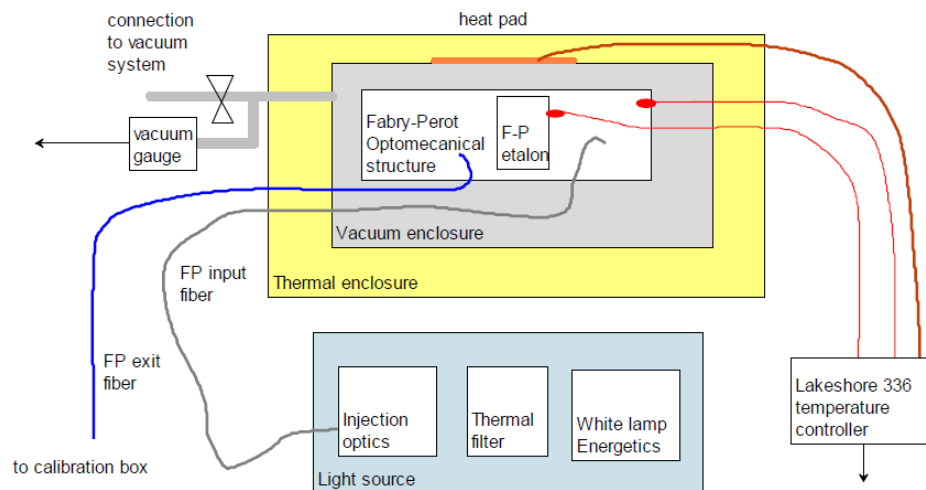
Figure 2.9: Schematic of complete FP based calibration system being used in HARPS. Credits: Wildi *et al.* (2012)

The spectrograph, along with the FP calibration system, gives radial velocity stability of 10 cm/s over one night and 1m/s stability over 60 days. A similar design of the setup has been used for ESPRESSO with appropriate FP to cover the wavelength range of the spectrograph (Cersullo *et al.*, 2019).

Figure 2.10: Opto-mechanical design of the FP calibrator for HARPS. The image on the left shows the CAD view. The right image is the assembled enclosure with FP and related optics inside, along with the optical fibers. Credits: Wildi *et al.* (2012)

2.7.4 SPIRou Spectrograph

Spectropolarimétre Infrarouge (SPIRou) is a stabilized spectrograph that operates in the NIR wavelength range, integrated on Canada-France-Hawaii Telescope (CFHT). The main objective of the spectrograph is to find and characterize exoplanets in the habitable zone of low and very low mass M stars. It also offers spectro-polarimetry to study the impact of magnetic fields in stars and planet formation. SPIRou has a resolving power R=75,000 and covers a wavelength range of 980-2350 nm (Donati *et al.*, 2018). Due to lack of calibration sources in the infrared region, FP based wavelength calibrator is used to cover the entire wavelength range of the spectrograph, to achieve stability of FP lines better than 30cm/s over a period of an observing night (12 hours).

An air-spaced etalon is used with Corning ULE spacers, a cavity length of 12.25 mm, a finesse of 13 (effective finesse=10.8) and a reflectivity coating of R=80% (Cersullo *et al.*, 2017). A laser-driven light source (LDLS) by Energetiq is used as a primary light source for ensuring high brightness. An octagonal optical fiber of 200 μm core diameter and 0.2 NA is used for carrying light to the FP and provide better scrambling. The fiber is mounted on a spider, and it illuminates a collimator which produces a 40 mm diameter collimated beam. The collimators used are on-axis parabolic mirrors of 50 mm clear aperture and 100 mm focal length having a silver coating. After passing through the etalon, the output is refocused by the parabolic mirror onto a circular fiber of core diameter 600 μm.

The opto-mechanical setup is fixed to the top flange of the vacuum enclosure on three points using a thermally insulating material. The enclosure is operated at a pressure of 10^{-4} mbar with a controlled rate of pressure rise at 7.4×10^{-3} mbar/day. Heating is done using resistor foils installed around the vacuum tank. Temperature is controlled using a Lakeshore controller and measured using precise silicon diode sensors. The operating temperature is kept at 25°C and stability of 0.05K is maintained throughout the enclosure. The schematic of the complete system is illustrated in Fig. 2.11. The entire setup is kept inside an isolated box in a temperature-stabilized spectrograph room. The absolute wavelength scale of the FP is determined using simultaneous Th-Ar exposures. The CAD view of the opto-mechanical components assembled inside the vacuum tank is shown in Fig. 2.12.

2.8   Conclusion

The details about the construction and working of FP etalons used as a calibrator in different astronomical spectrographs have been discussed. FP etalon provides an economical and less complex source of wavelength calibration. We have taken inspiration from the existing designs and have come up with
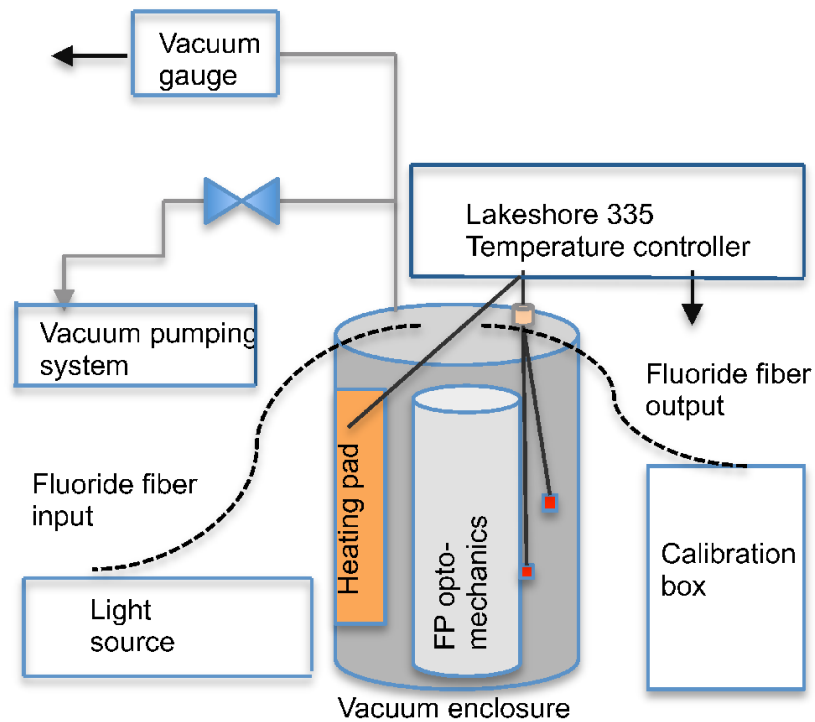
Figure 2.11: Schematic of the FP based calibration unit for SPIRou. Credits: Cersullo *et al.* (2017)

a very simple design using off the shelf available components. For example, instead of using a double-walled chamber with coolant liquid, we use printed heaters pasted on a single-walled enclosure. This simplifies the design and eliminates problems like jitter that can be caused due to the flow of liquid and is more cost-effective. The parameters of the FP we use and the stability is determined by the specifications and capabilities of the spectrograph it is designed for, i.e. HESP, and hence requires a unique design for the setup. These aspects have been discussed in detail in Chapter 3 and Chapter 4.
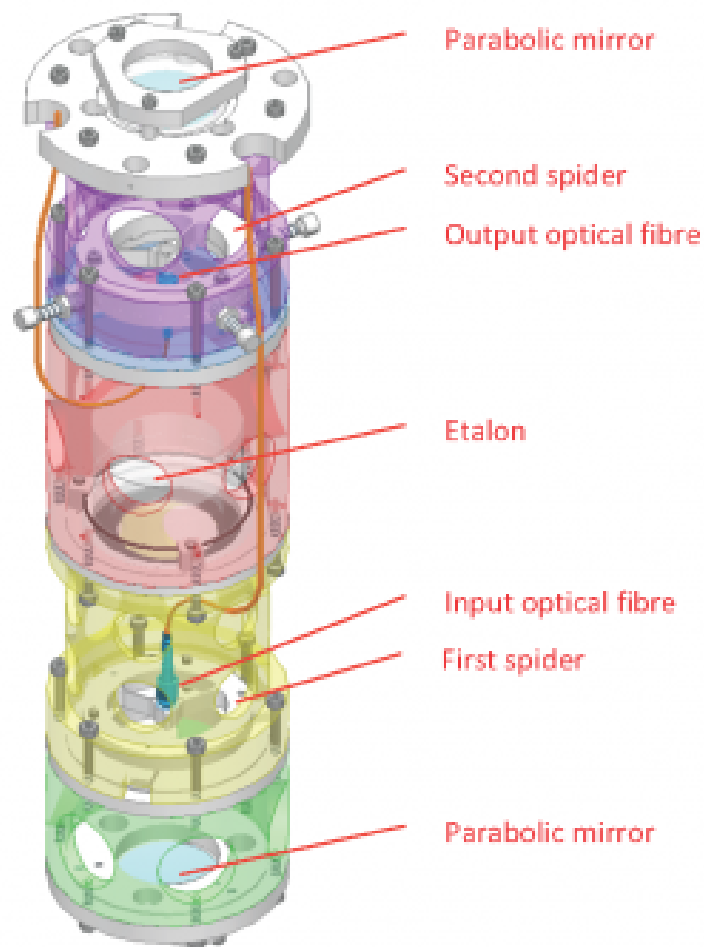
Figure 2.12: CAD view of the opto-mechanical design of the FP calibrator within vacuum tank. Credits: http://spirou.irap.omp.eu

Chapter 3

Factors affecting Fabry-Pérot Etalon stability [1]

3.1 Introduction

In order to use FP for high precision spectroscopy, the stability of the FP is a critical issue. According to Eq. 2.6 the separation between adjacent transmission peaks (FSR) depends upon refractive index n of the medium and cavity length d. Any change in the refractive index of the cavity or cavity length would change FSR, causing random drifts in calibration lines. Our objective is to minimize these fluctuations so that the FP cavity remains stable and FSR remains unchanged over time. These fluctuations can be introduced by temperature, pressure and humidity variations. Installing the FP unit in a temperature-controlled vacuum enclosure eliminates any such environmental variations. Getting stable transmission output from the FP depends upon the following factors:

1. Pressure stability of the FP housing environment

---

[1] *Part of this chapter is published in Tanya Das et al., Proc. SPIE. 10702, 2018 and in Tanya Das et al., Applied Optics Journal 59, 2020.*

2. Temperature stability of the FP housing environment

3. Illumination angle

   (a) Fiber size (core diameter)

   (b) Misalignment errors

4. Coating dispersion

3.2 Pressure stability of the FP housing environment

The refractive index of air is a function of temperature and pressure. The dispersion formula of dry air shows how the refractive index fluctuates with variation in pressure and temperature (Owens, 1967).

$$(n - 1) \times 10^8 = D_s \left[2371.34 + \frac{683939.7}{130 - \sigma^2} + \frac{4547.3}{38.9 - \sigma 2} \right], \qquad (3.1)$$

where, n is refractive index, σ is vacuum wave number, D_s is density factor for dry air given by,

$$D_s = \frac{P_s}{T} \left[1 + P_s \left(57.9 \times 10^{-8} - \frac{9.325 \times 10^{-4}}{T} + \frac{0.25844}{T^2} \right) \right], \qquad (3.2)$$

where, P_s is pressure of dry air, T is temperature of dry air.

The change in refractive index Δn can be converted into RV shift using the following equation,

$$\frac{\Delta n}{n} = \frac{V_{RV}}{c}, \qquad (3.3)$$

where, V_{RV} is the radial velocity error and c is speed of light.

The dispersion formula of dry air and Equation 3.3 are used to calculate

the RV shift at different pressure and temperature. This gives the pressure limit in which the FP has to be operated.
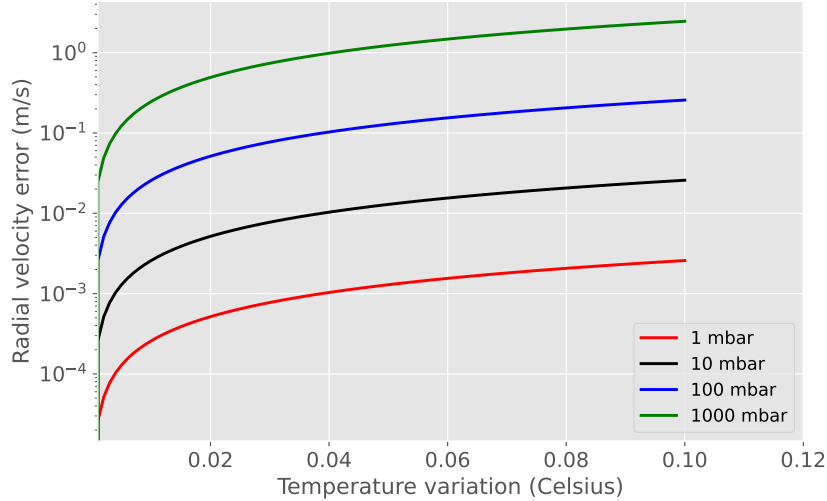
Figure 3.1: Radial velocity error caused by temperature variation at different pressure. The y-axis is in log scale.

It is observed from Fig. 3.1 that at a pressure of 1000 mbar, a temperature variation of 0.1 °C can induce an RV error of several tens of m/s, whereas, at 1 mbar pressure, the induced RV error for the same temperature variation reduces to a few cm/s. Hence, at atmospheric pressure, small temperature changes strongly affect the refractive index of air, causing significant errors in RV measurement. At low pressure, the effect of temperature variation on RV becomes less significant. Hence the FP setup is installed in an evacuated enclosure operating at a pressure below 1 mbar.

3.3 Temperature stability of the FP housing environment

FP cavity length varies with variations in the temperature. The parallel glass plates in FP are held together by a spacer made of a material having a very low thermal expansion. Cavity length d can change due to fluctuations in ambient temperature.

$$\Delta d = d_o \alpha \Delta T \,, \tag{3.4}$$

where, Δd is change in cavity length, d_o is initial cavity length, α is coefficient of thermal expansion, ΔT is change in temperature.

Small variations in temperature can alter the cavity length d, thereby causing large errors in measurement of radial velocity. Change in cavity length can be converted to RV units using the following equation,

$$\frac{\Delta d}{d_o} = \frac{V_{RV}}{c} \,, \tag{3.5}$$

where, V_{RV} is the radial velocity and c is speed of light.

Cavity spacer is usually made from Zerodur with a coefficient of thermal expansion around $2 \times 10^{-8} \ K^{-1}$ or from ULE glass with a coefficient of thermal expansion around $10^{-8} \ K^{-1}$. Equation 3.4 and Equation 3.5 are used to calculate the RV shift due to temperature variations, plotted in Fig. 3.2.
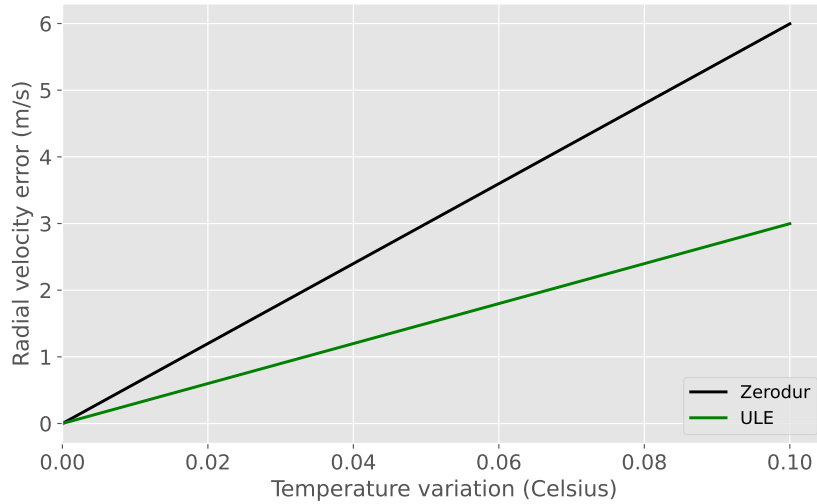
Figure 3.2: Radial Velocity error due to temperature variation in Zerodur and ULE glass.

Since limiting temperature fluctuations is the main objective rather than maintaining a specific temperature, the FP is being operated at a temperature $4\,°\text{C}$ - $5\,°\text{C}$ above ambient. To obtain an RV precision of 1-10 m/s, fluctuations in the temperature are limited to within $\pm 0.05\,°\text{C}$.

3.4   Illumination angle errors

Since the transmission function of the FP also depends upon the angle at which light is incident on the FP surface (Eq 2.1 and Eq 2.2), it is essential to ensure that FP is illuminated uniformly.
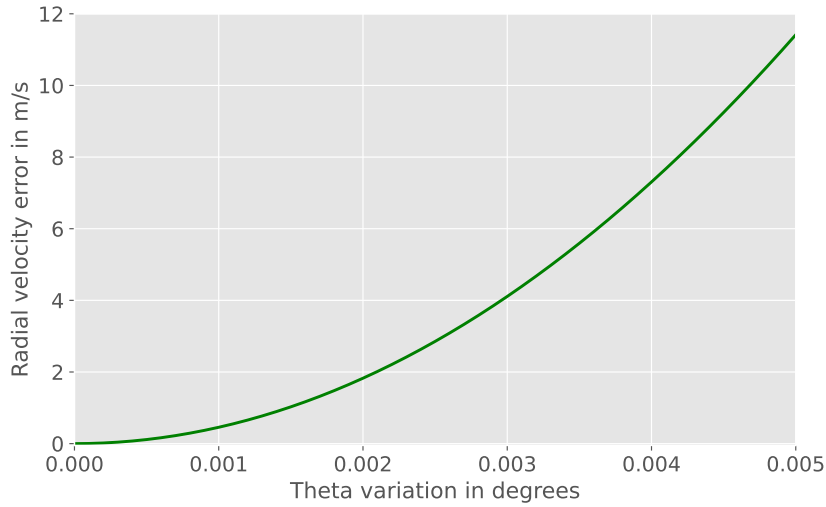
Figure 3.3: Radial velocity error due to variation in angle of incidence of light falling on the FP.

Fig. 3.3 shows the RV error that can be introduced due to light falling at a different incident angle on the FP surface. To keep this error below the required RV limits, the angular divergence should be kept less than 16 arcseconds. Divergence angle in illumination can be introduced by:

1. Finite diameter of the fiber core.

2. Misalignment between fiber and FP.

3.4.1   Finite diameter of fiber

The effective finesse of the etalon depends upon reflectivity finesse, the contribution from the surface finish, parallelism finesse and imperfect collimation due to the finite size of the light source (Cersullo *et al.*, 2017). The beam divergence resulting from the finite size of the fiber core, depicted in Fig. 3.4,

introduces loss in effective finesse and hence a shift in transmitted peaks towards the shorter wavelengths.
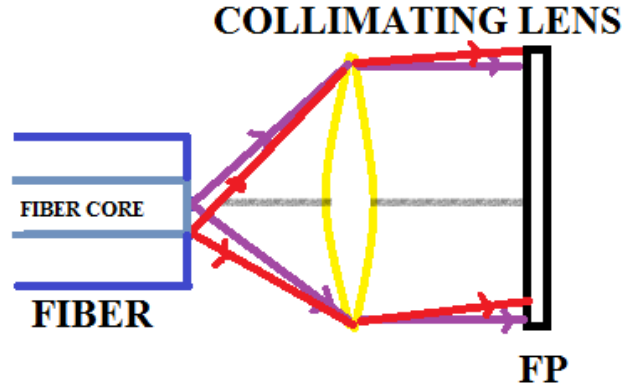
Figure 3.4: Cartoon depicting divergence in input light caused due to finite diameter of optical fiber illuminating the FP.

Using the method discussed in Cersullo *et al.* (2017), we have simulated the effect of different fiber sizes used for illuminating the FP and the RV error induced by it, as shown Fig. 3.5. It is seen that as the fiber diameter increases, the FP parameter and hence line quality degrades. This is because a fiber with a larger core acts as an extended source, leading to imperfect collimation.

3.4.2 Misalignment errors

Fig. 3.6 shows the angle in the illumination of FP caused when the fiber center is not correctly aligned with the FP. Misalignment or decentering of the fiber also causes line broadening and loss in effective finesse. Simulation of effect on FP lines due to different values of decentering was performed using the method suggested in Cersullo *et al.* (2017), and the RV error introduced by the same was calculated. In Fig. 3.7, the red curve shows the ideal FP output when there is no misalignment between the input optics and the FP. As the misalignment in the fiber increases, the quality of FP lines degrade, as shown by the purple and green curves.
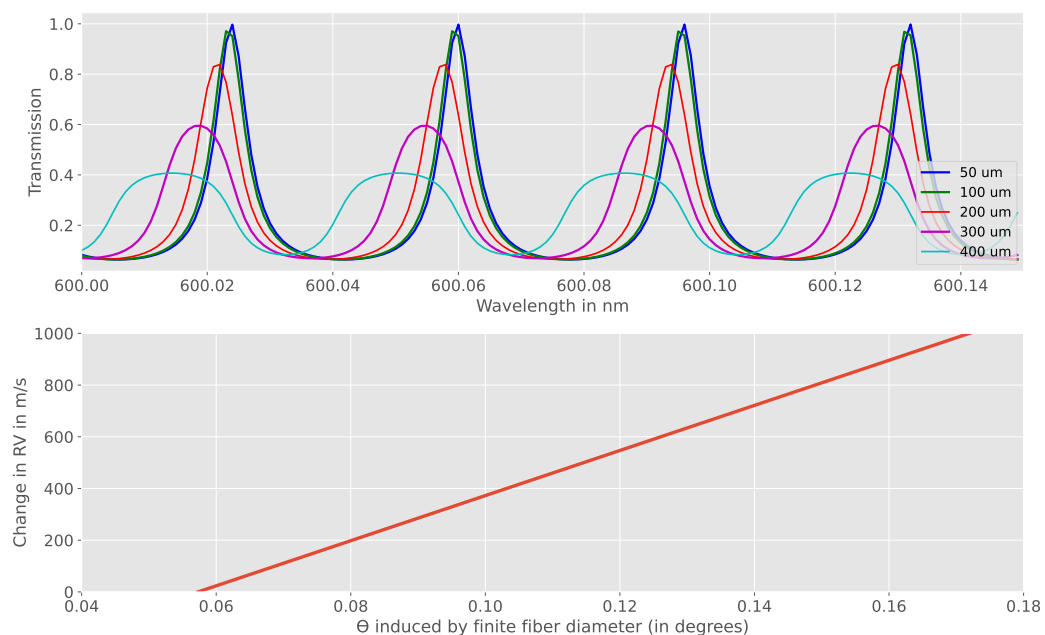
Figure 3.5: Top: Simulated transmission profile of FP for different fiber diameter. Bottom: Radial Velocity error induced in spectra due to finite divergence of fiber. This helps us in deciding the appropriate size of input fiber to be used to illuminate FP.
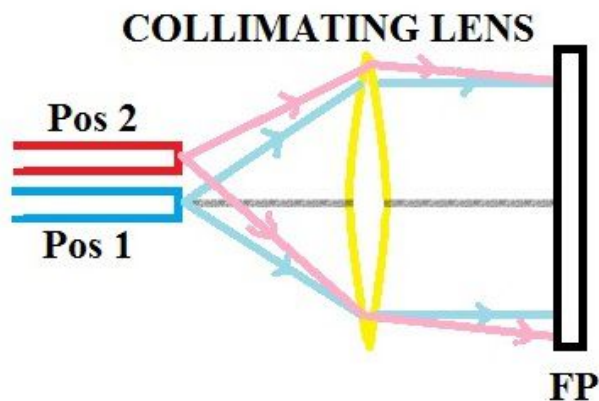
Figure 3.6: Cartoon depicting divergence in input light caused due to misalignment between the optical fiber and the FP. Pos 1 indicates no misalignment whereas Pos 2 indicates position of fiber not centered with respect to the FP.

3.5 Coating dispersion

For absolute wavelength calibration, the effective cavity spacing of etalon should be known with an accuracy better than $\Delta \lambda / \lambda \simeq 3 \times 10^{-8}$ for RV precision of 10 m/s. This implies that the cavity width should be known
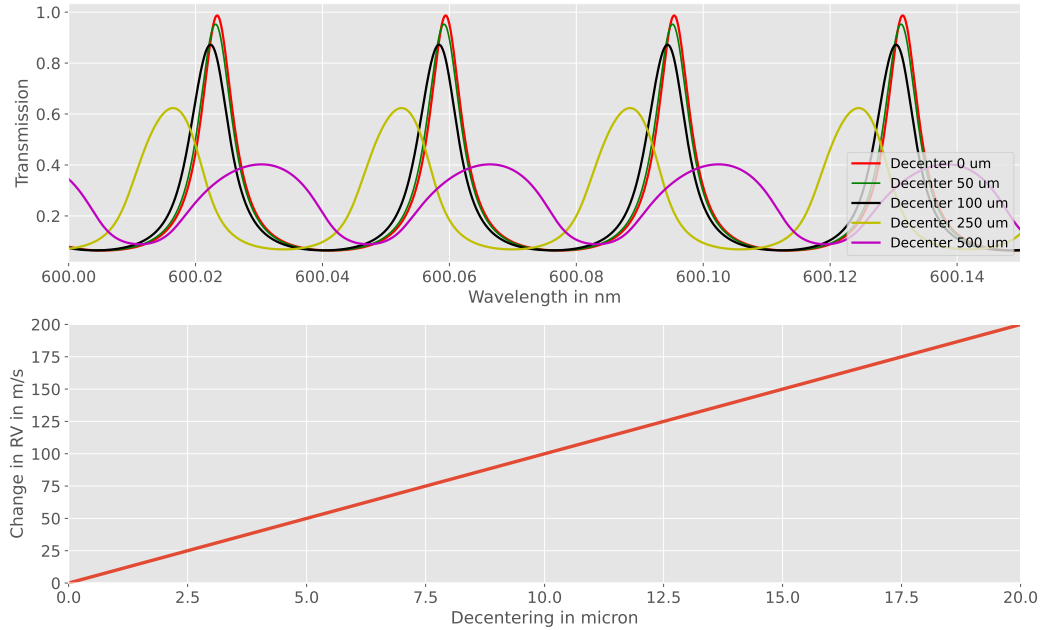
Figure 3.7: Top: Simulated transmission profile of FP for different fiber decentering value. Bottom: Radial Velocity error induced due to decentering of fiber. This helps us to decide on the limit of the misalignment that can be tolerated for the targeted RV precision.

with an accuracy of 1.5 Å. However, in practice, the cavity mirror separation cannot be measured with an accuracy better than ~ 1 μm (Bauer *et al.*, 2015). Determining the effective cavity width of the etalon and ensuring a constant FSR is further compromised by the finite thickness of the multilayer dielectric coating of the cavity mirrors. Photons of different wavelengths penetrate to different optical depths, leading to wavelength dependency of cavity spacing $d(\lambda)$. Therefore, the FP cavity lines, unlike LFC, will not be precisely periodic. This is one of the factors that could limit the use of FP for absolute wavelength calibration. The functional dependence of coating dispersion can be predicted and corrected, provided the coating structure is known (McCracken *et al.*, 2017). It is also possible to model the slow variations in FSR from the FP data taken with a high-resolution spectrograph. For example, Bauer *et al.* (2015) used a spline function to extract out the contribution of wavelength-dependent undulations of FSR. Another direct approach is to externally cross-calibrate the etalon with primary sources such as Fourier Transform Spectrograph or Th-Ar lamp (Wildi *et al.*, 2010). Once

a unique wavelength is assigned to each FP peak, a secondary wavelength solution can be easily derived without the need to consider coating dispersion. Another way to ensure a constant FSR across the wavelength range is to use dispersion-free cavity mirrors (Ma *et al.*, 2019; Chen *et al.*, 2010).

3.6   Summary

The stability of the output of Fabry-Pérot is crucial for it to be used as a wavelength calibration source, especially for high precision spectroscopy. To avoid any drift in the FP lines during observation runs (both short and long term), it is vital to ensure that the environmental requirements and opto-mechanical aspects are met to the best of their capability.

Based on the considerations and calculations made in this chapter, the design requirements for our instrument are listed in Table 3.1.

Table 3.1: Design requirements to achieve an RV precision about 10 m/s or better.

Design parameters	Required value
Pressure	≤ 1 mbar
Temperature stability	± 0.05 °C
Misalignment error	$< 5 \ \mu$m
Fiber size	$\leq 100 \ \mu$m

Chapter 4

Design of instrument [1]

4.1 Introduction

The instrument design comprises of two aspects, the opto-mechanical design and the design for environmental stability, namely, pressure and temperature control. Figure 4.1 gives an overview of the instrument at the component level.
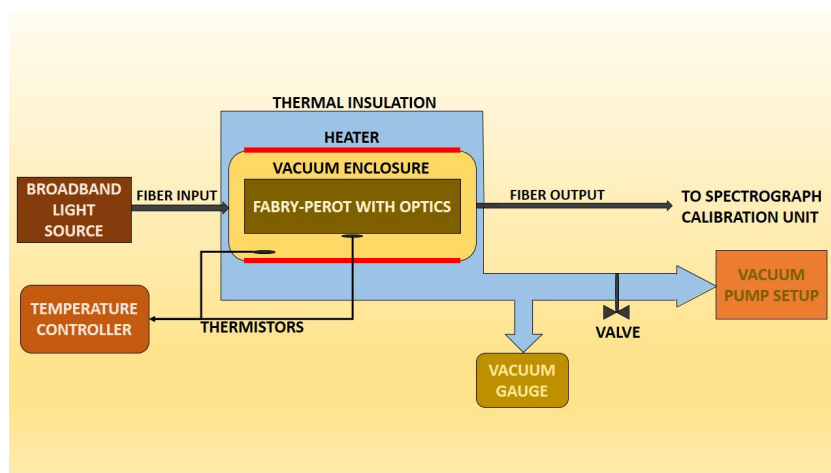
Figure 4.1: Illustration of the complete set up of Fabry-Pérot based wavelength calibration system.

---

[1]*Part of this chapter is published in Tanya Das et al., Proc. SPIE. 10702, 2018 and in Tanya Das et al., Applied Optics Journal 59, 2020.*

The complete instrument comprises of the following components:

1. The Fabry Perot unit along with collimating lens and precision mounts.

2. Light delivery system using multimode fibers, fiber feedthroughs and broadband light source.

3. Vacuum tank with pressure gauge, vacuum pump and electrical feedthroughs.

4. Temperature controller with heaters and insulation.

4.2   Pressure control

Simple off-the-shelf components have been used to construct the enclosure. A standard stainless steel cylindrical chamber of 333 mm length and 152 mm diameter (shown in Fig. 4.2) has been used to house the FP unit.
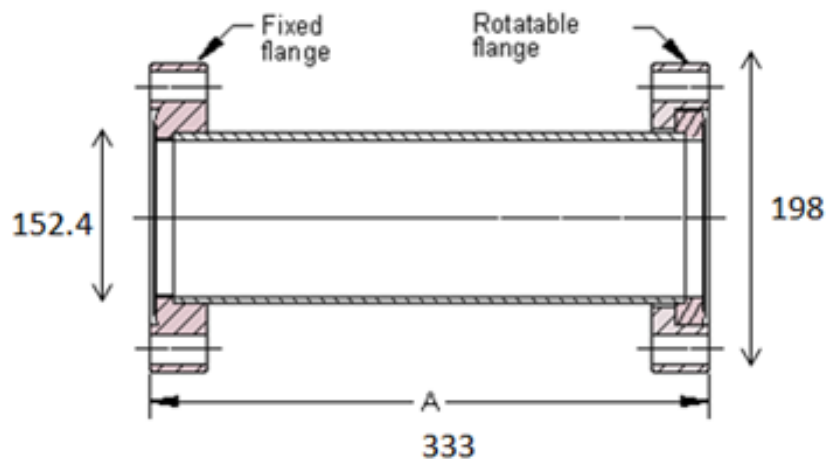
Figure 4.2: Schematic of vacuum enclosure being used to house FP and related optics. All the dimensions mentioned are in mm.

Fiber feedthroughs are used to provide access to the optical fibers into and out of the vacuum chamber. There are two types of feedthroughs available:

1. Penetrating feedthroughs have fibers directly running through them. It uses soft sealant material compressed by an end cap, through which the

fibers pass. The cap holds the sealant material that surrounds the fibre and seals the hole.

2. Receptacle type uses two separate fibers on either side of the vacuum flange. It consists of a short fiber stub that is sealed using vacuum glue. The second fiber is placed close to the input stub. The issue with this design is that the fibre ends are highly polished, and the airgap between two fibres might result in etalon effect and casue light loss.

To avoid the light loss which occurs in the receptacle type feedthroughs, we have designed and fabricated an in-house penetrating type feedthrough for inserting the fiber into the chamber (Kirilov *et al.*, 2014). An initial prototype was made using a silicone plug, as shown in Fig. 4.3.
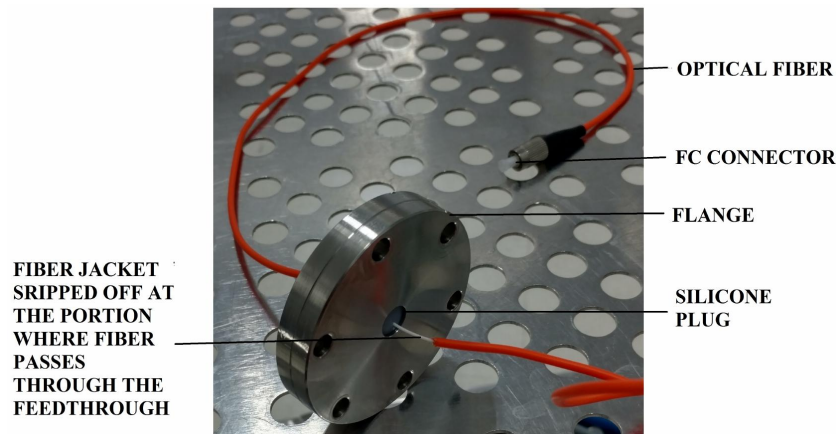
Figure 4.3: A penetrating type fiber feedthrough developed using silicone plug. The fiber is inserted into a cut made in silicone plug and then pressed using pressing plate from one side.

To provide better sealing, the silicone plug was replaced by plugs made of Viton material. The CAD design for the feedthrough is shown in Fig. 4.4. A longitudinal slit along the plug is made, and the fiber is inserted radially into the plug. The length of the plug is kept 1 mm more than the thickness of the flange, and a pressing plate with a slit to accommodate the fiber is screwed on the outer side of the flange to push the plug into the flange and provide better sealing. During the operation of the pump, the plug gets pulled

inwards under the influence of vacuum and seals off the opening, after which the pressing plate on the outer side is tightened further.

1. Flange model
2. Viton plug
3. Pressing plate
4. M3 screws
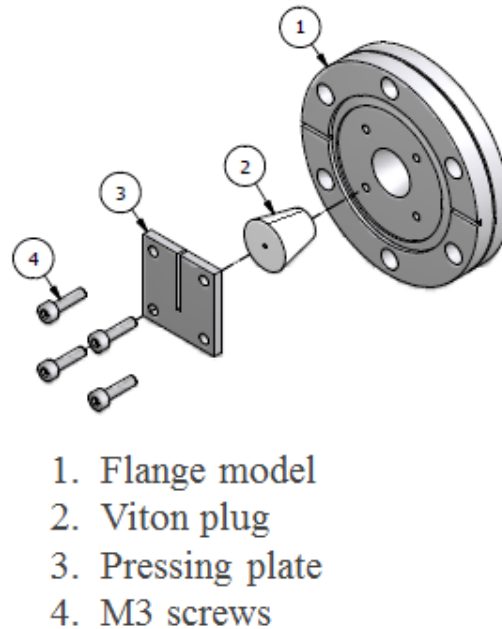
Figure 4.4: Design of the penetrating type feedthrough fabricated in house.

A combination of roughing pump and turbo pump is being used to reach the desired vacuum level. Pfeiffer HiPace 80 Turbo pump is being used because it gives the required pressure range with minimum vibration effects. To avoid introducing any vibration into the setup, the pumps are kept away from the main FP setup, and a bellow is used to connect the turbo pump with the chamber to dampen any vibration. Pfeiffer vacuum Pirani gauge PKR 251 has been used for the measurement of the pressure inside the chamber. The pressure stability of the setup has been tested, and a vacuum pressure of 0.03 mbar was achieved in laboratory tests. The data for pressure has been logged for 8 hours in the laboratory test and is plotted in Fig. 4.5.

4.3 Temperature Control

In order to obtain stable reference lines using FP, minimum fluctuation in the temperature inside the vacuum enclosure has to be ensured. To bypass the
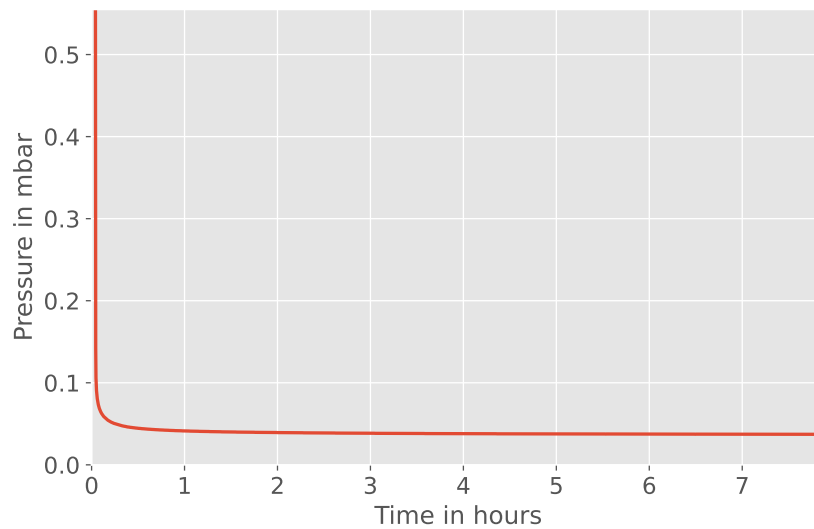
Figure 4.5: Pressure stability of the FP enclosure achieved during a laboratory test run.

need for cooling and to keep the hardware simple, we decided to operate the instrument at about 5 °C above the ambient temperature, which is set manually. A digital Proportional-integral (PI) controller was designed in-house using Arduino Uno micro-controller and off-the-shelf electronic components for temperature control, as shown in Fig. 4.6.

Figure 4.6: Temperature controller circuit with Arduino Uno Microcontroller.

The enclosure is initially heated in a controlled manner so that the temperature reaches a set point, after which the feedback loop in the controller

maintains the temperature with minimum fluctuations. The block diagram of the control process is shown in Fig. 4.7.
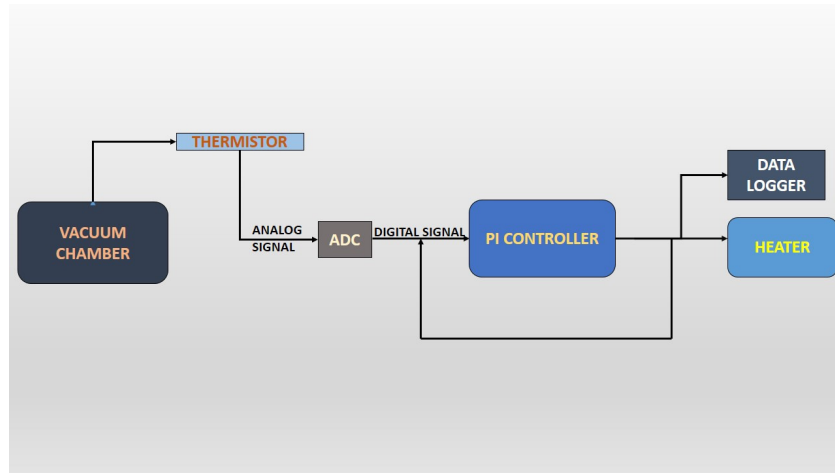
Figure 4.7: Temperature controller block diagram. The temperature of the chamber is sensed using thermistors and relayed to the Arduino board through an external 16 bit ADC for further processing.

The nominal operating temperature for the enclosure is 5 °C above the room temperature with fluctuations limited within ±0.05 °C. Thermistors are being used as temperature sensors. Four thermistors have been installed, two inside through electrical feedthrough and two outside the chamber. Response from the thermistor mounted on the inside wall of the chamber is used for temperature control. Printed polymer PTC heating elements, connected in series, are used to heat the chamber. Thermal insulation is provided by nitrile rubber, and the entire setup is kept inside a Styrofoam box, acting as an outer layer of insulation. Fig. 4.8 shows the complete laboratory setup of the vacuum enclosure.

The temperature stability of the setup was also tested in the lab. The test was conducted over 8.5 hours. The enclosure temperature could be maintained with the required stability as shown in Fig. 4.9. The maximum and minimum deviations in the temperature were within ±0.05 °C during the test run.
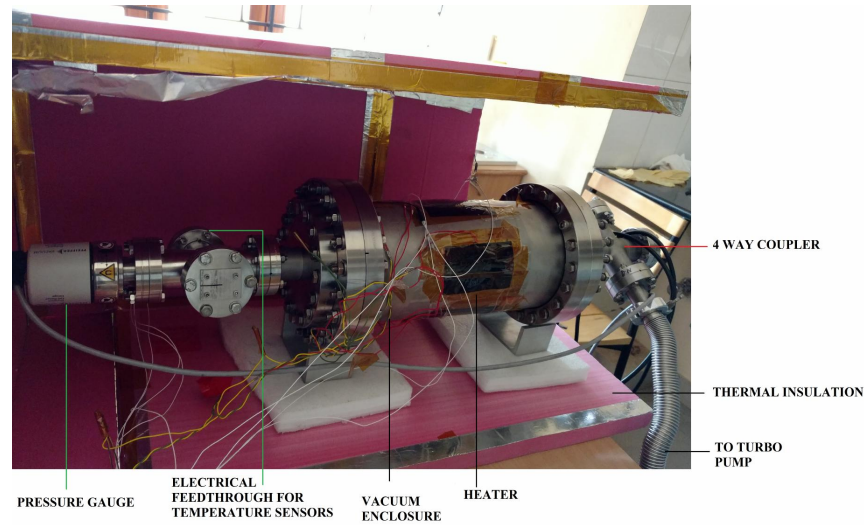
Figure 4.8: Complete instrument assembly with heaters and sensors in the laboratory. Nitrile rubber insulation is not shown in this image.
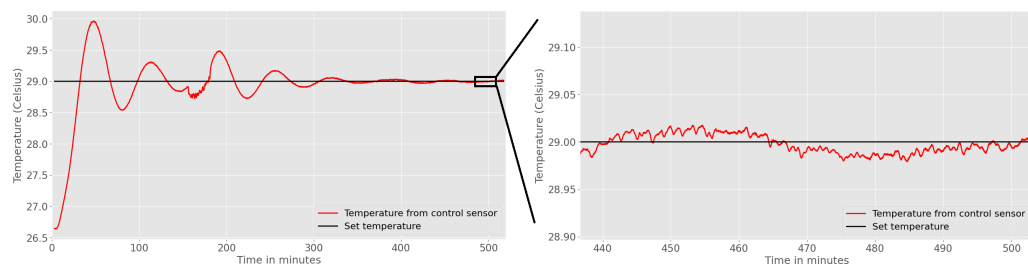
Figure 4.9: Left: Temperature controller performance shown in the plot. Temperature from control sensor is given as input to the controller. Right: Zoomed in view showing the temperature deviations from set point are maintained within ± 0.05 °C.

4.4 Opto-mechanical Design

The details of the optical components used are given in the following subsections.

4.4.1 Light source

We are using an intensity stabilized broadband fiber-coupled LED from Thorlabs (model MBB1F1) as the light source, shown in Fig. 4.10. The wavelength range of operation provided is 470 nm - 850 nm. The output connector is fixed and compatible with SMA fibers. The light source was

Figure 4.10: LED coupled broadband light source MBB1F1. Credits: Thorlabs

chosen due to its property of giving a flat spectral emission over a wide range of wavelength, seen in Fig. 4.11.
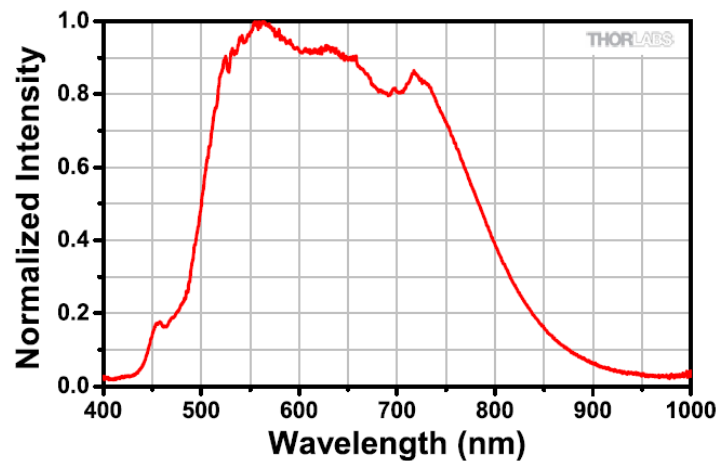
Figure 4.11: Performance of the bare LED used in MBB1F1. Credits: Thorlabs

4.4.2   Optical fibers

Optical fibers with a core diameter of 105 μm are used to carry light into and out of the chamber, respectively. The fibers being used are low OH, silica core step-index multimode fiber from Thorlabs (Model: M15L05). The fiber has a core diameter of 105 μm, NA=0.22 and operates in the wavelength range 400 nm - 2400 nm. The fiber attenuation plot is shown in Fig. 4.12.
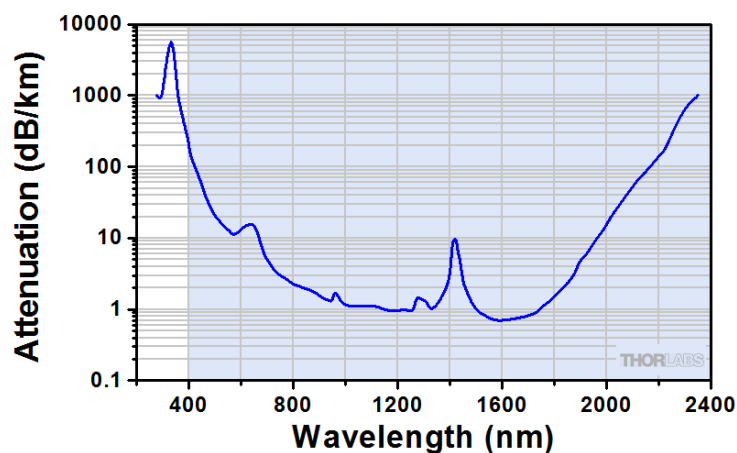
Figure 4.12: Attenuation values with respect to wavelength for M15L05 optical fibers. Credits: Thorlabs

4.4.3 Achromatic lens

Achromatic doublets are designed to keep the effect of chromatic aberration under control. Generally, it comprises two lenses made from glasses with different dispersion values. The concave (negative) element and the convex (positive) element are cemented together so that the chromatic aberration of one element counterbalances the other.

Since the system is compact, achromat doublets (AC254-050-A-ML) of focal length 50 mm are used to collimate and collect light from the FP. The lenses are of 1" diameter and have AR coating for the wavelength range 400 nm - 700 nm, the reflectance plot of which is shown in Fig. 4.13.

4.4.4 Fabry-Pérot Etalon

The FP etalon being used in the instrument setup is shown in Fig. 4.14. It was custom built by SLS Optics Ltd., to our specifications. The cavity spacing and FSR were decided based on the resolution of the spectrograph the calibration setup is designed for. For optimal sampling of the FP lines on spectrograph CCD, the FSR of FP should be 2-3 times more than the spectrograph resolving power. The resolution of Hanle
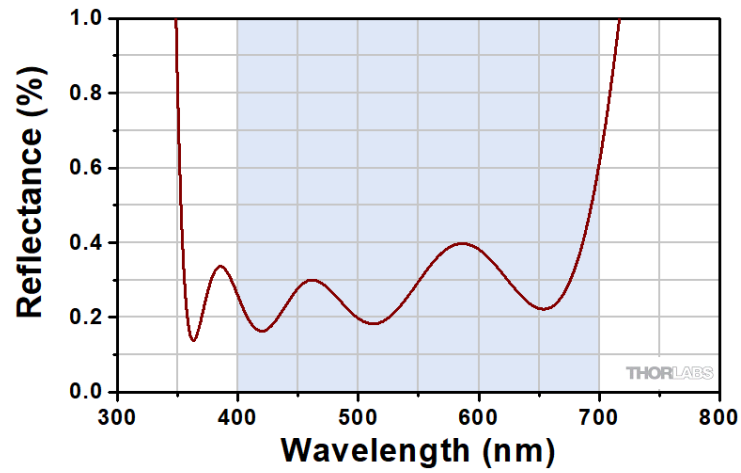
Figure 4.13: Achromatic doublet visible anti-reflection(AR) coating. Credits: Thorlabs
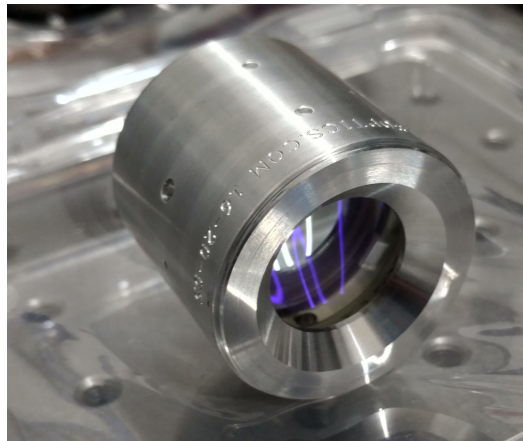
Figure 4.14: The Fabry-Pérot etalon being used in wavelength calibration setup.

Echelle Spectrograph is R=60,000. Resolution of a spectrograph is given by Equation 1.3. Converting the equation in terms of frequency (ν) using Equation 4.1

$$\lambda = \frac{c}{\nu} , \tag{4.1}$$

We get,

$$R = \frac{\nu}{\Delta\nu} , \tag{4.2}$$

Using Equation 4.1 and Equation 4.2, for $\lambda = 600\ nm$, we get spacing

between two lines to be $\Delta\nu = 8.3\ GHz$ for the spectrograph. Hence, the FSR for FP was decided to be 30 GHz. For the given FSR, using Equation 2.6, the cavity length was calculated to be 5 mm.

The cavity mirrors were prealigned in the factory and securely sealed inside an aluminium holder. Both mirrors have broadband (500-750 nm) multi-layer coating. Fused silica was used as a substrate, and a low thermal expansion Zerodur ring was used as a spacer between two flat mirrors, forming a plane-parallel cavity which is a preferred configuration for a white-light optical filter.

Although the high reflectivity coating(>90%) can produce narrow lines, an average reflectivity of 60% was selected to ensure a uniform response of the FP over the desired wavelength range of the spectrograph (400-750 nm). Reflectance spectra of the cavity mirrors are shown in Fig.4.15. Other specifications of the FP used in our setup are summarised in Table 4.1.
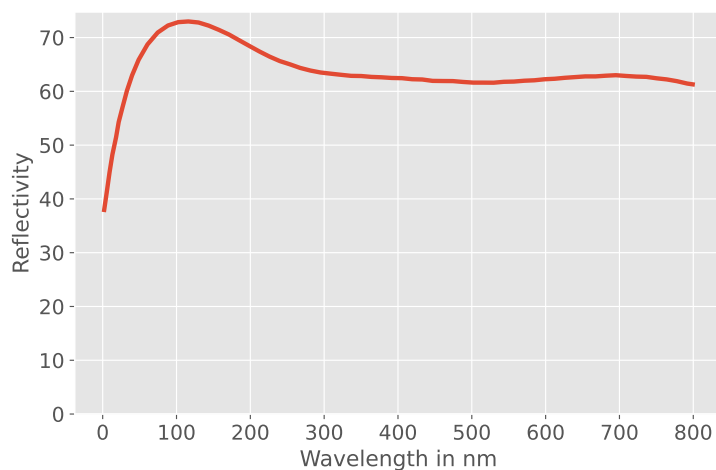
Figure 4.15: Reflectance spectra of the Fabry-Pérot cavity mirrors measured with monochromator. The spectra was provided by the manufacturer.

Light from the broadband light source is carried by the input multimode fiber and is collimated using the achromat doublet, which illuminates the FP. Light output from the FP is collected by another achromat doublet which fo-

Table 4.1: Specifications of the Fabry-Pérot etalon

Etalon type	Air spaced
Mirror material	Fused Silica
Spectral coverage	$500 - 750$ nm
Cavity thickness	5 mm$\pm$0.001 mm
Finesse	$\sim$6
Clear aperture	20 mm
Free Spectral Range	30 GHz
Coating reflectivity	$\sim$60%

cuses light into the output multimode fiber that carries light into the spectrograph. The end-to-end ray diagram of the optical setup is shown in Fig. 4.16.
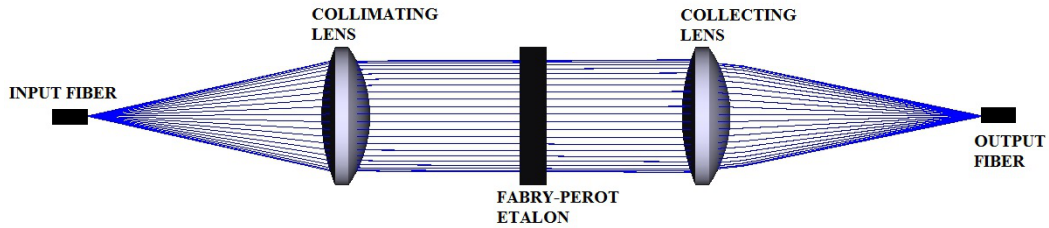
Figure 4.16: Ray diagram of the complete optical setup showing the beam path from input fiber to output fiber, through the lenses and the Fabry-Pérot.

A stable mounting scheme for holding the FP unit with its light collimation and collection optics is required. For this purpose, we have designed and tested two different mounting schemes: a cage based mounting as shown in Fig. 4.17 and a rail-based mounting as shown in Fig. 4.18. Cage based mounting scheme has been used for characterizing the FP with a Fourier Transform Spectrograph (FTS). Rail-based mounting scheme is being used to hold the optical components inside the vacuum chamber because of its stability, rigidity, and the design's adherence to the size constraints.

Instead of using only one side of the tube for fiber feedthrough, in which case the output fiber has to be bent and brought back to the same feedthrough, fiber feedthroughs are installed on both sides of the tube so that the fiber can go through and through, also avoiding the bending of fiber. For this purpose, T couplers are being used on both sides, which also provides an additional length to accommodate the fiber ferrules, hence taking care of the length con-
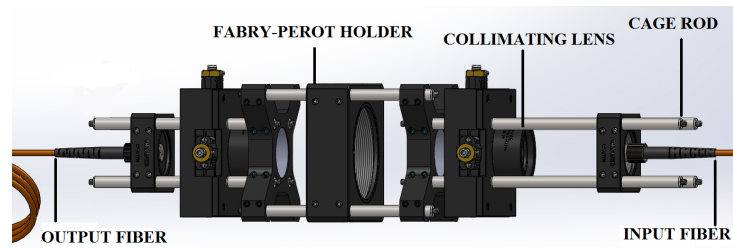
Figure 4.17: CAD drawing of the cage based mounting scheme for holding FP and related optics.
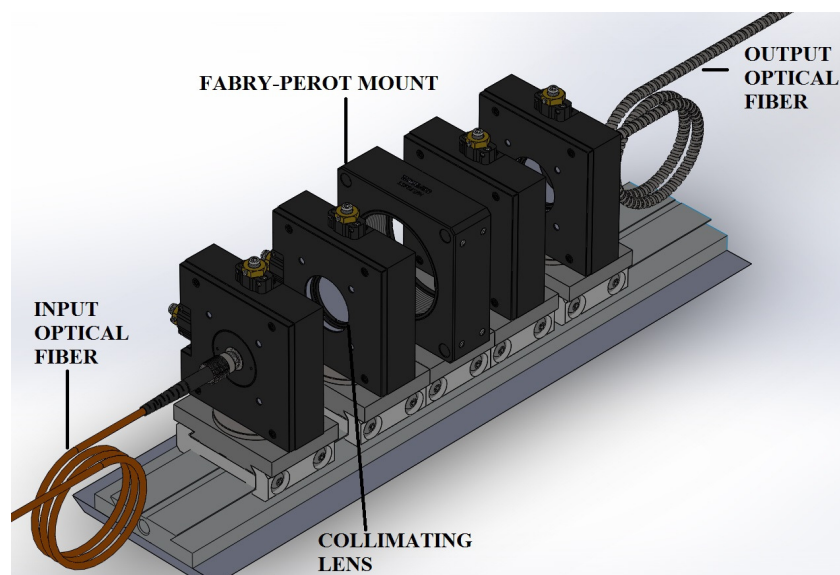
Figure 4.18: CAD drawing of the rail based mounting scheme for holding FP and related optics.

straint. The total height of the optical setup, including the rail, has been kept within 115 mm, and the total length of the setup is 290 mm. This allows us to have a stainless steel support platform that is 5 mm thick and welded at a height of 10 mm from the base of the chamber. CAD drawing of this concept is shown Fig. 4.19. The rail is mounted and secured on the support plate with the help of four M6 countersunk screws. Fig. 4.20 shows the optical setup mounted inside the chamber.

OUTPUT OPTICAL FIBER

FIBER ADAPTER

FABRY-PEROT HOLDER

COLLIMATING LENS MOUNT

VACUUM ENCLOSURE

INPUT OPTICAL FIBER
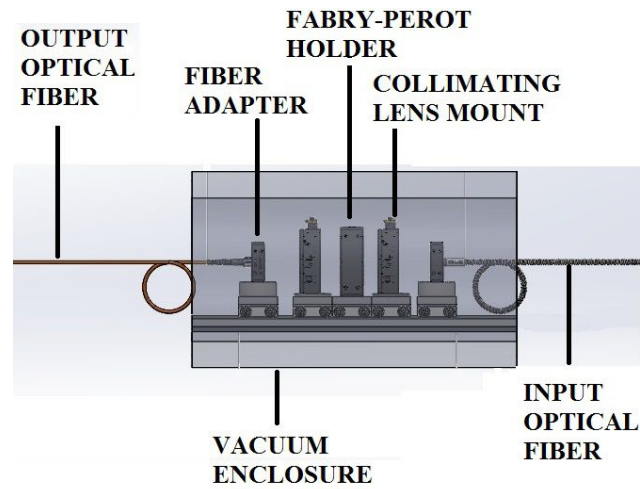
Figure 4.19: CAD design of vacuum chamber with support platform and opto-mechanical setup.

VACUUM ENCLOSURE

THERMISTOR FOR SENSING TEMPERATURE

OPTOMECHANICAL ASSEMBLY

DOVETAIL RAIL
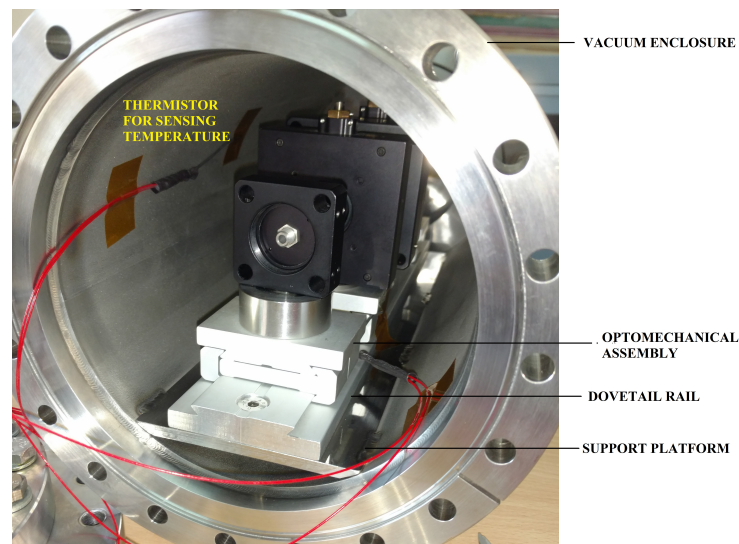
SUPPORT PLATFORM

Figure 4.20: Fabry-Perot assembly mounted on support platform inside the chamber in laboratory.

4.5 Summary

Based on the required design parameters discussed in Chapter 3, we have built a Fabry-Pérot based wavelength calibration system. It is a low-cost system, designed and developed using off-the-shelf components with the temperature controller and the vacuum enclosure developed in-house.

The optical components and the FP were decided based on the installed

specifications of the spectrograph. Two different schemes for the opto-mechanical design of FP setup were developed and used in different testing environments. We have also designed and machined penetrating type optical feedthroughs for lossless transmission of light in and out of the vacuum enclosure. The entire setup has been tested for temperature and pressure stability in the laboratory, and the expected values for both could be reached.

Chapter 5

Performance test of
Fabry-Pérot [1]

5.1   Introduction

The performance of etalon has been tested with three different spectrographs:

1. Fourier Transform Spectrograph (FTS) facility at Bhabha Atomic Research Center (BARC), Mumbai.

2. High Resolution Echelle Spectrograph on Vainu Bappu Telescope (VBT), Kavalur.

3. Final installation and testing with Hanle Echelle Spectrograph (HESP), Hanle.

   The first two tests were conducted at normal temperature and pressure without any environmental control. In this chapter, we will present descriptions of the three spectrographs used for the purpose of testing the FP along with discussions on the results obtained with them.

---

[1] *Part of this chapter is published in Tanya Das et al., Proc. SPIE. 10702, 2018; in Tanya Das et al., Proc. SPIE. 11447, 2020 and in Tanya Das et al., Applied Optics Journal 59, 2020.*

5.2 FP performance test with FTS

5.2.1 Fourier Transform Spectrograph

Fourier Transform Spectroscopy (A'Hearn *et al.*, 1974; Becker & Farrar , 1972) is a technique that produces the spectrum of a source through modulation of it's radiation in time domain and Fourier transforming it. Fourier transform spectrograph uses modified Michelson Interferometer setup with one of the mirrors kept movable, inducing optical path difference. The intensity at the output is measured at different positions of the movable mirror, which converts the time delay into spatial coordinates. The interference between light reflected off the stationary and movable mirrors hence produce a wavelength dependent interferogram. The input spectrum can be constructed by performing Fourier Transform on the same. Fig. 5.1 shows a schematic depicting the working principle of FTS.
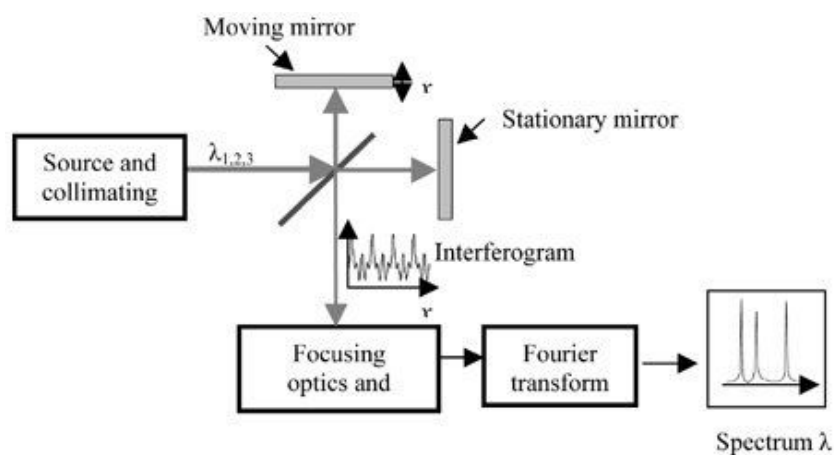
Figure 5.1: Schematic of a Fourier Transform Spectrograph based on Michelson interferometer setup. Credits: Saptari (2003)

The high resolution FTS facility at Bhabha Atomic Research Center (BARC), Mumbai, houses Bruker IFS 125HR model of FTS, shown in Fig. 5.2. The FTS can provide a high wavelength resolution of 100,000 over a wide wavelength range, starting from 5 cm^{-1} in far-IR to 50,000cm^{-1} in UV. It can also provide a path length upto 4 m for the movable mirror. The spectrograph

uses He-Ne laser as internal reference, which can be removed from light path if not necessary.

Figure 5.2: Bruker IFS 125HR Fourier Transform Spectrograph. Credits: Bruker Optics

This FTS has been used to characterise the parameters of FP, namely, cavity length, FSR, interference order and full width at half maximum (FWHM) of the FP lines. The internal reference (a frequency stabilized He-Ne laser) of the FTS can provide an accurate wavelength estimation of the FP peaks. The wavelength position of the FP lines is not known beforehand since it is solely determined by the cavity length d and the interference order m which is unknown. To determine the position of FP lines and other characteristics of FP, a complete scan of the FP over the visible wavelength range (500-750 nm) is taken using FTS. This aids in generation of a map of wavelength versus FP peak number which can be used to produce a high fidelity wavelength solution model for the spectrograph.

5.2.2   Results

For the purpose of the test, the etalon was mounted on a cage assembly, as shown in Fig. 5.3. The collimated output from the FP directly illuminates the FTS input port, to obtain transmission spectra at a resolution of 100,000.
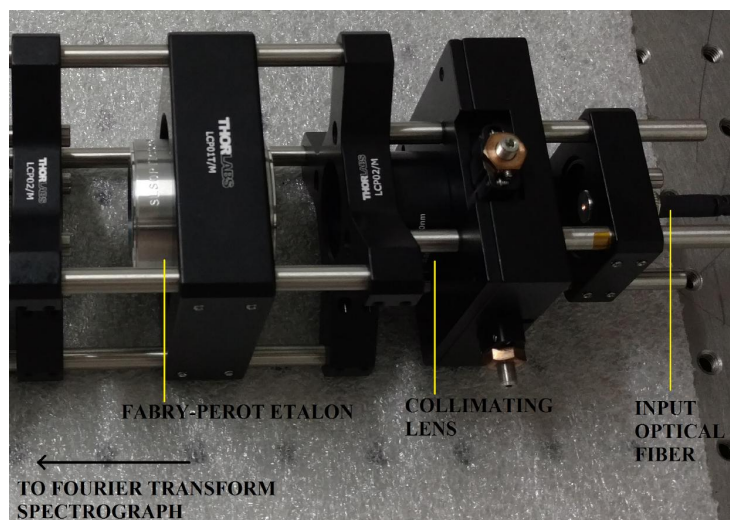
Figure 5.3: Image of FP mounted in a cage assembly for testing with FTS.

FTS spectra of the FP has been analysed and the FP parameters provided by manufacturer were compared with the results obtained from the test. Fig. 5.4 shows the spectra of FP as obtained from FTS.
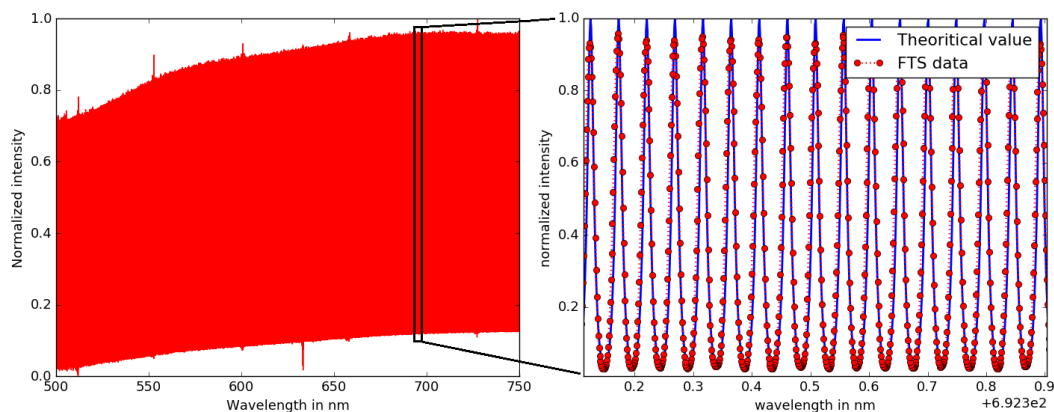
Figure 5.4: Left: FP transmission spectra with broadband LED light source. Right: A narrow slice of the spectra clearly showing the equispaced FP transmission peaks. The theoretical transmission as obtained by datasheet calculations (blue curve) have been overplotted.

During the analysis, we found that Gaussian fit to the individual FP lines provides a better approximation to line center and line width. We determine, from the data, the FSR for each wavelength and the FSR variation is plotted in Fig. 5.5. A 2nd order polynomial is fit through the varying FSR, the residue between the actual values and the fit is determined, RMS value of which is

9.42×10^{-8}. A small gap in the spectra around 633 nm is due to the presence of a strong He-Ne laser line that is used as a frequency reference for scanning the FTS.
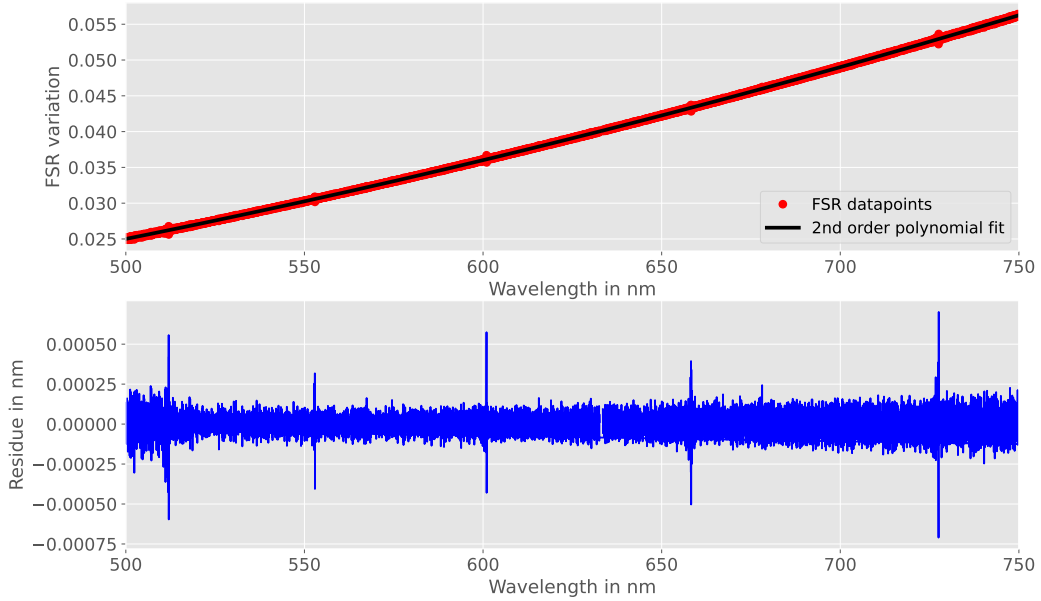
Figure 5.5: Top panel: FSR variation as a function of wavelength. A second order polynomial is fit through the obtained FSR. Bottom panel: Residual between polynomial fit and actual data. The periodic spikes in the residuals are RF pickup by the FTS from the drive electronics of the LED light source.

To investigate the impact of coating dispersion (see section 3.5) in our FP, we looked for systematic variations in FSR. Other than random scatter, the measured FSR did not show any noticeable trend that can be attributed to coating dispersion. It is, therefore, likely that coating used in our FP had nearly a flat response.

The FWHM of all the FP lines have also been calculated. The variation of FWHM across the wavelength range is shown in Fig. 5.6. It was seen that the FSR of the FP lines remain unchanged when compared to the FSR from the theoretical calculations. An increase in FWHM of the lines was observed as compared to expected theoretical values. The values of FSR and FWHM obtained from FTS data and calculated theoretically, have been plotted simultaneously in Fig. 5.7 to show the comparison.

The average cavity width of etalon was calculated to be 4.999 mm (cavity
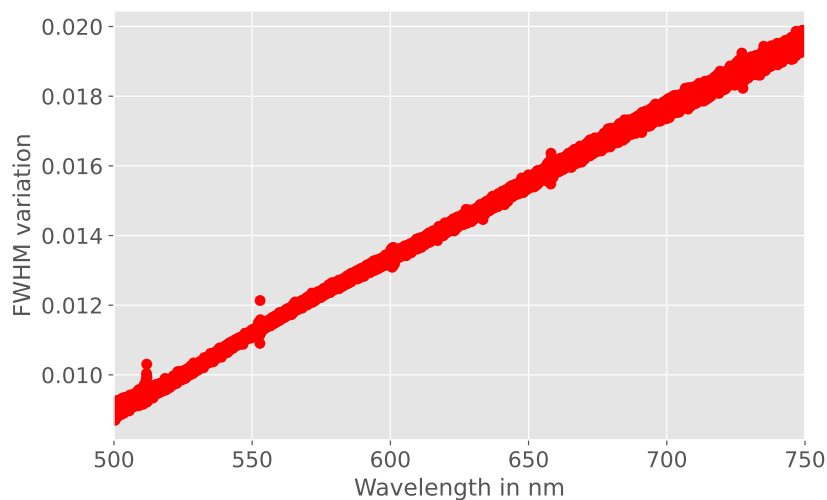
Figure 5.6: FWHM variation calculated from FTS data as a function of wavelength.
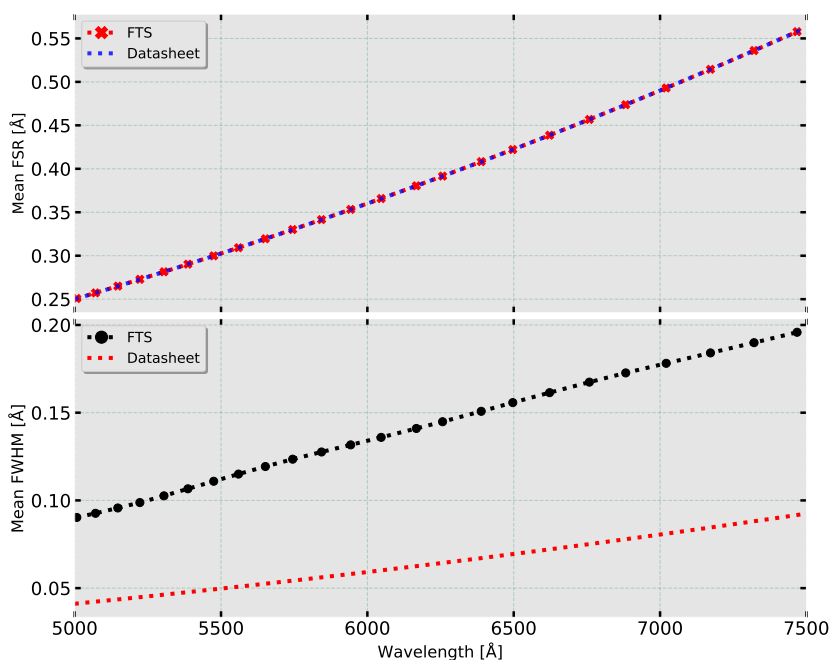
Figure 5.7: Top panel: The FSR determined from FP transmission spectra taken with high-resolution FTS and the expected values computed from the etalon parameters specified in the FP datasheet. Bottom panel: FWHM computed from FTS data and the expected value determined based on datasheet parameters.

length provided by manufacturer is 5 mm $\pm$ 0.001 mm). The cavity width of etalon is not constant throughout and varies as a function of wavelength. This is due to the soft coating on the FP, which causes different penetration depth for photons of different energy (Bauer *et al.*, 2015). Hence, cavity

widths vary for photons of different wavelength. Therefore, along with mean effective cavity width, cavity width as a function of wavelength $d(\lambda)$ also has to be determined. From the FSR values obtained by fitting the polynomial and Equation 2.7, we calculate the cavity width at each wavelength and the average cavity width of the etalon. Plot of cavity width as a function of wavelength is shown in Fig. 5.8. Apart from a random spread around 4.999 mm, we don't see any functional dependence of the coating dispersion on cavity length variations.
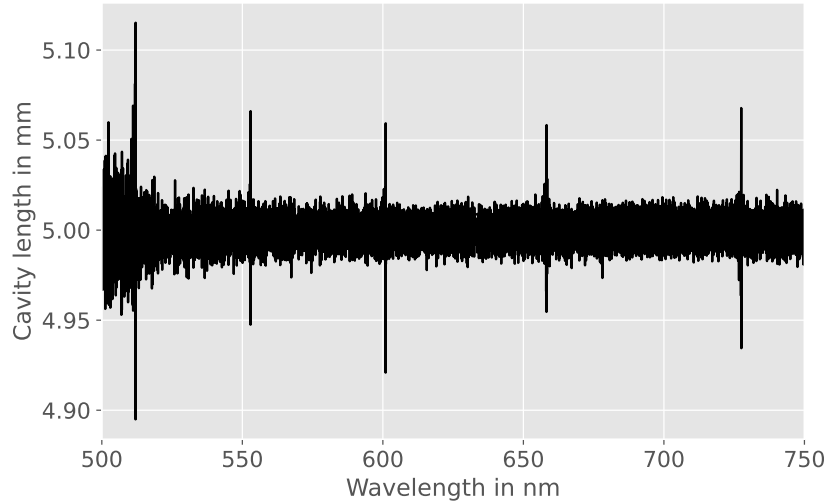
Figure 5.8: Effective cavity length variation as a function of wavelength. The periodic spikes seen in the data were traced to the SMPS power supply used for driving our broadband LED light source.

Wavelength obtained from FTS has also been used to determine the absolute interference order of FP transmission lines. For FP, a transmission maxima is obtained whenever interference condition is fulfilled, which is given by:

$$m\lambda_m = 2d\,, \tag{5.1}$$

where m is an integer called interference order, λ_m is the wavelength of transmission maxima and d is effective cavity width of FP.

We can only get a relative numbering k, from observed spectra, by count-

ing the FP lines. This is related to interference order m by the relation:

$$k = m - m1 \,, \tag{5.2}$$

where $m1$ is order of the first transmission peak.

We use the assumption that penetration depth is a smooth function of wavelength and hence a smooth function of relative interference order k (Bauer *et al.*, 2015). An initial guess for $m1$ can be made using Equation 5.1 with the value of effective cavity width d and wavelength of the first peak. With the initial guess for $m1$, a set of values of effective cavity width is obtained, which is modelled by fitting a cubic spline. This process is repeated by varying the value of $m1$. Average effective cavity width is calculated for each $m1$ value from the fitted data and the difference between the effective cavity width and average effective cavity width is obtained. Plotting this difference in cavity width as a function of relative peak number using the correct value of $m1$ will give distribution of data points around a nearby constant value. A positive slope is produced for small value of $m1$ and a negative slope for large value of $m1$, as suggested by Bauer *et al.* (2015). The value of $m1$ which gives minimum penetration depth variation is chosen, which is $m1=13332$ as seen from Fig. 5.9.

5.3 FP test with VBT Echelle Spectrograph

5.3.1 High resolution Echelle spectrograph on Vainu Bappu telescope

The Echelle Spectrograph installed on 2.3 m Vainu Bappu Telescope (VBT) in Kavalur, India is a general purpose spectrograph. It is designed for performing high-resolution spectroscopic observations, including stellar abundance analysis, the study of pulsating variable stars, the determination of chemical abundances of stars, and probing stellar and galactic kinematics.
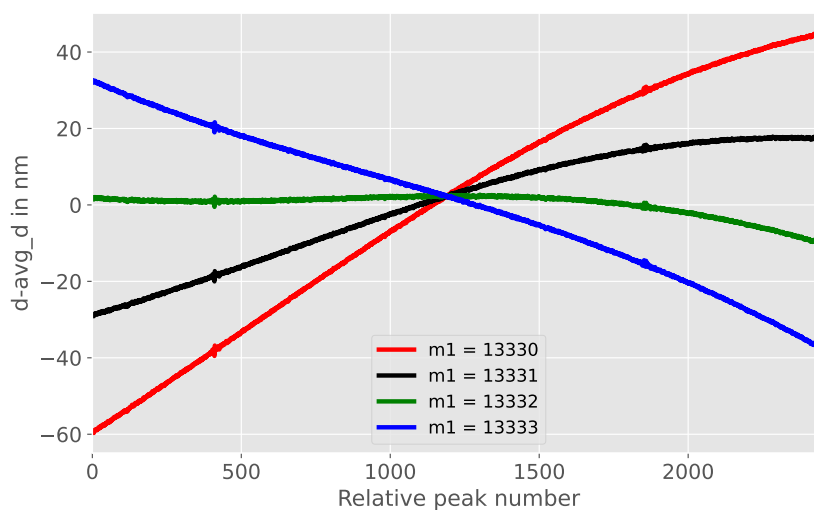
Figure 5.9: Difference between the effective cavity width(d) and average effective cavity width(avg_d) for different absolute interference order numbers $m1$. The green curve corresponding to $m1 = 13332$ shows the minimum variation.
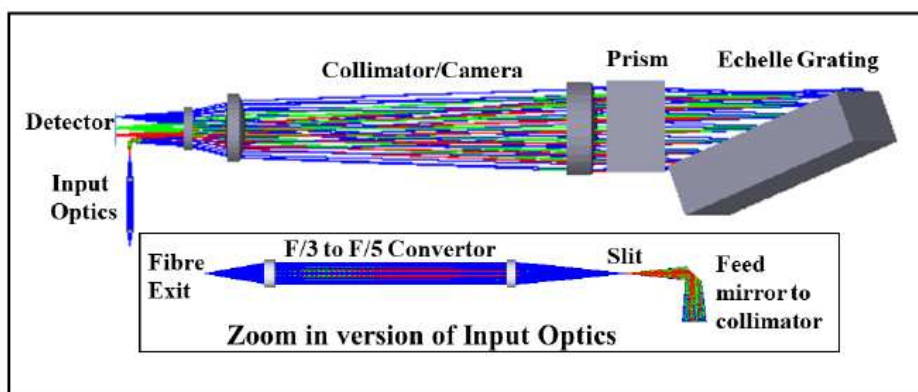
Figure 5.10: Optical design of the spectograph showing different components. Input optics to the spectrograph slit is shown in the zoomed in version. Credit: Sireesha *et al.* (2019)

The optical layout of VBT Echelle spectrograph is shown in Fig. 5.10. Light from f/3 primary of the telescope is fed into a 45 m long 100 μm multimode fiber placed at telescope prime focus. Light at the fiber exit is focused by f/3 to f/5 converter input optics onto the slit. Light passing through the slit is collimated using an f/5 collimator of focal length 755 mm and directed to cross dispersing prism. The prism's output is given to echelle grating with a groove density of 52.67 grooves/mm. The reflection grating operates in quasi-littrow mode and feeds light back into the cross dispersing

prism. The collimator acts as a camera in the return path, focusing light onto a 4k × 4k CCD. VBT echelle spectrograph is a low-cost, compact instrument that utilizes collimator and prism in double pass (N.K.Rao *et al.*, 2005).

Table 5.1: Spectrograph component specification (Sireesha C. *et al.*, 2018)

Component	Specification
Collimator	Field of view: 60mm diameter, Focal length: 755mm
Cross dispersing prism	Apex angle: 40°, Base size:126 × 165mm
Echelle Grating	Groove density: 52.67 grooves/mm, Blaze angle: 70°

The specification of the major spectrograph components are tabulated in Table 5.1. The echelle grating operates at a blaze angle of $\theta_B = 70°$ (N.K.Rao *et al.*, 2005) allowing a resolution of R=60,000. Wavelength coverage offered by the instrument is 4000-10,000 Å with a limiting magnitude of V≤10. Iodine absorption technique has been implemented for precision RV studies (Sireesha *et al.*, 2018). Long term stability of the spectrograph is not yet established due to it being a general purpose instrument. However, a drift of about ±1 pixels (±1000 m/s) (Sireesha *et al.*, 2019) is observed over several nights.

The spectrograph operates in quasi littrow mode with θ=1.1° (N.K.Rao *et al.*, 2005). Prism placed in the light path before the grating causes partial dispersion of light before passing it on to the grating. This results in an out-of-plane angle of grating, which causes a tilt in slit image as a function of wavelength at the detector (Sireesha C. *et al.*, 2019). This tilt limits the Radial Velocity (RV) precision achieved by the spectrograph. Distortion in the system has been modelled and estimated to be 400 m/s (Sireesha *et al.*, 2019).

5.3.2 Results

Preliminary test of the etalon has been conducted at VBT. The FP spectra was taken at normal temperature and pressure. Rail based design scheme for holding the FP and related optics, has been used for the purpose of this test as shown in Fig. 5.11. The output from the FP was fed to the calibration fiber that carries light to the telescope, from where it is picked up by another fiber and fed to the spectrograph.

OUTPUT TO SPECTROGRAPH   **FABRY-PEROT ETALON**   **INPUT FROM LIGHT SOURCE**
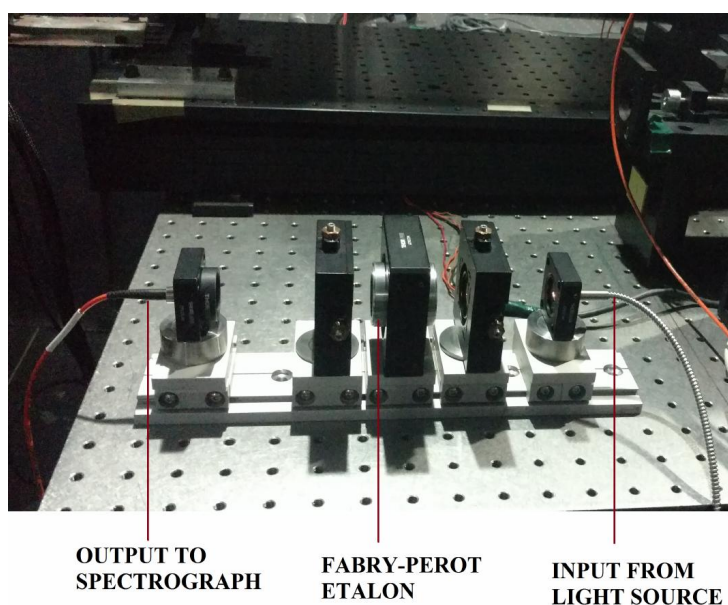
Figure 5.11: Image of the setup used for taking FP spectra with VBT Echelle spectrograph.

Fig. 5.12 shows the spectra obtained from the Echelle spectrograph using a 200 μm optical fiber to illuminate the FP. Total number of FP lines detected were 2617.

Gaussian profile is fit to individual FP lines and the FSR and linewidth at each wavelength is determined from the data. The values of FSR and linewidth of FP were found to be more than the values obtained from FTS data. Upon further inspection, we found that the broadening was caused due to misalignment errors and finite fiber divergence as explained in section 3.4. We changed the input fiber to a 100 μm core diameter fiber and used a laser
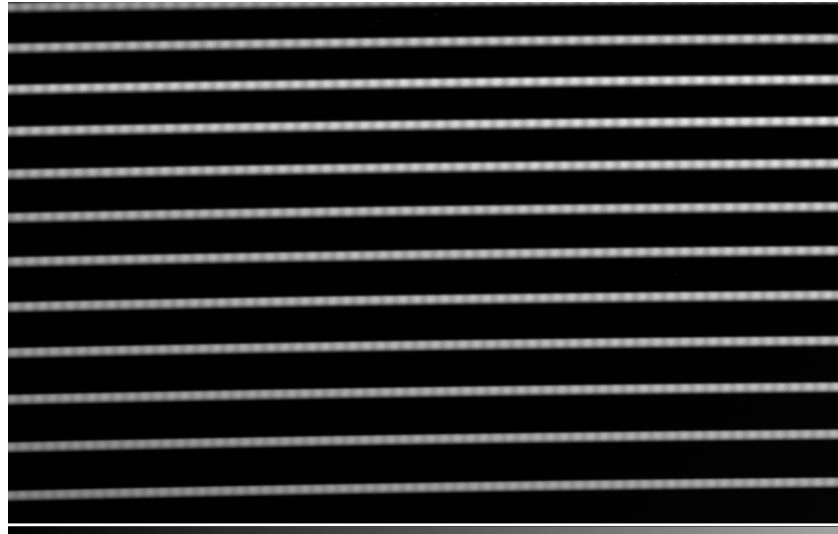
Figure 5.12: Fabry-Perot spectra obtained from VBT Echelle spectrogaph using a 200 μm optical fiber at the input.

and a 10 μm fiber setup for alignment of the optics with FP. We observed a significant improvement in the FP output data. Fig. 5.13 shows the two-dimensional spectra of FP as observed with VBT Echelle Spectrograph. A total of 4032 FP lines were detected across 20 orders of the spectrograph.
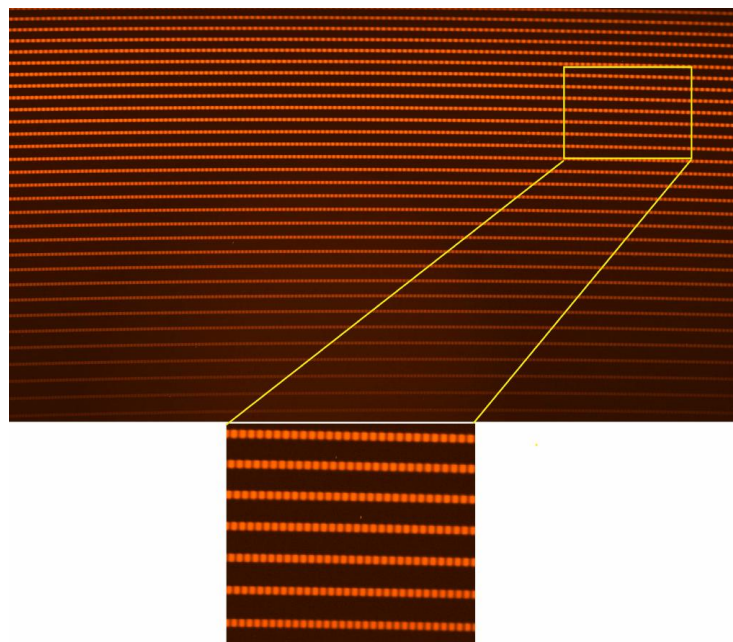
Figure 5.13: High Resolution spectra of FP obtained from VBT Echelle, taken at normal room temperature and pressure. Top panel: Full CCD frame of the spectra. Bottom Panel: Zoomed-in view showing the FP lines.

The FSR and FWHM of the FP lines across each order were calculated and have been plotted in Fig. 5.14 and Fig. 5.15 respectively.
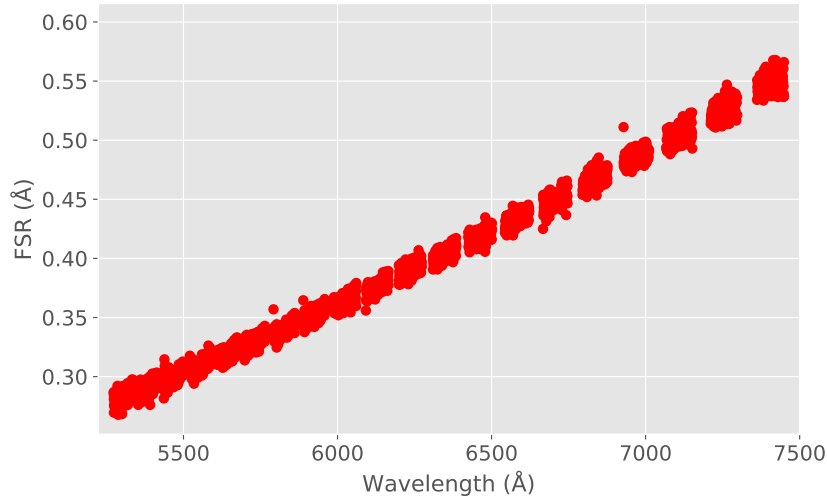
Figure 5.14: FSR of the FP lines plotted with respect to the wavelength, for the identified orders. The gaps in the data are attributed to wavelength breaks from order to order.
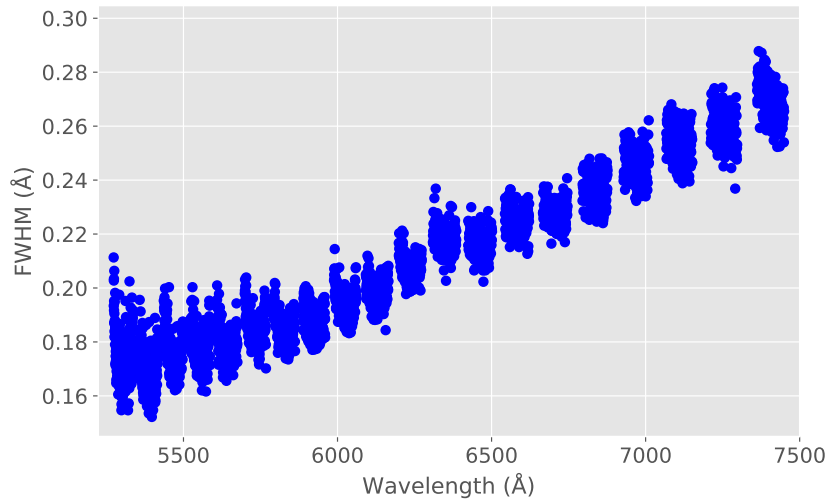
Figure 5.15: FWHM of the FP lines plotted with respect to the wavelength, for the identified orders. The gaps in the data are attributed to wavelength breaks from order to order.

On analysis of the spectra, we observed almost no change in the Free Spectral Range (FSR) of FP. However, a significant increase in the FWHM of the FP lines was noticed, which has been shown in Fig. 5.16. VBT Echelle Spectrograph is a general purpose spectrograph which is not temperature

and pressure stabilized. The stability issues faced by the spectrograph have been discussed in detail in Sireesha C. *et al.* (2018). The FP data obtained from this, hence showed blended lines in first 300 Å of the wavelength range (hence, discarded), increased line width along with curvature in all orders and artifacts at the edges, as seen in Fig. 5.17.
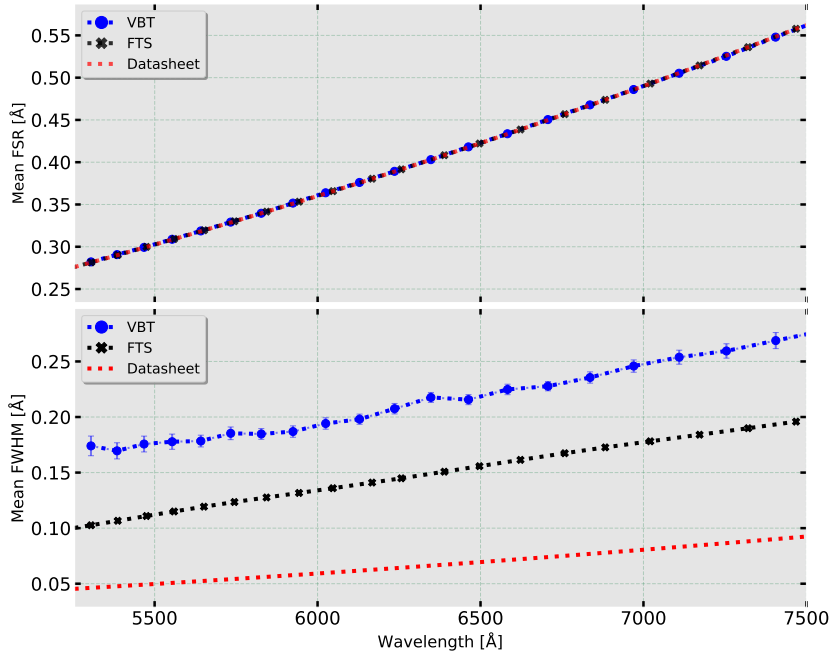
Figure 5.16: Top panel: The FSR determined from FP transmission spectra taken with VBT, high-resolution FTS and the expected values computed from the etalon parameters specified in the FP datasheet. Bottom panel: FWHM computed from VBT spectra, FTS data and the expected value determined based on datasheet parameters. We see a significant increase in the FWHM values for VBT data. The FSR of the FP lines remain unchanged.

5.4 FP installation on Hanle Echelle Spectrograph

5.4.1 Hanle Echelle Spectrograph (HESP)

HESP is a high-resolution general purpose spectrograph designed to perform a wide range of scientific studies, including the capability to conduct RV studies of host stars of exoplanet (Sriram *et al.*, 2018). It is installed on the 2 m
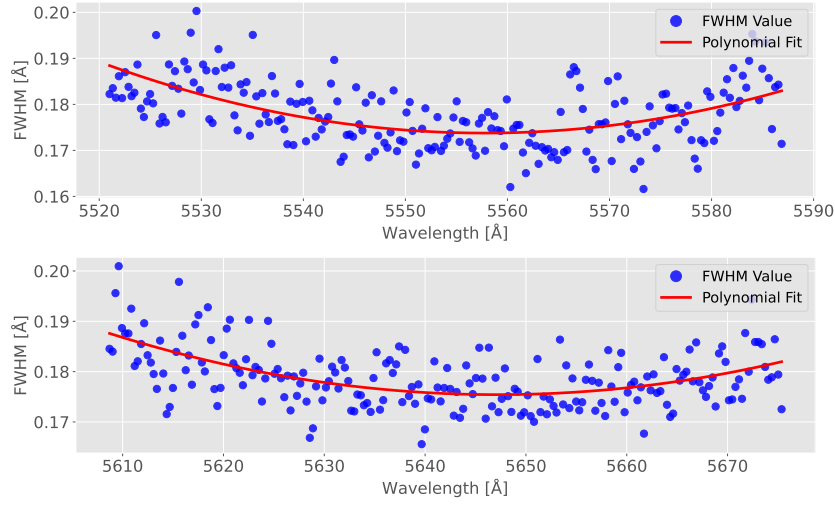
Figure 5.17: The FWHM of Fabry–Perot lines obtained in two adjacent orders showing scatter at the edges. The red line shows a second order polynomial fit to the data to depict the curvature in FWHM.

Himalayan Chandra Telescope (HCT), located at Indian Astronomical Observatory (IAO), Hanle, which lies at an altitude of 4500 m above sea level. HESP covers a wavelength range of 3500-10000 Å. HESP operates from a temperature stabilized room with temperature kept at 16°C. It works in two modes: low-resolution mode (R=30000) and high-resolution mode (R=60000). The spectrograph comprises of four units:

- Cassegrain unit (CU): mounted on one of the telescope's side ports, the CU acts as an interface between the spectrograph and telescope.

- Spectrograph unit: mounted on a vibration isolated optical table in a temperature-controlled environment

- Calibration unit: houses wavelength calibration lamps and flat lamps with color balancing filters. Light from this unit is carried to CU at the telescope using calibration fibers.

- CCD detector system: It is a 4k × 4k E2V-231-84 LN2 cooled detector with 15 μm pixel size.

The optical layout of HESP is shown in Fig. 5.18. The spectrograph design is based on while pupil layout. f/9.2 beam from HCT first passes through a

pair of atmospheric dispersion correctors. The beam is converted to f/3.6 and fed to the fiber using two identical lens doublets. At the exit of the science fiber, three lenses produce an f/75 beam for the image slicer. The slicer used is a modified version of the classic Bowen-Walraven image slicer. The slicer is used only in high-resolution mode, R=60000. Regardless of mode, a large field lens gathers the light, and with the help of a small doublet lens, it forms a telecentric image at the slit.
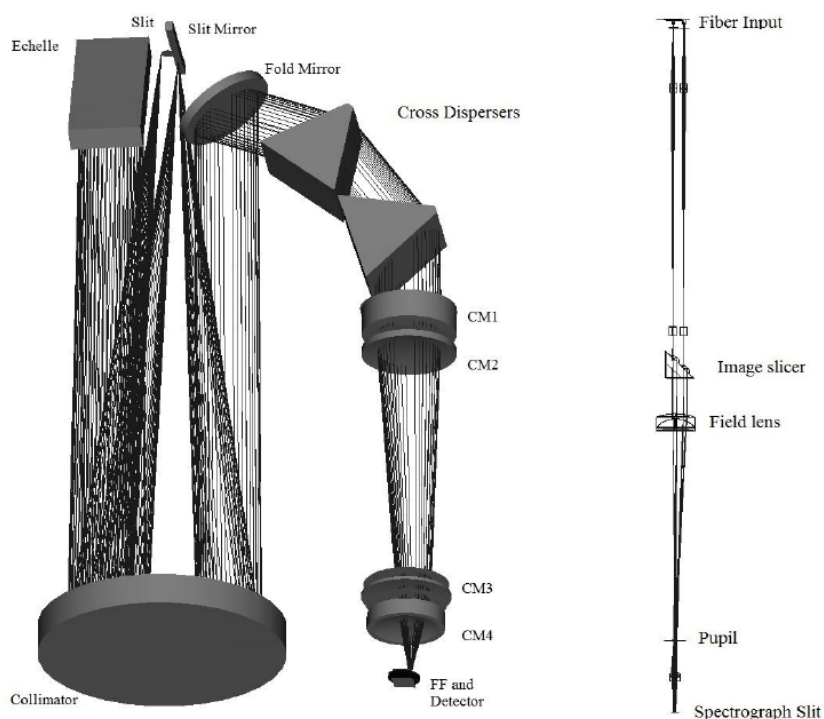
Figure 5.18: Optical layout of Hanle Echelle Spectrograph. Credits: Anantha C. *et al.* (2015)

The spectrograph is made into a compact system by using a folding mirror arrangement. HESP uses a collimator in triple pass with baffling to separate incoming and reflected beams from the collimator. Input beam from spectrograph slit is f/10.45 and is collimated by an off-axis portion of a 1850 mm focal length parabolic reflective collimator. The R2.15 echelle grating with 52.67 lines/mm and two cross dispersing prisms having an apex angle of 55° produces a required wavelength coverage but with considerable wavelength overlap in successive orders.

Finally, the cross-dispersed orders are imaged onto the detector using an f/2.7 camera. The detector has been tilted to take care of the achromatic requirement on the camera and improve the overall state of correction (Sriram *et al.*, 2018), causing an overall global tilt in the spectra. Apart from the global tilt and a small tilt introduced due to curvature of orders, the optical design of HESP does not introduce any large tilt into the individual spectral lines. The specifications of the spectrograph are summarized in Table 5.2.

Table 5.2: Specifications of Hanle Echelle Spectrograph (HESP). (Sriram *et al.*, 2018).

Spectral Coverage	3500-10000 Å
Echelle grating	R2.1
Resolution	30000 (without image slicer) 60000 (with image slicer)
RV Accuracy	20 m/s with dual fiber mode
Stability	200 m/s (over a night)
Efficiency (includes telescope)	∼22% peak (at ∼600 nm)

5.4.2   Results
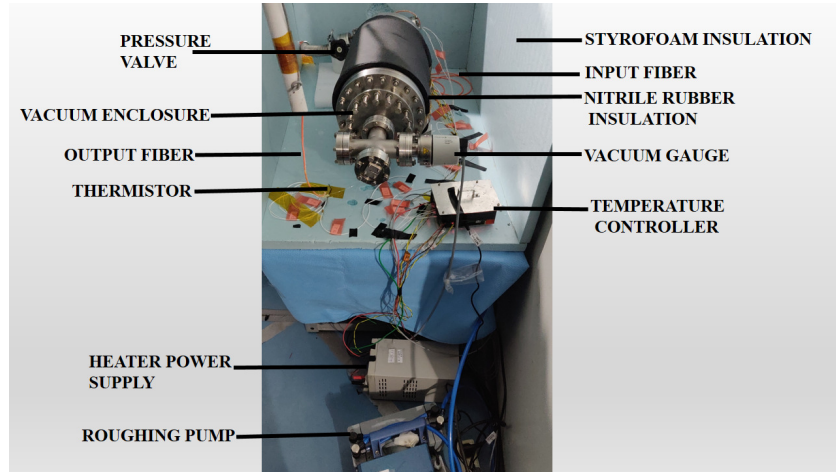
Figure 5.19: FP setup installed in the spectrograph room at Indian Astronomical Observatory, Hanle.

Fig .5.19 shows the etalon based calibration system installed on HESP. The FP is kept in a temperature controlled vacuum chamber with two layers of thermal insulation. The operating temperature for FP is 19°C and operating

pressure is 2.5×10^{-2} mbar. The output from the FP is fed to the calibration unit through a fiber of 100 μm size. The calibration unit holds the flat and Th-Ar light sources and the main calibration fiber of 100 μm size that carries light into the spectrograph. The calibration unit has been shown in Fig. 5.20.

1. FP output fiber
2. Collimating lens
3. Flat lamp
4. Th-Ar lamp
5. Calibration fiber
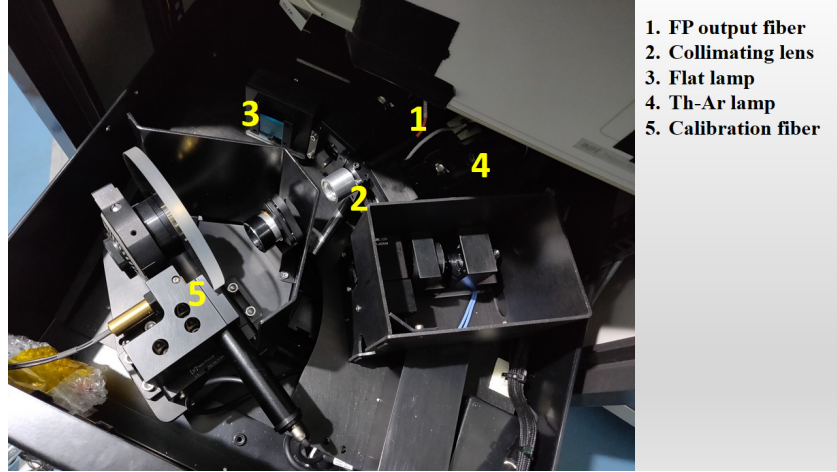
Figure 5.20: Calibration rack of HESP with the FP output fiber integrated into the rack.

A zoomed in version of the spectra obtained from HESP in low resolution mode (R=30,000) is shown in Fig 5.21. The spectra obtained in high resolution mode (R=60,000), is shown in Fig. 5.22, the split in the lines indicating the use of an image slicer. FP lines were found across 22 orders of the spectrograph.

Gaussian profile is fit to individual FP lines and the FSR and line-width at each wavelength is determined from the data, which has been plotted in Fig. 5.23 and Fig. 5.24 respectively. Total number of FP lines detected were 6624 across the wavelength range 500-750 nm. Initial level of calibration of FP data has been done using Th-Ar to determine the wavelength of FP lines.

Preliminary reduction and analysis of FP calibration frames have been carried out in IRAF (Doug T., 1986, 1993) and Python. It is observed that the FSR values match the expected value from FTS observation and datasheet prediction, shown in Fig. 5.25. However, the FWHM shows an increase in value compared to FWHM values obtained from FTS observation and as expected from datasheet calculations, as seen in Fig. 5.25. Since HESP is
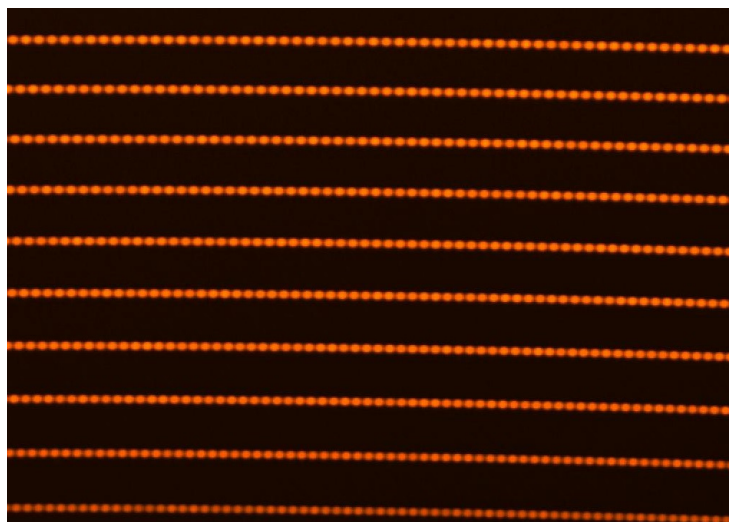
Figure 5.21: Fabry-Pérot spectra obtained from HESP at low resolution, R = 30,000. A part of the spectra is presented here to show the FP lines clearly. Low resolution mode of HESP does not use an image slicer.
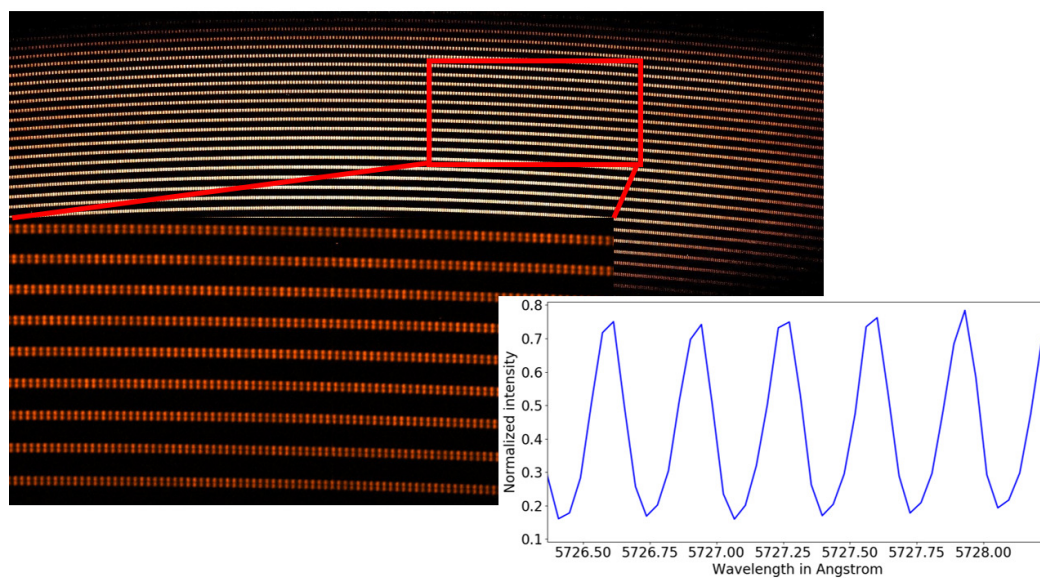
Figure 5.22: A high resolution (R=60,000) Fabry-Pérot spectra obtained from HESP. Top panel: A full CCD frame of the spectra. Bottom left panel: Zoomed in version focusing a part of the spectra. Bottom right panel: Portion of an extracted spectral order showing the well resolved FP lines.

temperature stabilised, the FWHM values obtained are lesser than the values obtained from VBT. This decrease is also due to the fact that the FP with related optics was operating in a temperature and pressure controlled setup, thereby solidifying the need for environment control.
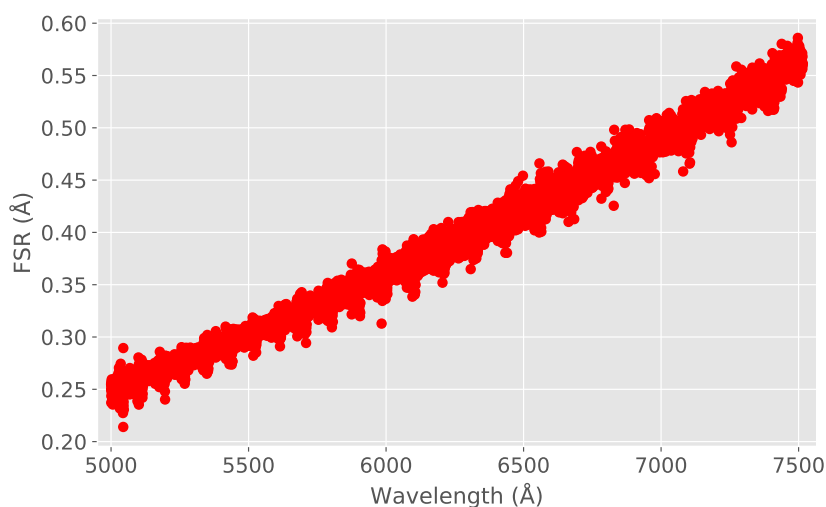
Figure 5.23: FSR of the FP lines plotted with respect to the wavelength, for the identified orders. HESP design causes significant overlap between subsequent orders.
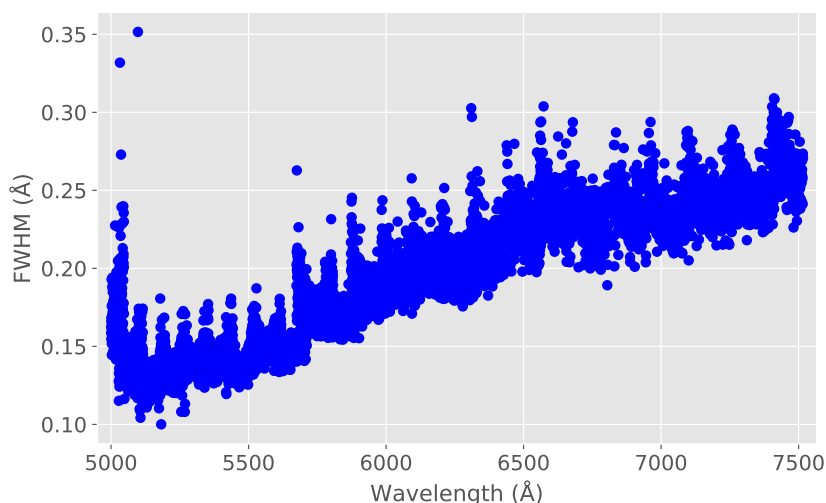
Figure 5.24: FWHM of the FP lines plotted with respect to the wavelength, for the identified orders. HESP design causes significant overlap between subsequent orders.

Examination of FP calibration frames show that the spectrograph has a characteristic presence of field curvature and distortion introduced by the optics. Along with the increase in values, we have observed a curvature in FWHM in all the orders of the spectra. Apart from this, the instrumental artifacts are also seen at the edges of each order as shown in Fig. 5.26. This opens up new possibilities of spatially mapping the spectrograph point-spread function and other artifacts from the FP spots. Incorporating such input
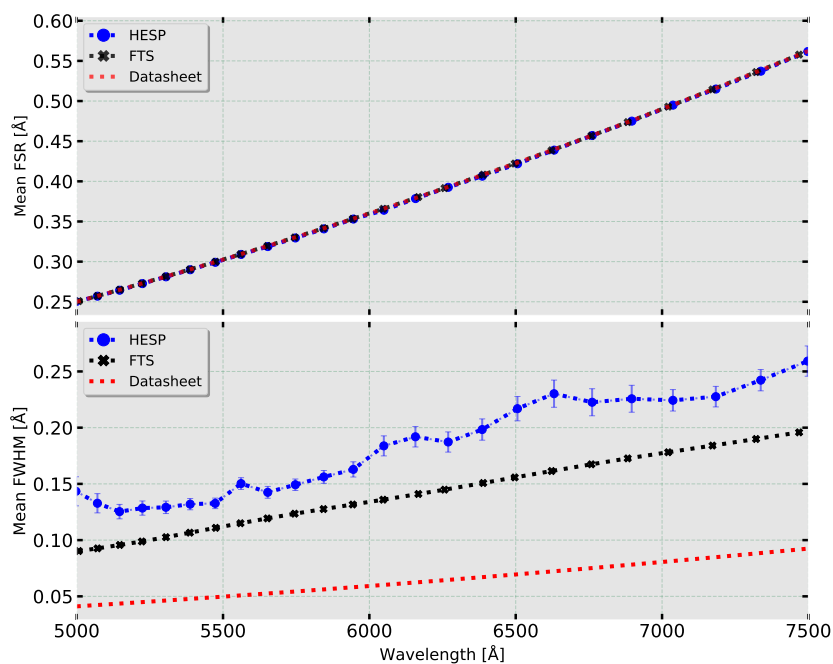
Figure 5.25: Top panel: The FSR determined from FP transmission spectra taken with HESP, high resolution FTS and the expected values computed from the etalon parameters specified in the FP datasheet. Bottom panel: FWHM computed from HESP spectra, FTS data and the expected value determined based on datasheet parameters. An increase in the FWHM values for HESP data is observed. The FSR of the FP lines remain unchanged.

would help us in developing a better wavelength solution for the spectrograph.
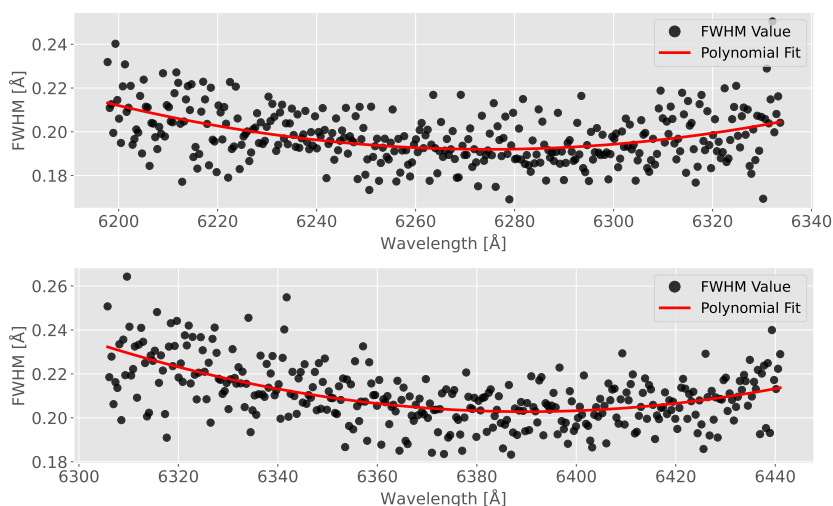
Figure 5.26: The FWHM of Fabry–Perot lines obtained in two adjacent orders showing scatter at the edges for HESP data. The red line shows a second order polynomial fit to the data to depict the curvature in FWHM.

5.5   Discussion

We have conducted preliminary tests of the FP based calibration system with FTS, VBT Echelle Spectrograph and have installed the setup and tested it with HESP. Table 5.3 shows the comparison among values for finesse and cavity width as obtained from the test data.

Table 5.3: Comparison of FP parameters obtained from datasheet, FTS and HESP.

FP Parameter	Datasheet	FTS test	VBT data	HESP data
Cavity Width	5 mm	4.999 mm	4.993 mm	5.002 mm
Finesse	6	2.73	1.88	2.16

The observed differences in the values can be attributed to the degradation of optical coating of the FP since its purchase 5 years back. We have used 100 μm fibers for illuminating FP for the tests, thereby the loss in finesse can also be due to the finite size of the optical fibers. During the analysis of the test results from HESP, we observed artifacts like curvature and tilt in lines in the spectra, increasing the value of line-width to more than the expected value, thereby reducing the effective finesse of the FP. This aspect is discussed in detail in Chapter 6.

Since FP is a stable source that provides a large number of uniformly spaced lines of equal intensity, the artifacts and aberrations of spectrographs clearly show up in the reduced data. This can help in better prediction and removal of artifacts of the instrument, leading to a better estimation of the final wavelength calibration model.

Chapter 6

Curvature and tilt correction of high resolution spectra [1]

6.1 Introduction

The benefits provided by echelle spectrographs also come with several short-comings. In order to accommodate the spectra effectively on the detector, optical components, such as slit or camera, are often adjusted, leading to the introduction of artifacts and aberrations like distortion, defocus and tilted lines. Curvature in the spectrograph orders can arise due to the cross disperser, whose dispersion direction is perpendicular to the Echelle grating (Sireesha C. *et al.*, 2018). The tilt in individual lines in the spectrum are caused due to the cross disperser and Echelle grating working on two different planes (operating in quasi-Littrow mode). During post-processing, most of these factors are neglected, which leads to the addition of errors.

The presence of tilt in calibration and spectral lines are an artifact that can add unwanted error to the final result if not taken care of in post-processing. In general techniques, the binning of data is done normal to the dispersion

---

[1] *Part of the work presented in this chapter is submitted to Tanya Das et al., Applied Optics Journal 60, 2021.*

axis, and hence if the tilt in spectral lines is not considered, the resulting 1D data may show an increase in the FWHM of the lines and also cause blending in some cases. This is because, in the case of tilted lines, the intensity is distributed over several pixels, which, when binned along the slit direction, gives a broadened line and wrong flux values, as shown in Fig. 6.1. The broadened spectral line also results in the degradation of spectral resolution.
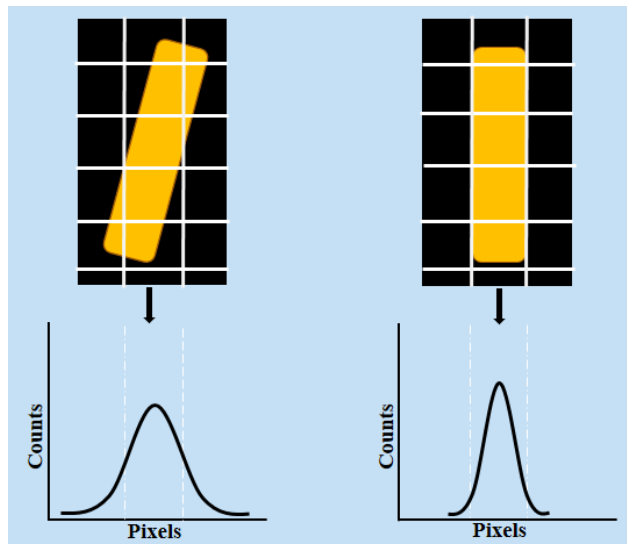
Figure 6.1: A cartoon depicting the effect of tilt on the FWHM of the lines.

The tilt in the slit image at the detector is a function of wavelength (Robinson & Latham, 1988). It also compromises the attainable accuracy in RV measurements if not adequately taken care of or modelled by the extraction software (Ireland *et al.*, 2018). Disentangling the tilt related shifts in line centroid position from the RV shift is essential for RV studies. The point spread function (PSF) is predominantly the response of the instrument to an object or point source. The instrumental aberrations of the system already broaden the energy distribution for the point spread function (PSF). The tilt is an artifact of the system, which causes further broadening of the line. Removal of this artifact can hence facilitate the effort of predicting instrument PSF by removing one of the dependent factors, in cases where it is necessary to generate a PSF map of the instrument and its variation during an observation run. Measuring the tilt can also help in the study and estimation of

instrument aberrations, for example, a better prediction of distortion in the system.

We have used FP and Th-Ar calibration data to assess and remove the tilt and curvature being introduced by the instrument. Spectrographs like Magellan Inamori Kyocera Echelle (MIKE) spectrometer (Bernstein *et al.*, 2003) and X-shooter (D'Odorico *et al.*, 2006) show highly tilted spectral lines. The tilt removal algorithm developed as part of this study has been tested on X-Shooter and MIKE Th-Ar calibration data.

6.2 Review of existing techniques for tilt and curvature removal

In order to obtain calibrated science quality data, the two-dimensional spectrograms obtained from the spectrograph have to be processed and the spectrum extracted. Software like IRAF Doug T. (1986, 1993) can be used for general reduction purpose. Many spectrographs have dedicated state of the art pipeline for preparation and reduction of the 2D spectra. A brief description of the method adopted in X-Shooter and MIKE pipeline has been discussed along with a new algorithm called PyReduce developed for the same purpose.
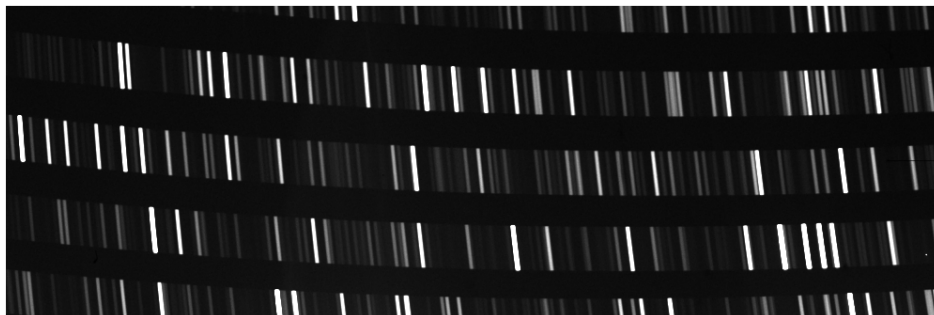
Figure 6.2: Zoomed in Th-Ar calibration spectra from X-Shooter showing highly curved orders along with large tilt in spectral lines.

X-Shooter is a single target spectrograph of medium resolution (R∼ 4000-

17000), installed at the Cassegrain focus of ESO's Very Large Telescope (VLT) (Vernet *et al.*, 2011). The output of this spectrograph consists of highly curved orders with tilted spectral lines, shown in Fig. 6.2. Due to this, special measures are taken for wavelength calibration and optimal extraction of the spectra, as described in Goldoni *et al.* (2006, 2008). X-Shooter pipeline is written in ANSI C. Separate pinhole mask arc frames are taken for computation of initial guess for wavelength solution and determine spatial and wavelength scale calibrations. A polynomial interpolation, constructed using multi-pinhole frame, is used for transforming detector coordinates into a function of wavelength (determined by the guess solution), order number and position on the slit that allows the removal of order curvature and line tilts. The physical model of the instrument can also be used to determine the wavelength position on detector. Finally, the detector pixels are oversampled in 2D and linear interpolation is used to find the slit profile which is then collapsed over user defined slits. A detailed description of the entire pipeline can be found in Modigliani *et al.* (2010).

The Magellan Inamori Kyocera Echelle (MIKE) is a high resolution, double echelle spectrograph installed on the Magellan II telescope at Las Campanas Observatory, Chile. Fig. 6.3 shows the Th-Ar calibration spectra as captured in the red arm for a slit size of 0.7 inches. A dedicated pipeline is available for data reduction (Bernstein'*et al.*, 2015) using IDL with a Python alternative. After the standard image processing involving overscan removal and flat fielding, a 2D wavelength image is generated by using Th-Ar arc frame to derive a 1D wavelength solution along the center of each order. For each order, the high SNR arc lines are identified and their tilt is measured as a function of wavelength and echelle order. The centroid of each line is traced across the order and best fit line for each arc line is used to calculate the slope. A 2D Legendre polynomial is fit to the calculated slopes for every order and the slope values interpolated from the solution for areas with less density of Th-Ar lines. A unique wavelength is assigned to the center of all

the pixels falling within the echelle order by using the derived wavelength solution and the arc line tilts. This is done across full CCD pixels and a wavelength image is generated which is finally used in the optimal extraction of the orders. A similar method is adopted by MAGE Spectral Extractor (MASE) (Bochanski *et al.*, 2009)
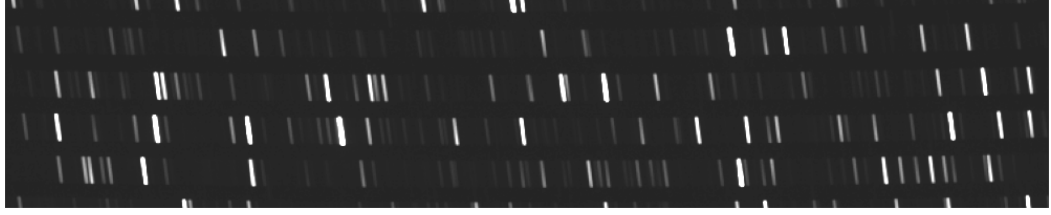
Figure 6.3: Zoomed in Th-Ar calibration spectra from red channel of MIKE at 0.7" slit setting, showing tilted lines.

The new REDUCE package (Piskunov *et al.*, 2021) adds to the earlier version of the developed package (Piskunov & Valenti, 2002) by incorporating tilted and curved slit images. The method follows a slit decomposition algorithm, where the 2D image of the spectral order is represented by slit illumination and spectrum, sampled on the detector. The shape of slit image is modelled by taking strong and unblended emission lines in a wavelength calibrated spectrum and fitting a 2D Gaussian to each of the line image. The tilt and curvature variations across the order is combined by fitting a polynomial and interpolating to all the columns. Optimal extraction is then performed keeping in mind the calculated tilt and curvature.

All data reduction pipelines are spectrograph specific and involves complex mathematical modelling that focuses on the overall optimal extraction of the science spectrum by incorporating for the tilt and curvature while extracting the spectrum. For example in case of X-Shooter, separate multi-pinhole exposure frames are used to prepare a mathematical model for tilt and curvature in spectrum. In case of MIKE, only high SNR Th-Ar lines are used to calculate line tilts, which is then interpolated to predict line tilts across the order. The proposed method has been primarily developed for HESP spectrograph, which has no tilt and curvature correction currently employed

in the pipeline, hence it will act as a new addition to the pipeline. The algorithm discussed in this paper takes a much simpler approach, using image processing methods to calculate and correct for the lines.

6.3   Methodology and algorithm

We have developed a routine that corrects the curvature in spectra and removes the tilt of the individual spectral lines. Image processing tools in Python, namely, Scikit-Image (Van der Walt *et al.*, 2014) and OpenCV (Bradski *et al.*, 2000) were used for this purpose.

6.3.1   Aperture Tracing

The first step in the process is to identify the position of all the apertures in the spectra. The position of all these apertures are saved as higher-order polynomials (2 or above), depending on which, the apertures are then extracted. This is called tracing of the apertures, and a continuous spectrum like that of a flat lamp is used for this purpose. Tracing of apertures was performed following the CERES routines described in Brahm *et al.* (2017). The traced aperture for HESP is shown in Fig. 6.4, where the global tilt in the spectra discussed in 5.4.1 can be observed.

6.3.2   Order extraction

After all the apertures were traced, they are extracted in the next step. The aperture size ($apsize$) was chosen based on the extent of every aperture in the cross dispersion direction. While choosing the aperture size, the inter-order separation in the spectra is kept in mind in order to avoid any overlapping of the mask with consequent orders. Intensity values in the aperture were extracted by creating a mask using Bivariate Spline (Zhou *et al.*, 2013) and sampling at every 0.5 pixels. Mask extent was decided from ($y0 - apsize/2$)
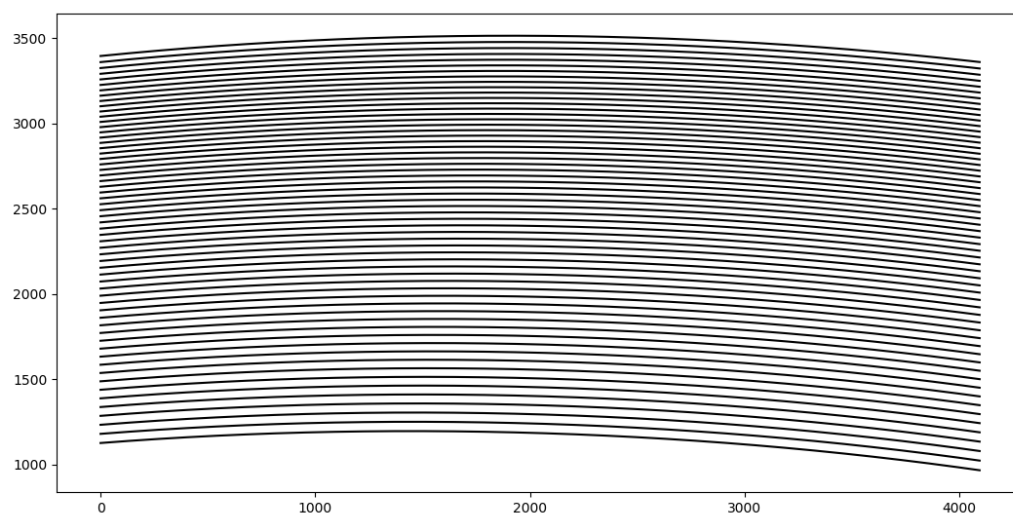
Figure 6.4: Apertures detected from flat lamp spectra for HESP. A total of 55 apertures were detected. The global tilt in the spectra is discernible in the figure.

to $(y0 + apsize/2)$ in step size of 0.5, where y0 is the traced polynomial. An example of the traced mask is shown in Fig. 6.5.

Figure 6.5: Aperture extraction mask, in red, over plotted on the spectra, for one particular order. There is no overlap of the mask with neighbouring orders.

6.3.3   Curvature removal

Correction of the tilt in individual spectral lines should be preceded by curvature and global tilt removal, if any. For removing the curvature and straightening the new array, extracted points were stored in a separate array row-wise. The intensity data extracted from the first row was stored in the first row of the new array and so on. Stacking each straightened aperture in order of their extraction reproduced the entire spectra without the curvature. Part of the spectra before and after curvature removal is shown in Fig. 6.6.

Original spectra

Curvature removed spectra
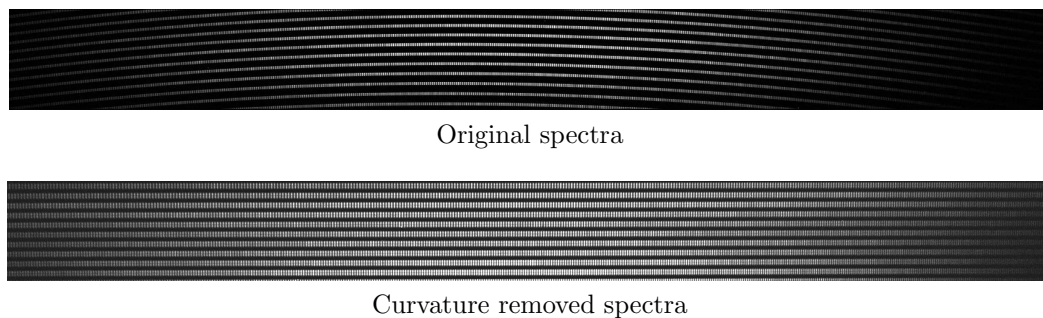
Figure 6.6: Depiction of the curvature and global tilt correction in HESP. Top: Part of the original spectra with curvature. Bottom: The curvature corrected and stacked aperture frames.

6.3.4 Tilt calculation and removal

The tilt is now computed in curvature removed result. Routine was tested on both FP and Th-Ar calibration frames (in X-Shooter and MIKE). Since the spectra have lines with distinguishable edges, we have used the Canny edge detection technique (Canny, 1986) for determining the boundaries of each tilted line. The correction was performed individually on each aperture. The selection, tilt calculation and correction procedures are entirely automated. The algorithm for tilt correction is as follows:

- Load the required aperture and take a central y-cut through the aperture.

- Smoothen the data obtained from y-cut using Gaussian smoothening, depicted in Fig. 6.7

- Detect the peak values in smoothened data and save the x-position corresponding to the peaks, plotted in Fig. 6.8. This generates position information for all the lines present.

- Calculate the difference between adjacent peak positions. This gives the separation between two peaks. Take the median value of differences obtained. Construct a boundary array with $xpeakposition \pm median/2$
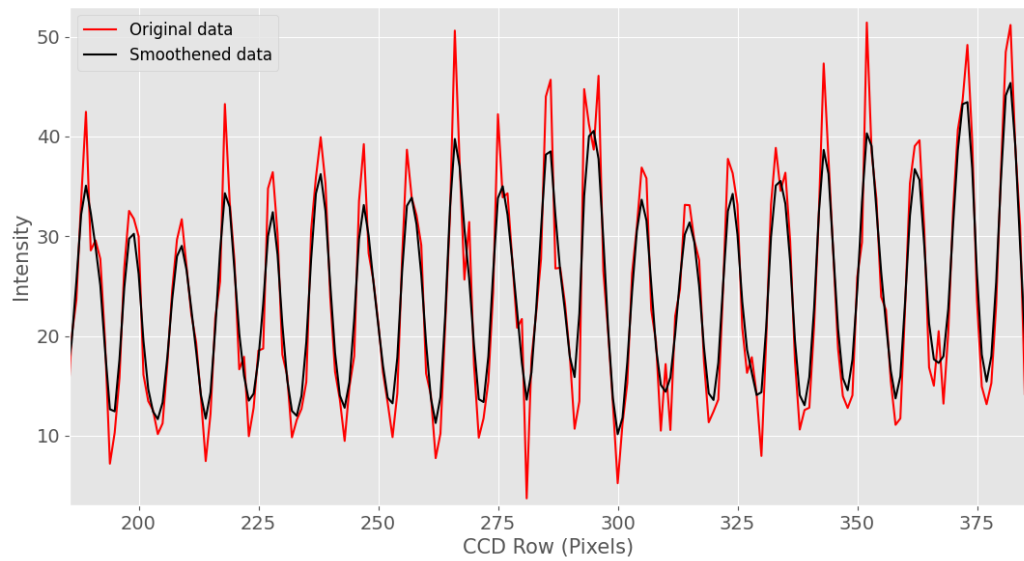
Figure 6.7: Application of Gaussian smoothening on reduced FP data from HESP. Red curve indicates the original FP data, black curve is the smoothened data overplotted on original. A zoomed version is presented to show individual lines clearly.
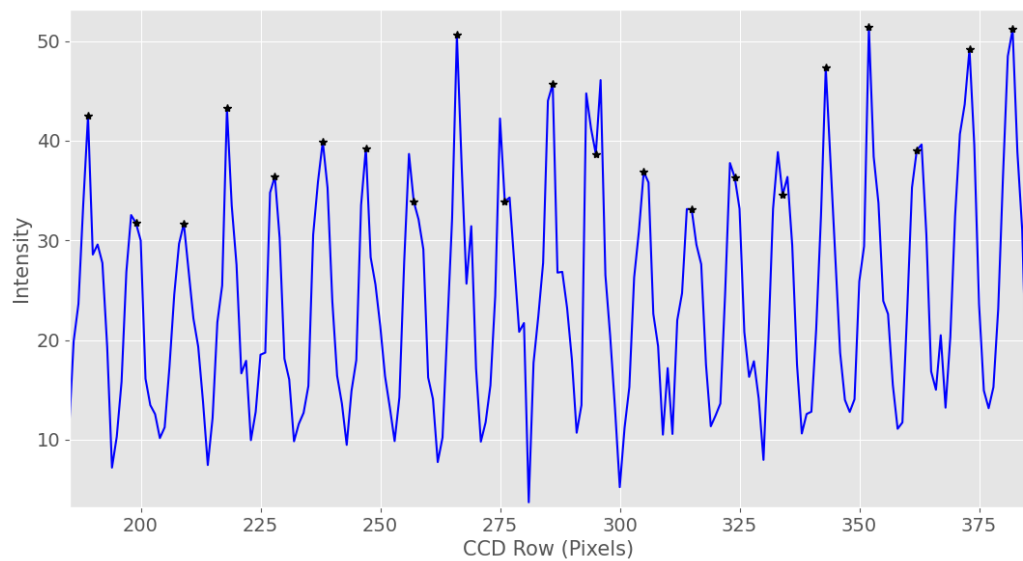
Figure 6.8: Detected peaks from the smoothened data marked with star on the orginal reduced FP lines from HESP. A zoomed version is presented to show the peak positions clearly.

being edge positions. This is done to avoid overlapping of each FP line boundary when the final corrected array is reconstructed.

- Use the boundary array to construct a box and isolate the region of interest in a separate array. Calculate the y-extent of the separated box

to include areas with FP data present and avoid background noise.

- Since Th-Ar spectra does not have equally spaced lines of uniform intensity, mean thresholding is performed, and a binary image is generated, example of which is shown in Fig 6.9. The transitions from 0 to 1 and vice versa determine the boundary array values mentioned in the previous step.

Original image

After binary thresholding
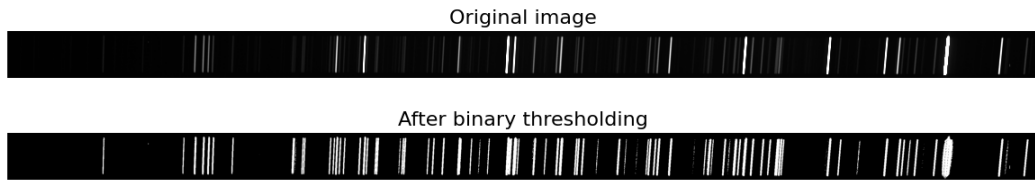
Figure 6.9: Binary thresholding performed on one of the apertures of X-Shooter Th-Ar calibration frame. This is done to detect medium SNR lines. Top: Original extracted aperture. Bottom: Result of Binary thresholding.

- The centroid and tilt angle (slope) are determined using function region prop in Scikit processing package on each calibration line. The centroid value is taken as the reference position (x0,y0).

- Every pixel is shifted with respect to the reference position (x0, y0) determined above, using Eq. 6.1 (Dubs & Schlatter, 2015; Dubs & Maeda, 2016). Function warp in the scikit-image processing tool is used for shifting pixels according to the calculated x_s value.

$$x_s = x' - (y' - y_0) \times slope \,, \qquad (6.1)$$

- The result of the algorithm applied on one tilted line is shown in Fig. 6.10. Top panel shows the corrected image and bottom panel shows the effect of correction on the FWHM of the line. The corrected line is stitched into the reconstructed main array using the boundary values determined before. This is done to make sure that the FSR of the data is not altered.

Tilt correction for single line

1D binned plot
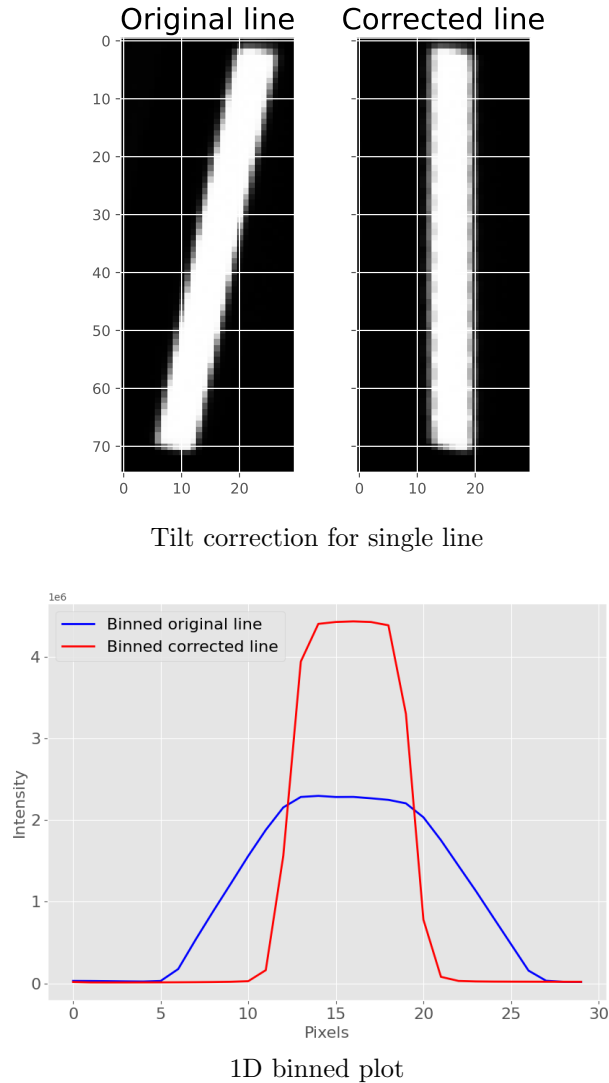
Figure 6.10: Representation of tilt correction. Top panel: Correction algorithm performed on one Th-Ar line to show how the tilt is removed. Original line shows the tilted line and corrected line is the result after correcting for tilt. Bottom panel: Binning done across y-axis to generate 1D plot for both the lines. It can be observed that the tilt correction drastically reduces the line-width from 12.44 before correction to 6.14 after correction.

6.4   Tilt correction results

The developed method has been tested on Fabry-Perot calibration spectra of HESP. In order to ascertain the capability of the algorithm, we looked into spectrographs with highly tilted lines and performed the tilt corrections on the Th-Ar calibration spectra from X-shooter and MIKE.

6.4.1   HESP

The FP calibration frame of HESP has been shown in Fig. 5.22. Tilt calculation is preceded by curvature removal and global tilt correction described in the previous section. FP lines exist across 22 orders of the spectra, and in Fig. 6.11 we show the representative plots for six orders: two top orders, two central orders and two bottom orders. The calculated tilt for FP lines is plotted along with a linear fit to the points. In HESP, we do not see a smooth variation in tilt angle after removal of curvature. The weak trend in the data, however, is still visible, as illustrated in the Fig. 6.11. The wavelength dependence of tilt is indicated by the slope of the linear fit to the tilt values, which increases from lower-order (7.75×10^{-6} for order 25) to higher order (1.46×10^{-5} for order 46). The tilt values are more scattered because the HESP design does not introduce a large tilt in the individual lines, causing the noise level in the spectra to come into the picture. For spectrographs in which it is known that the design introduces appreciable tilt, the scatter in the tilt angles are less, as will be seen in forthcoming sections.

Fig. 6.12 shows the uncorrected and corrected orders, plotted along with their similarity and difference image for one order. Structural Similarity Index (SSIM) is used to determine the similarity between two images, +1 indicating the most similar images and -1 indicating the images are very different (Wang *et al.*, 2004). SSIM image and difference image are computed between the original order and corrected order.

Since HESP does not show any visible tilt, the FWHM of each FP line across the order is plotted in Fig. 6.13 before and after the correction.

The number of lines that show a decrease in FWHM is determined and the finesse for every order is calculated. Not all the FP lines show a decrease in FWHM, especially the lines at edges, which can show an increase. This is because of low SNR at the edges due to the non-uniform illumination of the detector. Hence the correction is not performed effectively at these regions.
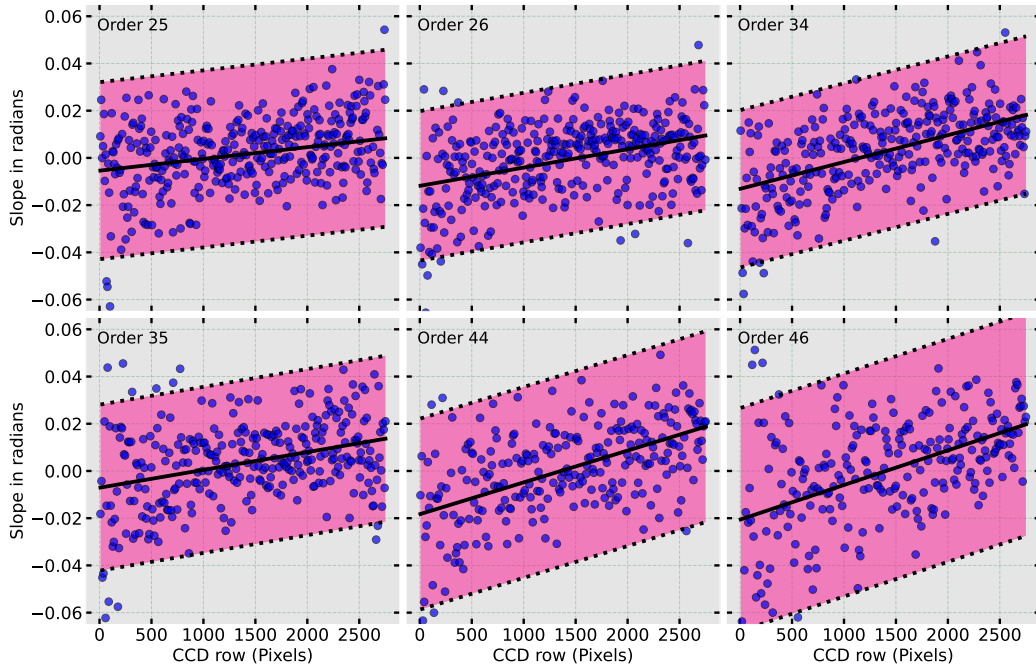
Figure 6.11: Tilt angle variation of FP lines across several spectrograph orders. The solid black line shows a linear fit to the data, and the dotted line shows a two sigma clipping boundary. Any point outside this boundary is rejected as an outlier during the fit. The scatter in the plot indicates the low tilt value in HESP spectra.

A total of 6624 FP lines were detected across 22 orders with this algorithm, and a reduction in FWHM of 5417 lines was observed after using the tilt correction procedure, thereby correcting 82% of the lines. The overall finesse value also improves from 2.167 to 2.208. The FWHM and finesse values for all orders are tabulated in Table 6.1.

6.5   X-Shooter[2]

Th-Ar calibration frames have been used to test the tilt correction algorithm. Unlike FP, Th-Ar does not provide equispaced lines of uniform intensity, which makes line detection across the order tricky. The method applies well on high to medium SNR arc lines. Fig. 6.14 shows binned corrected Th-Ar order overplotted on binned uncorrected order.

Fig. 6.15 shows the images of three uncorrected and corrected orders, plot-

---

[2]Data obtained from the ESO Science Archive Facility under request number 609319

Order 25:SSIM=0.980976

Order 34: SSIM=0.988868

Order 41: SSIM=0.977539
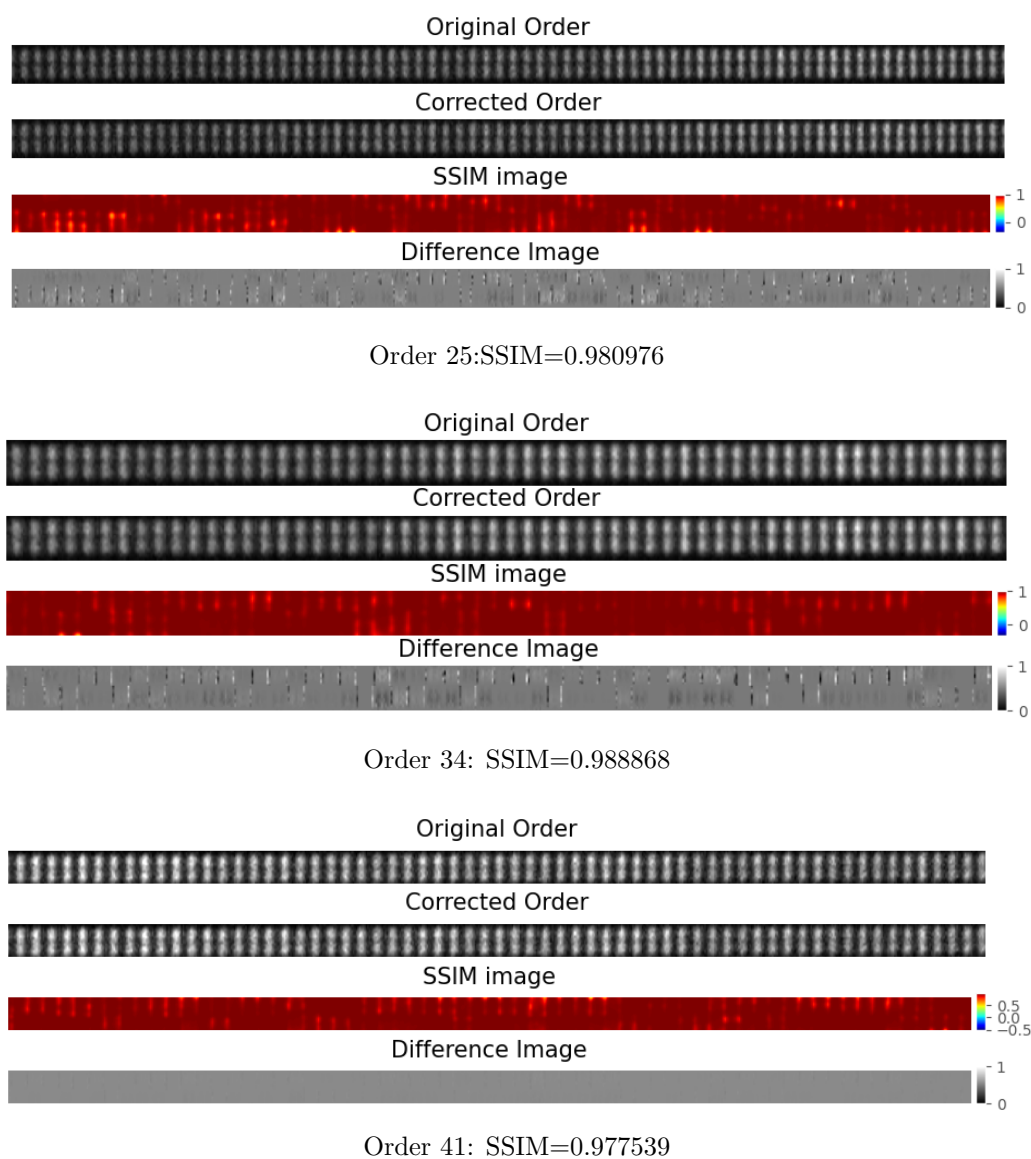
Figure 6.12: Zoomed in view of three tilt corrected FP spectral orders, taken with HESP. Original order is the image before tilt correction. Corrected order is the image after correction. SSIM image shows the similarity image, 1 being the parts where the images are similar. The similarity index is mentioned for each order. The difference image shows the normalized mathematical difference computed between two images, 0 being no difference regions.

ted along with their similarity image and difference image calculated between the original order and the corrected order.

X-shooter introduces visible tilts in the spectra, with the tilt amplitude being $\sim$ 1.5-2 times the HESP tilt values. Hence the calculated tilt values show less scatter than in HESP. Fig. 6.16 shows the comparison between the
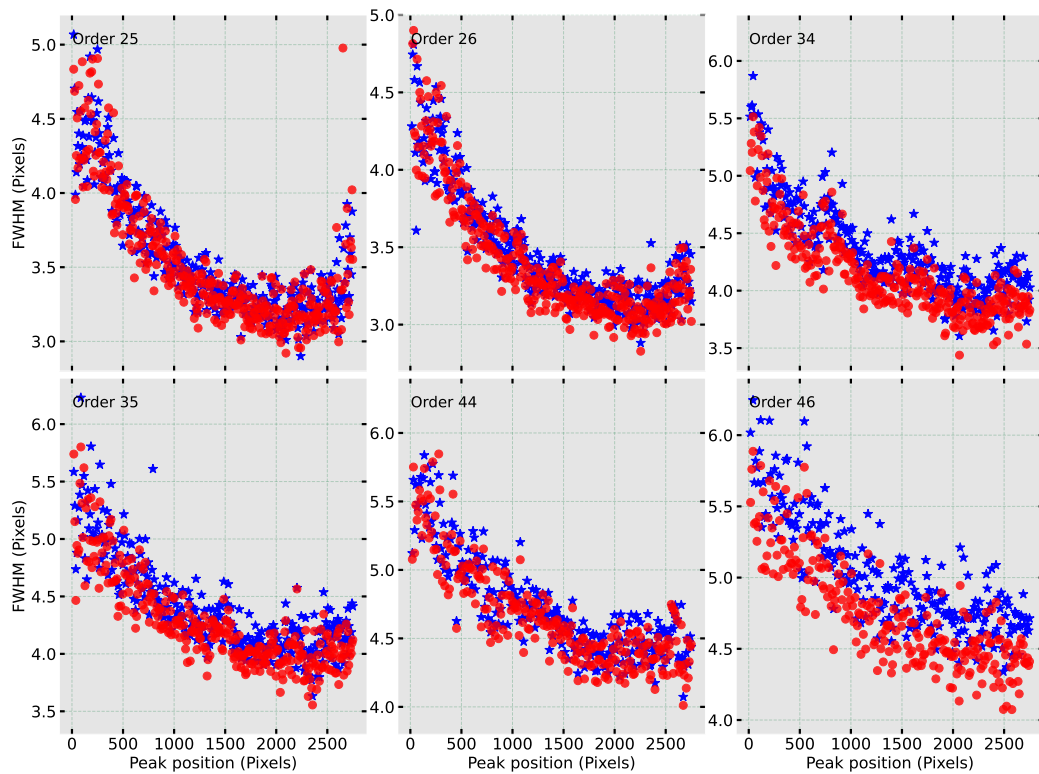
Figure 6.13: Comparison of FWHM of FP lines across an order before and after tilt correction. Values marked with blues stars show the FWHM of lines before correction. Values marked with red circles show the FWHM values of the same lines after correction.
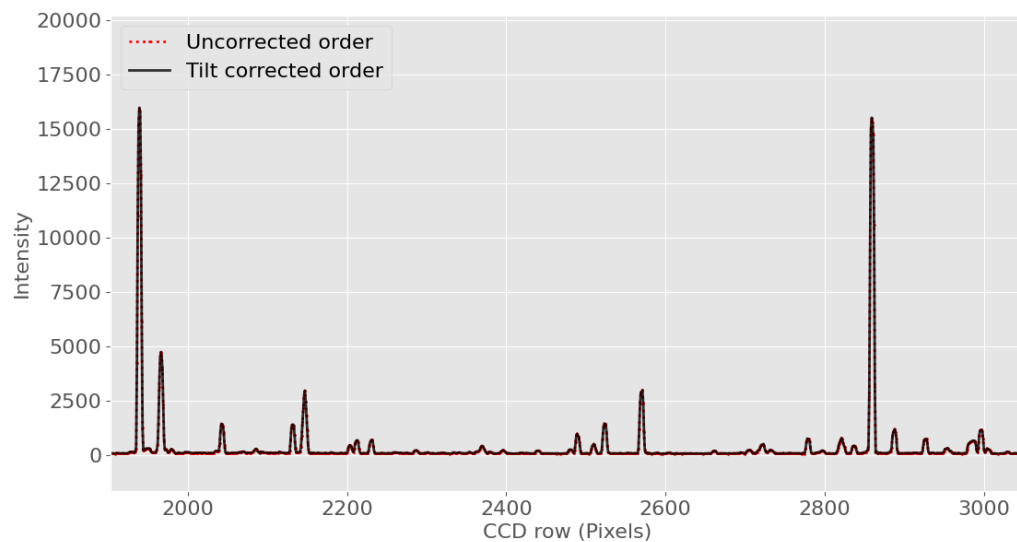
Figure 6.14: Zoomed in version showing few lines in the binned order before and after tilt correction. They have been overplotted to show that the code does not introduce any other artifacts into the data.

Table 6.1: Summarised result from tilt correction on HESP data.

Order no.	Original mean finesse	Corrected mean finesse	Total peaks	Peaks with increased FWHM	Peaks with decreased FWHM
25	2.161	2.175	360	75	285
26	2.250	2.300	355	45	310
27	2.224	2.224	349	182	167
28	2.255	2.288	343	44	299
29	2.209	2.233	337	60	277
30	2.231	2.259	332	68	264
31	2.217	2.235	326	87	239
32	2.165	2.211	321	10	311
33	2.172	2.179	315	95	220
34	2.053	2.151	309	2	307
35	2.057	2.115	304	14	290
36	2.052	2.071	297	53	244
37	1.982	2.089	290	0	290
38	2.035	2.122	287	1	286
39	2.081	2.076	282	164	118
40	2.123	2.140	276	55	221
41	2.124	2.168	270	8	262
42	2.166	2.184	265	67	198
43	2.236	2.314	260	2	258
44	2.291	2.326	254	11	243
45	2.336	2.332	249	164	85
46	2.257	2.387	243	0	243

slope values before and after correction. Most of the outliers in the data coincide with low SNR lines.

6.6 MIKE[3]

Since Th-Ar spectra do not share the same properties as FP spectra, only high to medium SNR lines are detected and corrected. We have performed the analysis on both blue and red channels of the spectrograph for data with slit settings of 2", 0.7" and 0.35". We will be presenting results of all the

---

[3]Data obtained from the LCO on request
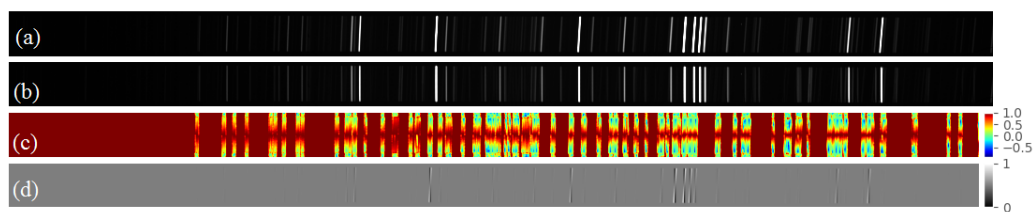
Order 9: SSIM=0.778193
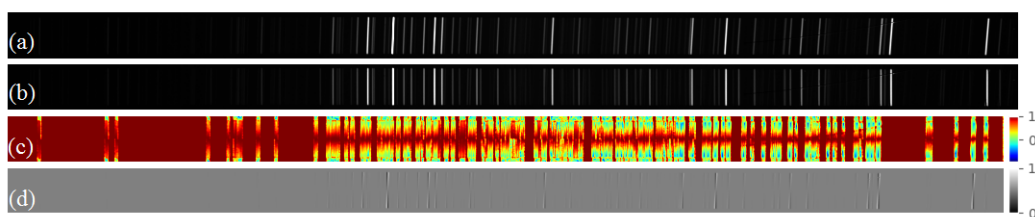
Order 10: SSIM=0.749655
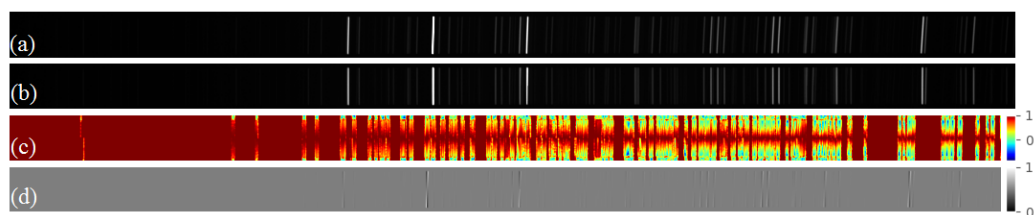
Order 12: SSIM=0.806626

Figure 6.15: Tilt correction of Th-Ar spectra taken with X-Shooter. (a) Original spectrum before the tilt correction. (b) Th-Ar spectrum after tilt correction. (c) SSIM image showing the similarity image. The regions with highest similarity in the images corresponds to 1. (d) Difference image shows the normalized mathematical difference computed between two images, 0 being no difference regions. The similarity index is mentioned for each order.

settings mentioned for the top, middle and bottom order.

Fig. 6.17 and Fig. 6.18 show the corrected and difference images for the 2" slit setting of the spectrograph in the blue and red channel respectively. The tilt in lines before and after correction is visible in the figure. Figure 6.19 shows the slope values before correction and after correction for spectra with 2" slit width in both blue and red channels.

Fig. 6.20 and Fig. 6.21 show the corrected and difference images for the 0.7" slit setting of the spectrograph in the blue and red channel respectively. Fig. 6.22 shows the corrected slope values for 0.7" slit data in both blue and red channels.
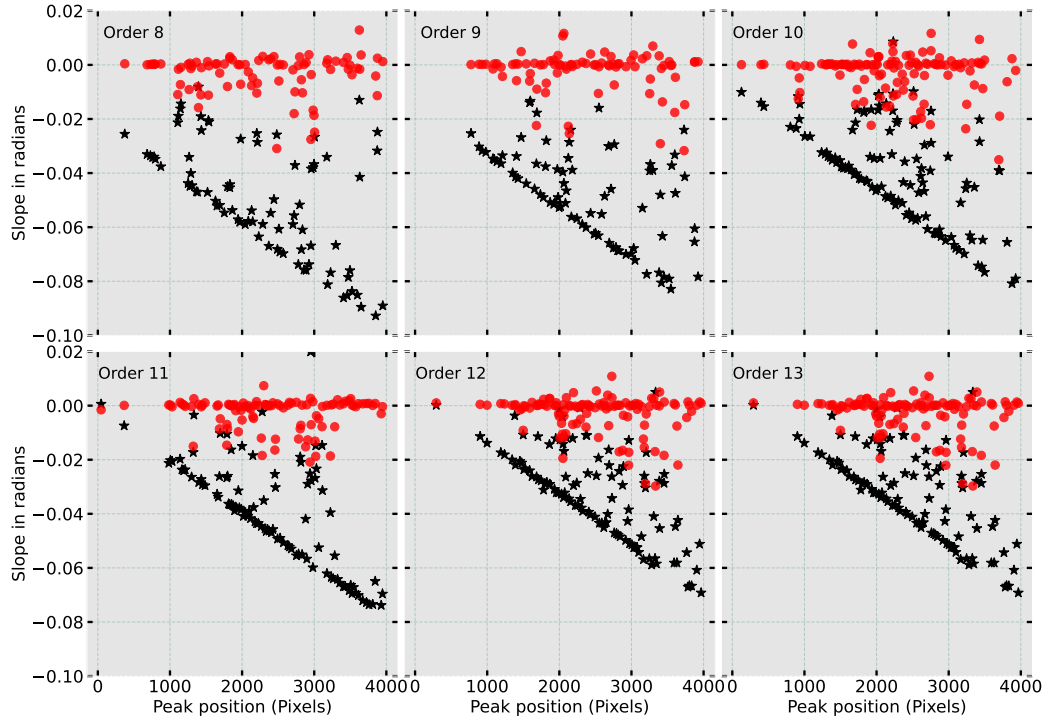
Figure 6.16: Slope values plotted for the uncorrected (black stars) Th-Ar lines and the corrected lines (red circles) for X-Shooter. The uncorrected slope values follow a clear trend. The scatter arises due to the attempt to calculate slopes of low SNR lines. The slope of the Th-Ar lines have been reduced after correction, the only deviation arising around the low SNR lines.

Fig. 6.23 and Fig. 6.24 show the corrected and difference images for the 0.35" slit setting of the spectrograph in the blue and red channel respectively. The corrected slope values for 0.35" slit setting is plotted in Fig. 6.25 for both blue and red channels.

We find a nearly similar performance while comparing the outcome of MIKE pipeline with our algorithm. Fig. 6.26 shows comparison between the FWHM of extracted Th-Ar lines by MIKE pipeline ($lw1$) and by the discussed algorithm ($lw2$). The difference between $lw1$ and $lw2$ has also been plotted, a positive difference obtained when $lw1$ is greater than $lw2$. The values have been calculated for one order of Th-Ar spectrum obtained in red channel using slit widths of 0.35", 0.7" and 2". For 0.35" slit width, MIKE pipeline gives $19\% \pm 7\%$ mean reduction in the FWHM of the Th-Ar lines whereas our algorithm gives $20\% \pm 7\%$ mean reduction in the FWHM. For 0.7" slit
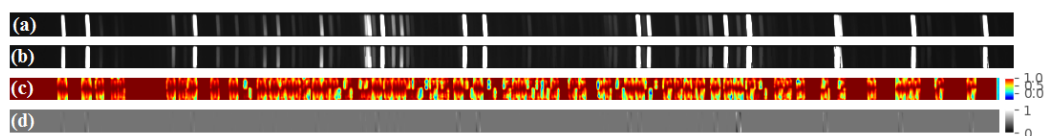
Blue order 12: SSIM=0.924884
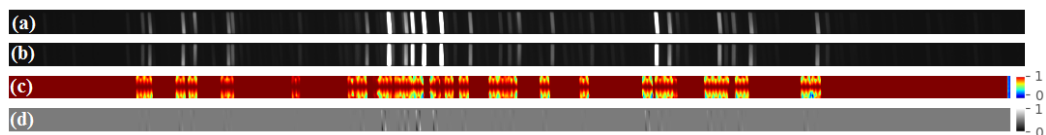
Blue order 18: SSIM=0.934234
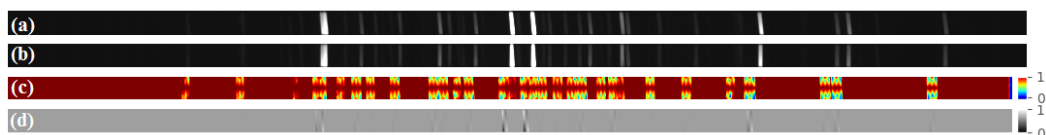
Blue order 28: SSIM=0.963201

Figure 6.17: Orders after tilt correction of Th-Ar lines for 2" slit setting of MIKE in the blue channel. (a) The image of order before tilt correction. (b) The image of same order after correction. (c) SSIM image shows the similarity image, 1 being the areas with maximum similarity. (d) Difference image shows the normalized mathematical difference computed between two images, 0 being no difference regions.
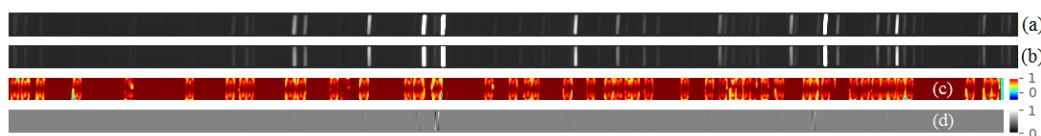
Red order 13: SSIM=0.964495
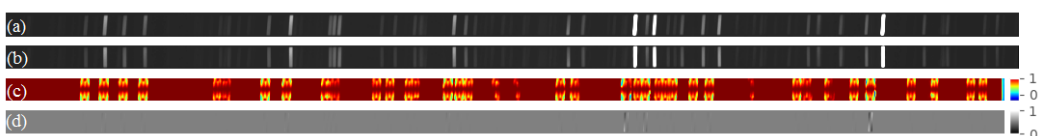
Red order 21: SSIM=0.933707
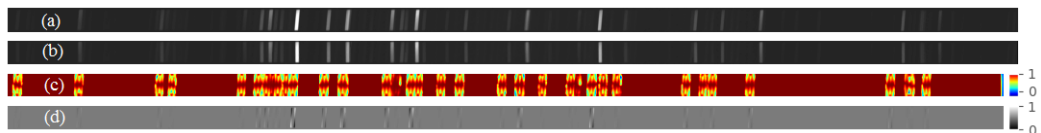
Red order 29: SSIM=0.959405

Figure 6.18: Orders after tilt correction of Th-Ar lines for 2" slit setting of MIKE in the red channel. (a) The image of order before tilt correction. (b) The image of same order after correction. (c) SSIM image shows the similarity image, 1 being the areas with maximum similarity. (d) Difference image shows the normalized mathematical difference computed between two images, 0 being no difference regions.
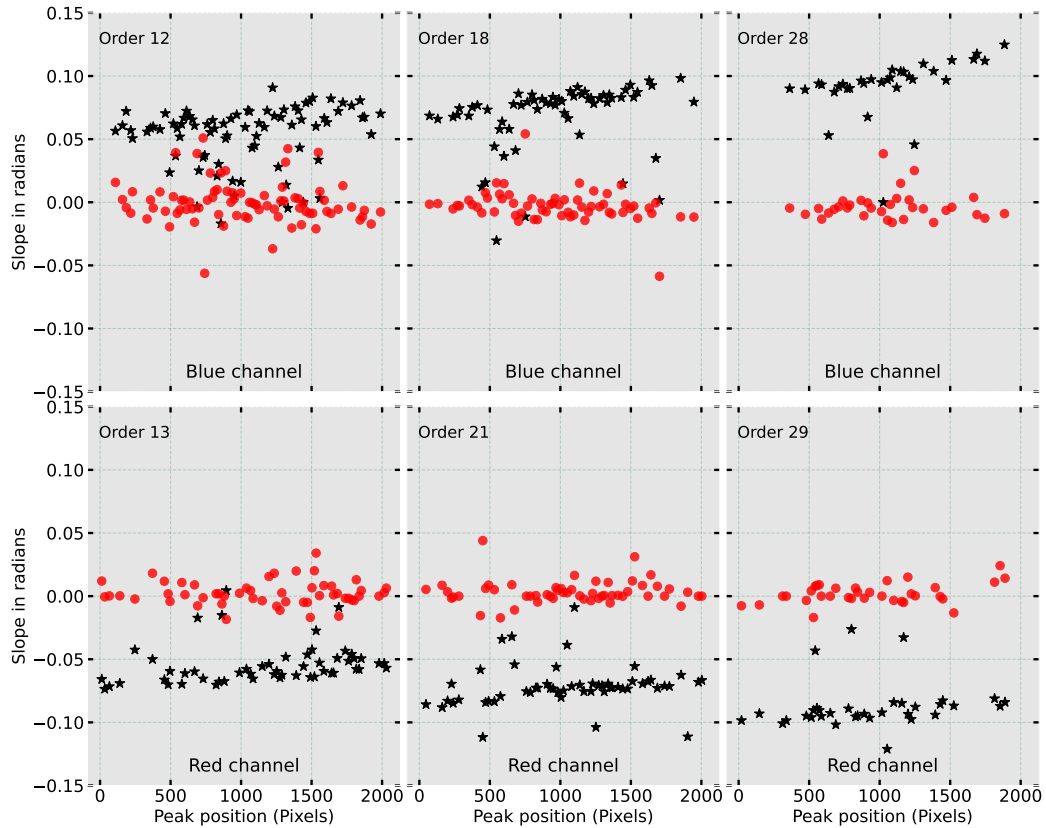
Figure 6.19: Slope values plotted for the uncorrected (black stars) Th-Ar lines and the corrected lines (red circles) for 2" slit setting of MIKE. The uncorrected slope values show a clear trend. The slope of the Th-Ar lines have been reduced after correction. The scatter in data is due to the attempt to calculate and correct for the low SNR lines.

width, MIKE pipeline gives $11\% \pm 4\%$ mean reduction in the FWHM of the Th-Ar lines whereas our algorithm gives $10\% \pm 4\%$ mean reduction in the FWHM. For 2" slit width, no significant change in line-width is observed for both the methods, even though the tilt can be seen reducing down close to zero in Fig 6.19. This can be due to the slit being wide as compared to the other two, causing decrease in spectral resolution.

6.7 Discussion

Analysis of the FP spectra acquired through HESP led us to the observation of discrepancies between the expected FP line FWHM (obtained with FTS) and the FWHM of the lines obtained with the spectrograph. This motivated us
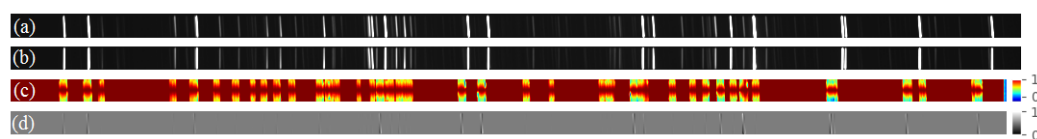
Blue order 12: SSIM=0.948363
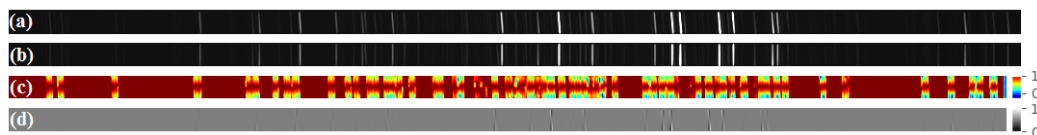
Blue order 19: SSIM=0.953734
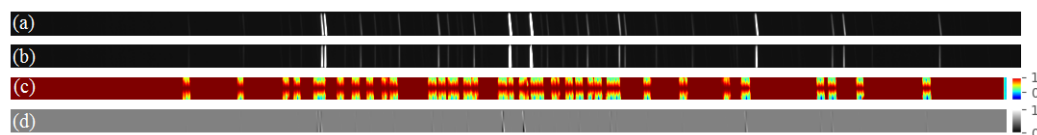
Blue order 28: SSIM=0.969412

Figure 6.20: Orders after tilt correction of Th-Ar lines for 0.7" slit setting of MIKE in the blue channel. (a) The image of order before tilt correction. (b) The image of same order after correction. (c) SSIM image shows the similarity image, 1 being the areas with maximum similarity. (d) Difference image shows the normalized mathematical difference computed between two images, 0 being no difference regions.
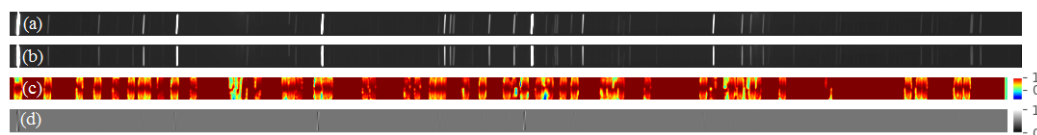
Red order 11: SSIM=0.949734
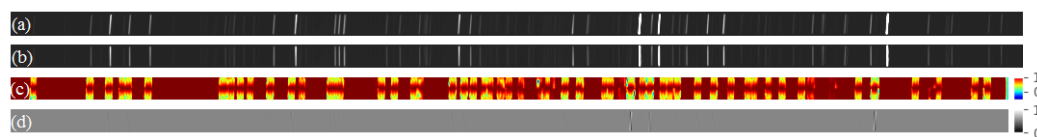
Red order 20: SSIM=0.946387
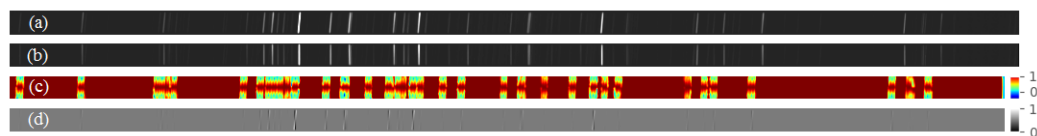
Red order 28: SSIM=0.959051

Figure 6.21: Orders after tilt correction of Th-Ar lines for 0.7" slit setting of MIKE in the red channel. (a) The image of order before tilt correction. (b) The image of same order after correction. (c) SSIM image shows the similarity image, 1 being the areas with maximum similarity. (d) Difference image shows the normalized mathematical difference computed between two images, 0 being no difference regions.
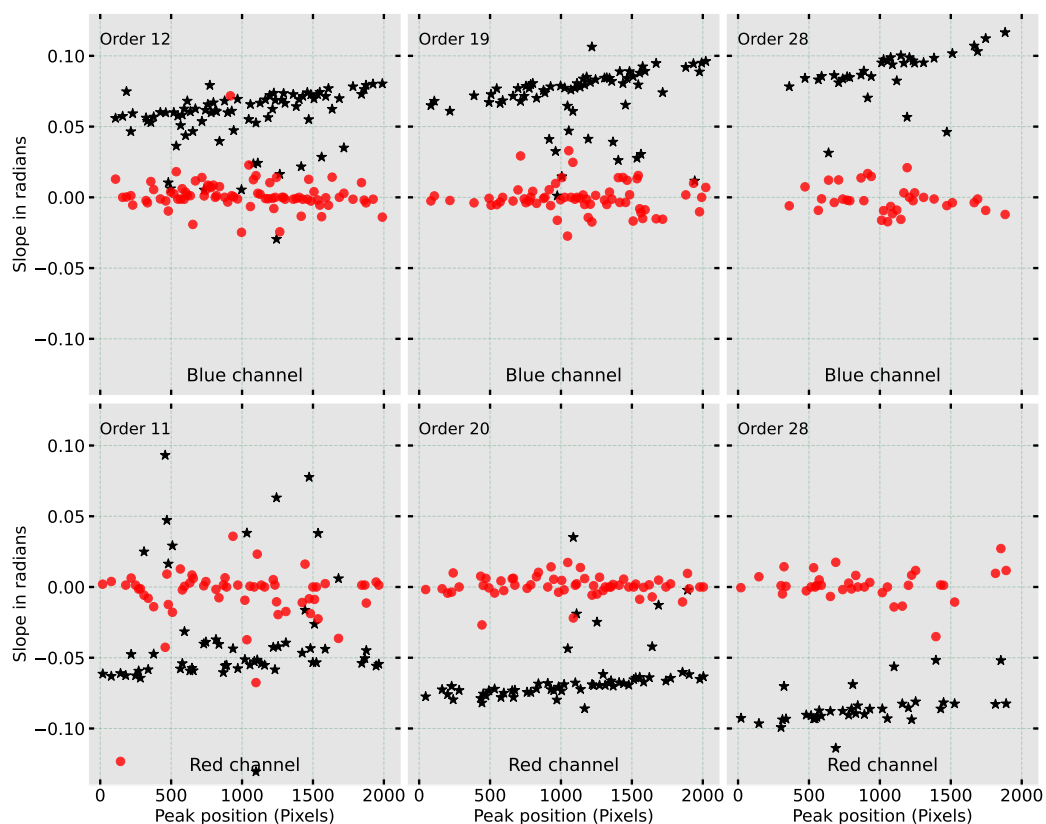
Figure 6.22: Slope values plotted for the uncorrected (black stars) Th-Ar lines and the corrected lines (red circles) for 0.7" slit setting of MIKE. The uncorrected slope values show a clear trend. The slope of the Th-Ar lines have been reduced after correction. The scatter in data is due to the attempt to calculate and correct for the low SNR lines.

to examine the factors that can cause the increase in line-width. Performance of the FP degrades over the years due to deterioration of the optical coating. An additional reason for the increase in line-width was found to be the tilt in the FP lines, caused due to curvature in the orders. The HESP design does not introduce any significant tilt in the data. Hence it is not visually discernible in the spectra. Although the amount of the tilt is small, it is important to take care of this artifact in post-processing in order to maintain the performance of FP.

Tilted lines in echelle spectra are artifacts often introduced by the curvature in spectra or due to the design of the spectrograph itself. It is essential to eliminate this artifact in order to avoid the introduction of any errors in the data while post-processing. A possible way is to avoid binning the data

Blue order 10:SSIM=0.953052

Blue order 19: SSIM=0.966096

Blue order 27: SSIM=0.9407741
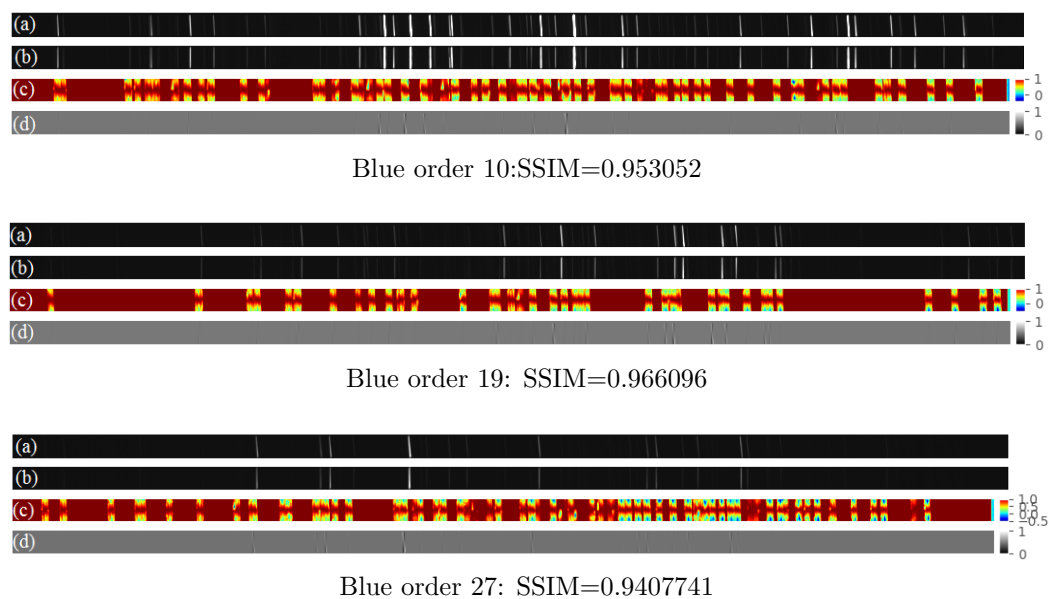
Figure 6.23: Orders after tilt correction of Th-Ar lines for 0.35" slit setting of MIKE in the blue channel. (a) The image of order before tilt correction. (b) The image of same order after correction. (c) SSIM image shows the similarity image, 1 being the areas with maximum similarity. (d) Difference image shows the normalized mathematical difference computed between two images, 0 being no difference regions.

Red order 13:SSIM=0.961899

Red order 21: SSIM=0.9441934

Red order 29: SSIM=0.955262
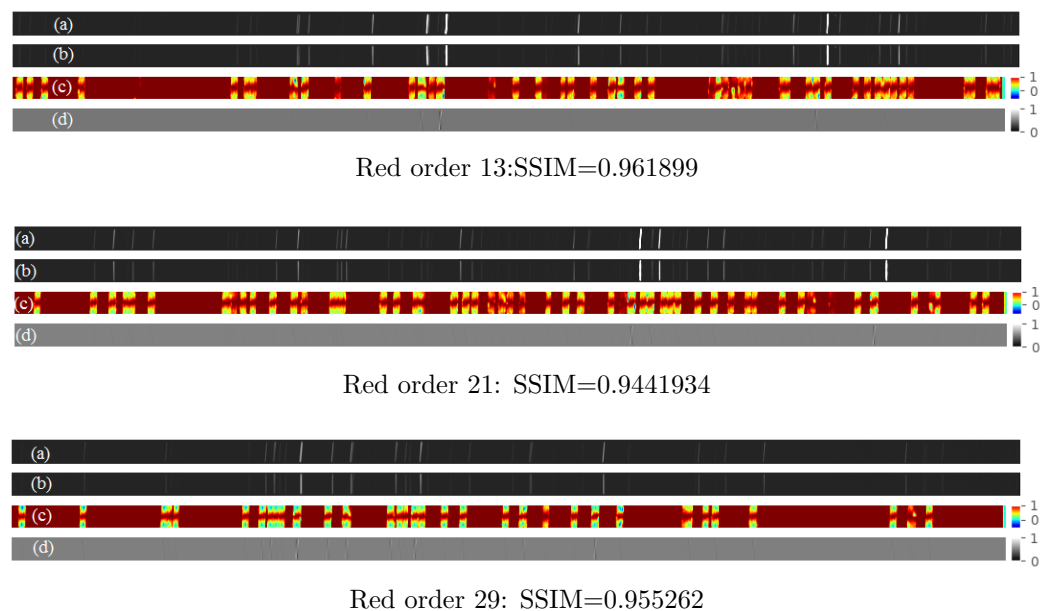
Figure 6.24: Orders after tilt correction of Th-Ar lines for 0.35" slit setting of MIKE in the red channel. (a) The image of order before tilt correction. (b) The image of same order after correction. (c) SSIM image shows the similarity image, 1 being the areas with maximum similarity. (d) Difference image shows the normalized mathematical difference computed between two images, 0 being no difference regions.
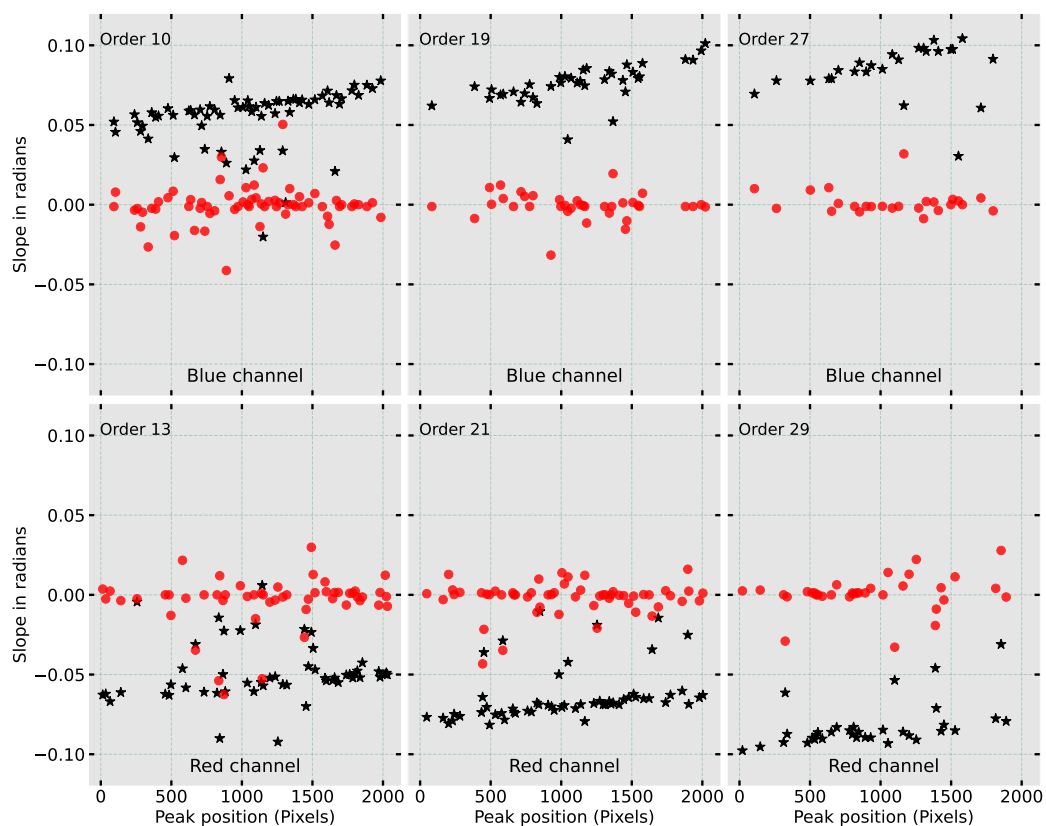
Figure 6.25: Slope values plotted for the uncorrected (black stars) Th-Ar lines and the corrected lines (red circles) for 0.35" slit setting of MIKE. The uncorrected slope values show a clear trend. The slope of the Th-Ar lines have been reduced after correction. The scatter in data is due to the attempt to calculate and correct for the low SNR lines.

and analyzing the flux at a single-pixel location. However, this technique will result in lesser flux values and hence less SNR in the data. Binning the 2D spectrum in the usual way is done vertically, i.e. along the slit direction. When a tilted line is binned vertically, it results in wrong flux values at each binned pixel as well as a decrease in spectral resolution due to the broadening of the line, and hence wrong wavelength when the final calibration is performed. The tilt is not constant and varies as a function of wavelength across the spectra. This also affects the accuracy with which we can determine the centroid positions of spectral lines, which is crucial in the case of high precision RV studies. To avert the miscalculations arising from binning a tilted line vertically, either the binning could be performed along an oblique axis or a simpler way is to find out the obliquity of each spectral line and correct
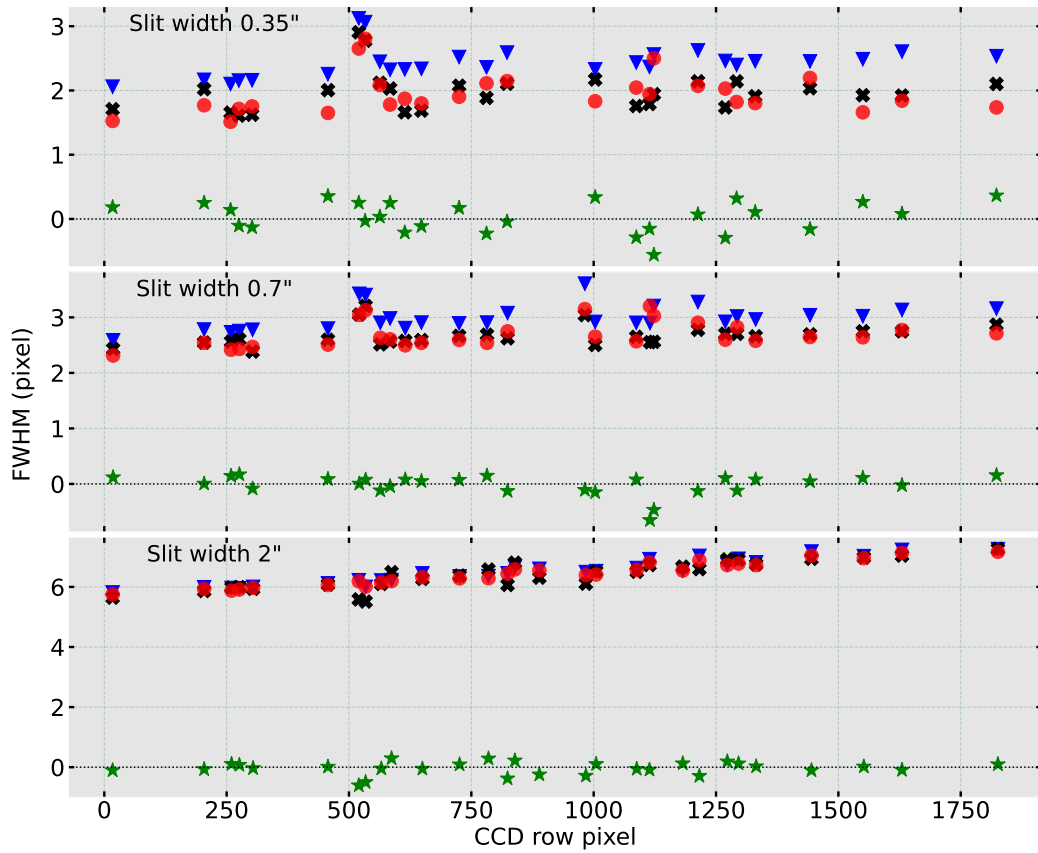
Figure 6.26: Performance of the developed algorithm with respect to MIKE pipeline. The blue triangles represent FWHM of uncorrected tilted lines. The black cross indicates FWHM of lines obtained after reduction with MIKE pipeline. The red circles indicate FWHM of lines obtained after reduction with discussed algorithm. Green stars indicate the difference between the line-widths obtained from MIKE pipeline and discussed algorithm.

for it. We employ the latter method to remove the tilt by automating the detection of each spectral line, computing the line's slant, and then compensating for it, so that the standard post-processing techniques can be applied as usual.

We have developed a simple algorithm for curvature and tilt correction in high-resolution spectra. The algorithm is written in Python and uses image processing techniques for finding individual line slant values and correcting for them. We have demonstrated the algorithm on FP calibration spectra from HESP. We have also performed the tilt corrections on the Th-Ar calibration spectra from X-shooter and MIKE using the method discussed. We noticed visual improvement in tilts of the lines after the application of the algorithm.

We also calculated the tilt values of each line before and after correction and found a reduction in the absolute value of the slope after correction, thereby indicating the efficacy of the algorithm. Currently, the main limitation of the algorithm is its inability to deal with very low SNR/faint lines (SNR¡6) and blended lines in Th-Ar spectra which results in small but noticeable increase in FWHM. This is partly due to the fact that algorithm was primarily developed keeping in mind the uniform line density provided by FP or LFC. This issue can be addressed either by filtering out or setting an appropriate threshold on the SNR for correction. We plan to incorporate this feature in the future upgrade.

Chapter 7

Summary and Future Work

7.1 Summary

Spectroscopy helps in investigating the physical and chemical properties of astrophysical sources. Some of these astrophysical phenomena require the need for higher precision to understand their inherent properties. The limitation of traditional wavelength calibration techniques is one of the major barriers in high precision spectroscopy. The thesis revolves around the domain of preparing an existing facility for high precision spectroscopy by the use of a Fabry-Pérot etalon as a source of wavelength calibration. FP based wavelength calibrator, when properly stabilized, can aid in overcoming the obstacles offered by the traditional techniques, at affordable costs.

The novel features of this thesis are:

- Entire instrument is designed and built in house, which includes the opto-mechanical design, construction of temperature stabilized enclosure, design of temperature controller and continuous fiber feedthrough for the vacuum enclosure.

- High precision radial velocity measurements require wavelength calibration specific to the spectrograph. Hence, the design of our instrument is

based on the requirements of HESP and differs significantly from other existing designs of FP based wavelength calibrators.

- This method helps in analyzing the design artifacts of the spectrograph. A generic algorithm has been developed to counter two such artifacts, namely curvature and tilt in high resolution spectra. This algorithm provides a much simpler approach towards correcting the said artifacts, is more robust and can be adapted to other calibration techniques like Th-Ar and LFC.

The main aim of this thesis was to develop a passively stabilized Fabry-Pérot etalon based instrument to be used as a wavelength calibration source in HESP to conduct radial velocity studies with the spectrograph with a precision of 10 m/s over one observation night. We have studied the various factors that affect the stability of the FP lines, and the design parameters like pressure, temperature, and opto-mechanical stability have been decided accordingly, as tabulated in Table 3.1. The design of the instrument has been discussed in detail in Chapter 4. Two different opto-mechanical setups, cage based and rail-based, were tested, and the setup offering more stability was chosen for the final design, i.e. rail-based scheme. The entire instrument had been assembled and tested in the laboratory to confirm that the pressure and temperature requirements are being met.

The FP has been tested with FTS to confirm the parameters offered by the manufacturer, and the results were used to calculate the absolute interference order. Analysis of the results obtained from the testing of FP setup with VBT echelle spectrograph was performed to fine tune the opto-mechanical design to meet the angular stability requirements. The complete setup has been installed on HESP, and preliminary tests were carried out to check the performance of FP with HESP. In Chapter 5, the results from all the tests have been shown. A difference in finesse values was observed, which can be caused due to the degradation of the optical coating of FP over a period of

5 years. It also has to be kept in mind that the computed finesse is just the ratio of the distance between FP peaks and the observed line-width. Hence, it is not an accurate depiction of the quoted FP finesse since the FP lines are convolved with the instrument profile of the spectrograph. If the line-width is dominated by the resolution of the spectrograph, the computed finesse will be lowered.

The results obtained from FP observations with HESP served as a motivation towards developing an algorithm for the removal of instrument design artifacts that can increase the line-width of the FP peaks. This algorithm provides a simple way of tilt correction in high resolution spectra that can be used for all general purpose spectrographs. The removal of such artifacts will also eventually lead to developing an accurate wavelength calibration model for the FP calibration setup. When applied to our FP data, the algorithm was able to reduce the line-width of 5417 lines out of a total of 6624 lines observed. The algorithm has been verified with data from spectrographs with known high tilts and curvature like X-Shooter and MIKE.

An essential aspect of this thesis is to prepare HESP for RV studies. With various sky transit survey satellite missions coming up, the requirement of ground-based RV follow-up observations become important to determine the mass and other orbital parameters of new exoplanets. Equipped with a technique for precise calibration and tracking instrumental shifts, HESP can conduct follow-up observations of some of the targets identified by the space missions.

7.2 Future Work

7.2.1 Upgrading the vacuum enclosure design

We are making the system more compact and replacing the cylindrical vacuum chamber with a rectangular, custom-designed chamber of size 50cm x 25 cm x

20 cm. The chamber has already been fabricated by Vacuum Techniques Ltd and is shown in Fig. 7.1. The chamber is designed with five ports available for electrical feedthrough, optical feedthrough, connecting to turbopump and vacuum gauge. The top part of the chamber comes with a detachable lid with handles to make the assembling of the FP and related optics inside the chamber easier. A rectangular viton O-ring is provided for proper placement and sealing of the lid while the chamber is in operation. The entire enclosure is mounted on a custom made table and fixed on four hinges, maintaining a clear distance between the tabletop and the bottom of the chamber. Polymide flexible heaters of appropriate size, according to the new chamber, will be used for heating.

Figure 7.1: The new rectangular vacuum chamber that will be used for future upgradation of the instrument.

Instead of using 100 μm fibers at the input side, 50 μm will be used, apart from which the opto-mechanical setup remains unchanged. For the input fiber, we will be using low OH content Optran® WF optical fiber. The fiber has a silica glass core of diameter 50 μm and NA=0.22. The wavelength range of operation is 300 nm - 2400 nm. The attenuation plot of the fiber is shown in Fig. 7.2.
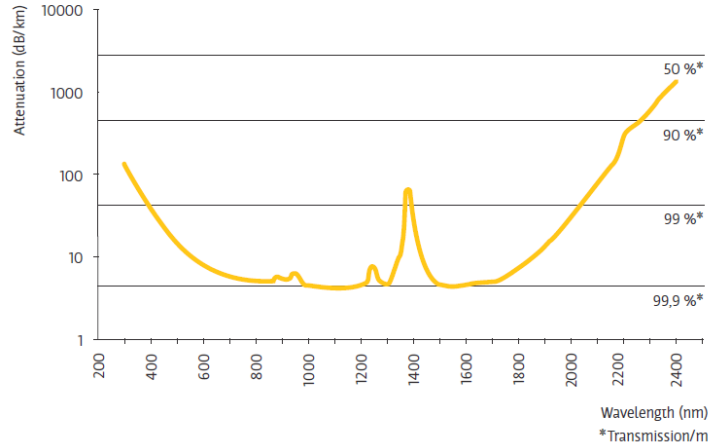
Figure 7.2: Attenuation values with respect to wavelength for Optran® WF optical fibers. Credits: CeramOptec®

7.2.2 Development of wavelength calibration model

The peak positions in an etalon are decided by the cavity length and interference order m. The actual position of the peaks in an FP is not known, hence, it requires an external source for absolute calibration. Tilt and curvature correction performed on the data removes any ambiguities in the measurement of these peak positions. A wavelength calibration model will be developed using the techniques employed in (Bauer *et al.*, 2015; Cersullo *et al.*, 2019).

The absolute interference order has been determined using the FP observations taken from FTS. The wavelength calibration models are specific to the individual spectrographs. Th-Ar calibration files of the spectrograph are being used to carry out the initial wavelength marking of the FP lines. HESP spectrograph is equipped with dual fibers for science and calibration frames, respectively. With few optical design changes of the HESP calibration unit, FP and Th-Ar frames can be taken simultaneously, hence leading to a more accurate prediction of FP based wavelength calibration model.

7.2.3   On sky observations

During a real observing run, several factors influence the stability of the spectrograph, which require a good understanding of the system's behaviour due to environmental changes and the operation of the observatory during the night. An appropriate calibration sequence needs to be worked out to mitigate these errors.

Observation of radial velocity standard stars, telluric lines and the laboratory calibration sources need to be carried out to study these effects. Scientific observations to validate the achievement of required RV precision have to be conducted at the telescope facilities. Since the main aim is to provide accurate calibration throughout the spectra for a wide range of wavelengths, the effect of stellar pulsations on the exoplanet radial velocity signal can be separated.

7.2.4   Active calibration

In this design, the FP etalon is being operated in transmission with only environmental control. This is termed as passive calibration. A passively stabilized etalon can suffer from frequency drifts due to various reasons, including aging of spacers in etalons (Wildi *et al.*, 2009), degradation of dielectric mirror coatings in the long term (Banyal & Reiners , 2017), changing environmental conditions as well as changing the illumination (Sturmer *et al.*, 2017).

Active stabilization of etalon involves tracking the change in position of etalon lines in real-time and then correcting for it by referencing them to an atomic transition which serves as an absolute scale. This can be done by locking one line of FP etalon to the laser frequency of a stabilized diode laser, which is in turn locked to a rubidium standard (Sturmer *et al.*, 2017; Reiners *et al.*, 2014). Any drift in the cavity length can be corrected by a piezoelectric transducer, which can modulate the cavity length. Long term stability of FP etalon is hence directly tied to the long term stability of Rubidium reference

lines. This leads to the achievement of more precise wavelength calibration and hence, more precise RV measurement. The concept of actively tracking the etalon to a rubidium reference is depicted in Fig. 7.3.
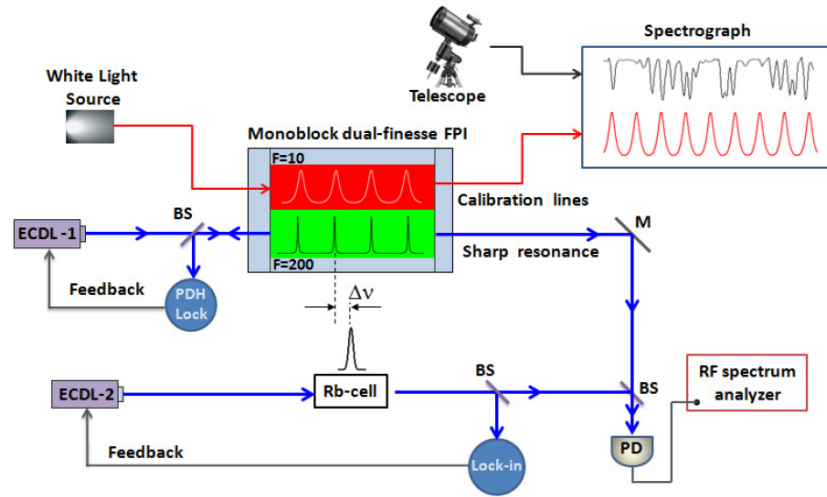
Figure 7.3: Schematic depicting the active tracking of the etalon cavity using laser locking. The red block is the FP that produces calibration lines for an echelle spectrograph. The green block signifies the high finesse etalon that acts as an external reference to lock diode laser's frequency (ECDL-1) to the calibration FP cavity. The high-speed photodetector PD records the RF-beat signal produced by interference between the Rb-locked ECDL-2 and the cavity-locked ECDL-1. Any observed change in the beat frequency translates to the drift in cavity spacing. Credits: Reiners *et al.* (2014)

Laboratory experiments are planned for actively measuring and controlling cavity length drifts. A high finesse etalon will be used for this purpose. An external cavity diode laser (ECDL) will scan rubidium reference lines and one full line of FP etalon. The error signal due to the drift of the etalon line against rubidium reference will be used for correction and hence actively stabilize the etalon.

Bibliography

Owens, J.C., *Optical Refractive Index of Air: Dependence on Pressure, Temperature and Composition*, **Applied Optics**, Vol. 6, 51–59 (1967).

Cersullo, F., Wildi, F., Chazelas, B., Pepe, F., *A new infrared Fabry-Pérot-based radial-velocity-reference module for the SPIRou radial-velocity spectrograph*, **A** & **A** 601 (2017).

Bauer, F. F., Zechmeister, M., Reiners, A., *Calibrating echelle spectrographs with Fabry-Pérot etalons*, **A** & **A** 581, A117 (2015).

Ma,Yuxuan, Meng,Fei, Liu,Yizhou, Zhao,Fei, Zhao,Gang, Wang,Aimin, Zhang,Zhigang, *Visible astro-comb filtered by a passively stabilized Fabry-Perot cavity*, **Review of Scientific Instruments** 90, 013102 (2019).

Li-Jin Chen, Guoqing Chang, Chih-Hao Li, Andrew J. Benedick, David F. Philips, Ronald L. Walsworth, Franz X. Kärtner, *Broadband dispersion-free optical cavities based on zero group delay dispersion mirror sets*, **Opt. Express** 18, 23204–23211 (2010).

Richard A. McCracken, Éric Depagne, Rudolf B. Kuhn, Nicolas Erasmus, Lisa A. Crause, Derryck T. Reid, *Wavelength calibration of a high resolution spectrograph with a partially stabilized 15-GHz astrocomb from 550 to 890 nm*, **Opt. Express** 25, 6450–6460 (2017).

François Wildi and Francesco Pepe and Bruno Chazelas and Gaspare Lo Curto and Ch. Lovis, *A Fabry-Perot calibrator of the HARPS radial velocity spectrograph: performance report,* **Proc. SPIE** 7735, 1853–1863 (2010).

Kirilov,K. M., Denkova,D., Tsutsumanova,G. G., Russev,S. C., *Note: Simple vacuum feedthrough for optical fiber with SubMiniature version A connectors at both ends,* **Review of Scientific Instruments** 85, 076107 (2014).

Michael F. A'Hearn, Francis J. Ahern, David M. Zipoy, *Polarization Fourier Spectrometer for Astronomy,* **Applied Optics**, Vol. 13, 1147–1157 (1974).

Becker, E. D., Farrar, T. C., *Fourier Transform Spectroscopy,* **Science** 178, 361–368 (1972).

V. Saptari, *Fourier-Transform Spectroscopy Instrumentation Engineering,* SPIE Press, Bellingham, WA (2003).

Sireesha Chamarthi, Ravinder K. Banyal, S. Sriram, *Estimation and correction of the instrumental perturbations of Vainu Bappu Telescope Echelle spectrograph using a model-based approach,* **Journal of Astronomical Telescopes, Instruments, and Systems** 5, 038003 (2019).

Sireesha Chamarthi, Ravinder K. Banyal, S. Sriram, *Estimation of asymmetries in point spread function for the echelle spectrograph operating at Vainu Bappu Telescope for high precision radial velocity studies,* **Proc. SPIE** 10702, Ground-based and Airborne Instrumentation for Astronomy VII, 261 (2018).

Sireesha Chamarthi, Ravinder K. Banyal, S. Sriram, *Toward precision radial velocity measurements using Echelle spectrograph at Vainu Bappu Telescope,* **Journal of Astronomical Telescopes, Instruments, and Systems** 5, 1–9 (2019).

Sireesha Chamarthi, Ravinder K. Banyal, S. Sriram, Gajendra Pandey, *Stability analysis of VBT Echelle spectrograph for precise radial velocity measurements*, **Journal of Optics** 47, 195–201 (2018).

N. Kameswara Rao, S. Sriram, K. Jayakumar, F. Gabriel, *High resolution stellar spectroscopy with VBT echelle spectrometer*, **Journal of Astrophysics and Astronomy** 26, 331–338 (2005).

S. Sriram,Amit Kumar, Arun Surya, T. Sivarani,Sunetra Giridhar, S. Kathiravan, M. N. Anand, Damien Jones, Deon Grobler, Robert Jakobsson, Anantha Chanumolu, Athira Unni, Angchuk Dorje, Tsewang Dorje, Tsewang Gyalson, *Hanle echelle spectrograph: design and performance*, **Proc. SPIE** 10702, 2007–2021 (2018).

Anantha Chanumolu, Damien Jones, T. Sivarani, *Modelling high resolution Echelle spectrographs for calibrations: Hanle Echelle spectrograph, a case study*, **Experimental Astronomy** 39, 423–443 (2015).

Doug Tody, *The IRAF Data Reduction and Analysis System*, **Proc. SPIE** 627, Instrumentation in astronomy VI, 733 (1986).

Doug Tody, *IRAF in the Nineties*, **A.S.P. Conference Series**, Vol. 52, 173 (1993).

Geoffrey W. Marcy, R. P. Butler, *Precision radial velocities with an iodine absorption cell*, **Pub. Astron. Soc. Pac.** 104, 270 (1992).

M. T. Murphy, Th. Udem, R. Holzwarth, A. Sizmann, L. Pasquini, c. Araujo-Hauck, H. Dekker, S. D'Odorico, M. Fischer, T.W. Hänsch, A. Manescau, *High-precision wavelength calibration of astronomical spectrographs with laser frequency combs*, **Mon. Not. Roy. Astron. Soc.** 380, 839–847 (2007).

L. B. Robinson, D. W. Latham, *Instrumentation for Ground-Based Optical Astronomy*, in **The Ninth Santa Cruz Summer Workshop in As-**

tronomy and Astrophysics, held at Lick Observatory, Santa Cruz, CA, USA, 13–24 July 1987, Springer (1988).

Michael J. Ireland, Marc White, Joao P. Bento, Tony Farrell, Kathleen Labrie, Lance Luvaul, Jon G. Nielsen, Chris Simpson, *Data reduction software for the Gemini high resolution optical spectrograph*, **Software and Cyber-infrastructure for Astronomy V** vol. 10707, SPIE, 864–873 (2018).

R. Bernstein, S. A. Shectman, S. M. Gunnels, S. Mochnacki, A. E. Athey, *MIKE: a double-echelle spectrograph for the Magellan Telescopes at Las Campanas Observatory*, **Proc. SPIE** 4841, Instrument Design and Performance for Optical/Infrared Ground-based Telescopes, 1694–1704 (2003).

S. D'Odorico, H. Dekker, R. Mazzoleni,J. Vernet, I. Guinouard, P. Groot, F. Hammer, P. K. Rasmussen, L. Kaper, R. Navarro, R. Pallavicini, C. Peroux, F. M. Zerbi, *X-shooter UV- to K-band intermediate-resolution high-efficiency spectrograph for the VLT: status report at the final design review*, **Proc. SPIE** 6269, Ground-based and Airborne Instrumentation for Astronomy, 993–1002 (2006)

N. R. Napolitano, A. J. Romanowsky, C. Tortora, *The central dark matter content of early-type galaxies: scaling relations and connections with star formation histories*, **Mon. Not. Roy. Astron. Soc.** 405, 2351–2371 (2010).

Daniel D. Kelson, Garth D. Illingworth, Pieter G. van Dokkum, Marijn Franx, *The Evolution of Early-Type Galaxies in Distant Clusters III M/L_v ratios in the z=0.33 Cluster Cl 1358+62*, **The Astrophysical Journal** 531, 184–199 (2000).

A. Bik, Th. Henning, A. Stolte, W. Brandner, D. A. Gouliermis, M. Gennaro, A. Pasquali, B. Rochau, H. Beuther, N. Ageorges, W. Seifert, Y. Wang, N. Kudryavtseva, *Age spread in W3 main: Large binocular telescope/LUCI*

Near-Infrared spectroscopy of the masive stellar content, **The Astrophysical Journal** 744, 87 (2011).

Anirban Bhowmick, Gajendra Pandey, David L. Lambert, *Detection of Fluorine in Hot Extreme Helium Stars*, **The Astrophysical Journal** 891, 40 (2020).

A. P. Hatzes, *The Radial Velocity Method for the Detection of Exoplanets*, in **Methods of Detecting Exoplanets: 1st Advanced School on Exoplanetary Science** vol. 428 of Astrophysics and Space Science Library, Page 3 (2016).

S. Van der Walt, J. L. Schönberger, J. Nunez-Iglesias, F. Boulogne, J. D. Warner, N. Yager, E. Gouillart, T. Yu, *Scikit-image: image processing in Python*, **PeerJ** 2, e453 (2014).

G. Bradski, *The OpenCV Library*, **Dr. Dobb's Journal of Software Tools**, 2236121 (2000)

Rafael Brahm, Andrés Jordán, Néstor Espinoza, *CERES: A Set of Automated Routines for Echelle Spectra*, **Pub. Astron. Soc. Pac.** 129, 1–18 (2017).

Tianhe Zhou, Ming-Jun Lai, *Scattered data interpolation by bivariate splines with higher approximation order*, **Journal of Computational and Applied Mathematics** 242, 125–140 (2013).

Martin Dubs, Peter Schlatter, *A practical method for the analysis of meteor spectra*, **WGN, Journal of the International Meteor Organization** 43, 94–101 (2015).

Martin Dubs, K. Maeda, *Calibration of meteor spectra*, in **International Meteor Conference Egmond**, the Netherlands, 2-5 June 2016, Page 65 (2016).

John Canny, *A Computational Approach to Edge Detection*, **IEEE Transactions on Pattern Analysis and Machine Intelligence** 8, 679–698 (1986).

Zhou Wang, A. C. Bovik, H. R. Sheikh, E. P. Simoncelli, *Image quality assessment: from error visibility to structural similarity*, **IEEE Transactions on Image Processing** 13, 600–612 (2004).

J. Vernet, H. Dekker, S. D´Odorico, L. Kaper, P. Kjaergaard, F. Hammer, S. Randich, F. Zerbi, P. J. Groot, J. Hjorth, I. Guinouard, R. Navarro, T. Adolfse, P. W. Albers, J. P. Amans, J. J. Andersen, M. I. Andersen, P. Binetruy, P. Bristow, R. Castillo, F. Chemla, L. Christensen, P. Conconi, R. Conzelmann, J. Dam, V. De Caprio, A. De Ugarte Postigo, B. Delabre, P. Di Marcantonio, M. Downing, E. Elswijk, G. Finger, G. Fischer, H. Flores, P. François, P. Goldoni, L. Guglielmi, R. Haigron, H. Hanenburg, I. Hendriks, M. Horrobin, D. Horville, N. C. Jessen, F. Kerber, L. Kern, M. Kiekebusch, P.Kleszcz, J. Klougart, J. Kragt, H. H. Larsen, J. L. Lizon, C. Lucuix, V. Mainieri, R. Manuputy, C. Martayan, E. Mason, R. Mazzoleni, N. Michaelsen, A. Modigliani, S. Moehler, P. Møller, A. Norup Sørensen, P. Nørregaard, C. Péroux, F. Patat, E. Pena, J. Pragt, C. Reinero, F. Rigal, M. Riva, R. Roelfsema, F. Royer, G. Sacco, P. Santin, T. Schoenmaker, P. Spano, E. Sweers, R. Ter Horst, M. Tintori, N. Tromp, P. Van Dael, H. van der Vliet, L. Venema, M. Vidali, J. Vinther, P. Vola, R. Winters, D. Wistisen, G. Wulterkens, A. Zacchei, *X-shooter, the new wide band intermediate resolution spectrograph at the ESO Very Large Telescope*, **A & A** 536, A105 (2011).

P. Goldoni, F. Royer, P. François, M. Horrobin, G. Blanc, J. Vernet, A. Modigliani, J. Larsen, *Data reduction software of the X-shooter spectrograph*, **Proc. SPIE** 6269, Ground-based and Airborne Instrumentation for Astronomy, 822–832 (2006).

P. Goldoni, F. Royer, M. Horrobin, P. François, L. Guglielmi, R. Haigron, J. Vernet, A. Modigliani, P. Bristow, *Results of X-shooter data reduction software on laboratory frames*, **Proc. SPIE** 7014, Ground-based and Airborne Instrumentation for Astronomy, 2004–2014 (2008).

Rebecca M. Bernstein, Scott M. Burles, J. Xavier Prochaska, *Data Reduction with the MIKE Spectrometer*, **Pub. Astron. Soc. Pac.** 127, 911–930 (2015).

M. Mayor, D. Queloz, *A Jupiter mass companion to a solar-type star*, **Nature** 378, 355—359 (1995).

T. Appourchaux, K. Belkacem, A. M. Broomhall, W. J. Chaplin, D. O. Gough, G. Houdek, J. Provost, F. Baudin, P. Boumier, Y. Elsworth, R. A. García, B. N. Andersen, W. Finsterle, C. Fröhlich, A. Gabriel, G. Grec, A. Jiménez, A. Kosovichev, T. Sekii, T. Toutain, S. Turck-Chièze, *The quest for the solar g modes*, **Astronomy and Astrophysics Review** 18, 197–277 (2010).

J. Liske, A. Grazian, E. Vanzella, M. Dessauges, M. Viel, L. Pasquini, M. Haehnelt, S. Cristiani, F. Pepe, G. Avila, P. Bonifacio, F. Bouchy, H. Dekker, B. Delabre, S. D'Odorico, V. D'Odorico, S. Levshakov, C. Lovis, M. Mayor, P. Molaro, L. Moscardini, M. T. Murphy, D. Queloz,P. Shaver, S. Udry, T. Wiklind, S. Zucker, *Cosmic dynamics in the era of Extremely Large Telescopes*, **Mon. Not. Roy. Astron. Soc.** 386, 1192–1218 (2008).

E. Reinhold, R. Buning, U. Hollenstein, A. Ivanchik, P. Petitjean, W. Ubachs, *Indication of a Cosmological Variation of the Proton-Electron Mass Ratio Based on Laboratory Measurement and Reanalysis of H^2 Spectra*, **Phys. Rev. Lett.** 96, 151101 (2006).

M. Bazot, F. Bouchy, H. Kjeldsen, S. Charpinet, M. Laymand, S. Vauclair, *Asteroseismology of α Centauri A* - Evidence of rotational splitting*, **A & A** 470, 295-302 (2007).

R. P. Butler, T. R. Bedding, H. Kjeldsen, C. McCarthy, S. J. O'Toole, C. G. Tinney, G. W. Marcy, J. T. Wright, *Ultra-High-Precision Velocity Measurements of Oscillations in α Centauri A*, **The Astrophysical Journal** 600, L75–L78 (2003).

J. A. Dittmann, J. M. Irwin, D. Charbonneau, X. Bonfils, N. Astudillo-Defru, R. D. Haywood, Z. Berta-Thompson, E. R. Newton, J. E. Rodriguez, J. G. Winters, T. Tan, J. Almenara, F. Bouchy, X. Delfosse, T. Forveille, C. Lovis, F. Murgas, F. Pepe, N. Santos, S. Udry, A. Wnsche, G. Esquerdo, D. W. Latham, C. D. Dressing, *A temperate rocky super-Earth transiting a nearby cool star*, **Nature** 544, 333 (2017).

C. Lovis, F. Pepe, *A new list of thorium and argon spectral lines in the visible*, **A** & **A** 468, 1115–1121 (2007).

Samuel Halverson, Ryan Terrien, Suvrath Mahadevan, Arpita Roy, Chad Bender, Gudmundur Kári Stefánsson, Andrew Monson, Eric Levi, Fred Hearty, Cullen Blake, Michael McElwain, Christian Schwab, Lawrence Ramsey, Jason Wright, Sharon Wang, Qian Gong, Paul Roberston, *A comprehensive radial velocity error budget for next generation Doppler spectrometers*, **Proc. SPIE** 9908, 2022–2041 (2016).

Christophe Lovis, Francesco Pepe, François Bouchy, Gaspare Lo Curto, Michel Mayor, Luca Pasquini, Didier Queloz, Gero Rupprecht, Stéphane Udry, Shay Zucker, *The exoplanet hunter HARPS: unequalled accuracy and perspectives toward 1 cm/s precision*, **Proc. SPIE** 6269, Ground-based and Airborne Instrumentation for Astronomy, 62690P (2006).

Butler R. P., Marcy G. W., Williams E., McCarthy C., Dosanjh P., Vogt S. S., *Butler R. P., Marcy G. W., Williams E., McCarthy C., Dosanjh P., Vogt S. S.*, **Pub. Astron. Soc. Pac.** 108, 500 (1996).

T.Wilken, C. Lovis, A. Manescau, T. Steinmetz, L. Pasquini, G. LO Curto,

T. W. Hansch, R. Holzwarth, Th. Udem, *High precision calibration of spectrographs*, **Mon. Not. Roy. Astron. Soc.** 405, L16–L20 (2010).

C. Sireesha, *High Precision Radial Velocity studies of VBT Echelle Spectrograph*, Ph.D. Thesis, University of Calcutta (2019).

Max Born, Emil Wolf, *Chapter VII - Elements of the theory of Interference and Interferometers*, **Principles of Optics (Sixth Edition)**, Pergamon, 256–369 (1980).

Eugene Hecht, A. R. Ganesan, *Chapter 9 - Interference*, **Optics (Fourth Edition)**, McGraw-Hill, 366–419 (1975).

Harikrishn Varu, *The optical modelling and design of Fabry Perot Interferometer sensors for ultrasound detection*, Ph.D. Thesis, University College London (2014).

T. Gangopadhyay, *Prospects for Fibre Bragg Gratings and Fabry-Perot Interferometers in fibre-optic vibration sensing*, **Sensors Actuators A Phys.** 113, 20—38 (2004).

J. Yin, T. Liu, J. Jiang, K. Liu, S. Wang, F. Wu, Z. Ding, *Wavelength-division-multiplexing method of polarized low-coherence interferometry for fiber Fabry–Perot interferometric sensors*, **Opt. Lett.** 38, 3751—3753 (2013).

S. Liu, Y. Wang, C. Liao, G. Wang, Z. Li, Q. Wang, J. Zhou, K. Yang, X. Zhong, J. Zhao, J. Tang, *High-sensitivity strain sensor based on in-fiber improved Fabry-Perot interferometer*, **Opt. Lett.** 39, 2121—2124 (2014).

D. Su, X. Qiao, Q. Rong, H. Sun, J. Zhang, Z. Bai, Y. Du, D. Feng, Y. Wang, M. Hu, Z. Feng, *A fiber Fabry–Perot interferometer based on a PVA coating for humidity measurement*, **Opt. Commun.** 311, 107—110 (2013).

H. Y. Choi, K. S. Park, S. J. Park, U.-C. Paek, B. H. Lee, E. S. Choi, *Miniature fiber-optic high temperature sensor based on a hybrid structured Fabry-Perot interferometer*, **Opt. Lett.** 33, 2455-–2457 (2008).

T. Wei, Y. Han, Y. Li, H.-L. Tsai, H. Xiao, *Temperature-insensitive miniaturized fiber inline Fabry-Perot interferometer for highly sensitive refractive index measurement*, **Opt. Express** 16, 5764 (2008).

T. Zhang, Z. Gong, R. Giorno, L. Que, *A nanostructured Fabry-Perot interferometer*, **Opt. Express** 18, 20282–8 (2010).

D. G. Peterson, A. Yariv, *Interferometry and laser control with solid Fabry-Perot etalons*, **Applied Optics** 5, 985—991 (1966).

N. N. Elkin, A. P. Napartovich, *Numerical study of the stability of single-mode lasing in a Fabry–Perot resonator with an active medium*, **Appl. Math. Model.** 18, 513-–521 (1994).

H.J. Pan, P. Ruan, H.W. Wang, F. Li, *Confocal Fabry-Perot interferometer for frequency stabilization of laser*, **Laser Phys.** 21, 336—339 (2011).

S. K. Dhara, B. Ravindra, R. K. Banyal, *Fabry-Pérot based narrow band imager for solar filament observations*, **Research in Astronomy and Astrophysics** 16, 010 (2016).

Alfred Pérot, Charles Fabry, *On the Application of Interference Phenomena to the Solution of Various Problems of Spectroscopy and Metrology*, **The Astrophysical Journal** 9, 87 (1899).

A. Quirrenbach , P. J. Amado , H. M,el , J. A. Caballero , R. Mundt , I. Ribas , A. Reiners , M. Abril , J. Aceituno , C. Afonso , D. Barrado y Navascues , J. L. Bean , V. J. S. Béjar , S. Becerril , A. Böhm , M. C. Cárdenas , A. Claret , J. Colomé , L. P. Costillo , S. Dreizler , M. Fernández , X. Francisco , D. Galadí , R. Garrido , J. I. González Hernández , J. Guàrdia , E. W.

Guenther , F. Gutiérrez-Soto , V. Joergens , A. P. Hatzes , J. Helmling , T. Henning , E. Herrero , M. Kürster , W. Laun , R. Lenzen , U. Mall , E. L. Martin , S. Martín-Ruiz , E. Mirabet , D. Montes , J. C. Morales , R. Morales Muñoz , A. Moya , V. Naranjo , O. Rabaza , A. Ramón , R. Rebolo , S. Reffert , F. Rodler , E. Rodríguez , A. Rodríguez Trinidad , R. R. Rohloff , M. A. Sánchez Carrasco , C. Schmidt , W. Seifert , J. Setiawan , E. Solano , O. Stahl , C. Storz , J. C. Suárez , U. Thiele , K. Wagner , G. Wiedemann , M. R. Zapatero Osorio , C. del Burgo , E. Sánchez-Blanco , W. Xu, *CARMENES: Calar Alto high-resolution search for M dwarfs with exo-earths with a near-infrared Echelle spectrograph*, **Proc. SPIE** 7735, Ground-based and Airborne Instrumentation for Astronomy, 455–468 (2010).

Sebastian Schäfer, Ansgar Reiners, *Two Fabry-Perot interferometers for high precision wavelength calibration in the near-infrared*, **Proc. SPIE** 8446, Ground-based and Airborne Instrumentation for Astronomy, 1306–1313 (2012).

Gábor Fűrész, Alex Glenday, Christian Latham, *An economic Fabry-Perot wavelength reference*, **Proc. SPIE** 9151, Advances in Optical and Mechanical Technologies for Telescopes and Instrumentation, 1755–1762 (2014).

F. Cersullo, A. Coffinet, B. Chazelas, C. Lovis, F. Pepe, *New wavelength calibration for echelle spectrographs using Fabry-Pérot etalons*, **A** & **A** 624, A122 (2019).

F. Wildi, B. Chazelas, F. Pepe, *A passive cost-effective solution for the high accuracy wavelength calibration of radial velocity spectrographs*, **Proc. SPIE** 8446, Ground-based and Airborne Instrumentation for Astronomy, 1122–1129 (2012).

Francois Wildi, Francesco Pepe, Christophe Lovis, Bruno Chazelas, Tobias Wilken, Antonio Manescau, Luca Pasquini, Ronald Holzwarth, Tilo

Stenimetz, Thomas Udem, Theodor Hänsch, Gaspare Lo Curto, *Calibration of high accuracy radial velocity spectrographs: beyond the Th-Ar lamps*, **Proc. SPIE** 7440, Techniques and Instrumentation for Detection of Exoplanets, 197–205 (2009).

Francesco Pepe, Michel Mayor, Bernard Delabre, Dominique Kohler, Daniel Lacroix, Didier Queloz, Stephane Udry, Willy Benz, Jean-Loup Bertaux, Jean-Pierre Sivan, *HARPS: a new high-resolution spectrograph for the search of extrasolar planets*, **Proc. SPIE** 4008, Optical and IR Telescope Instrumentation and Detectors, 582–592 (2000).

Francois Wildi, Francesco Pepe, Bruno Chazelas, Gaspare Lo Curto, Christophe Lovis, *The performance of the new Fabry-Perot calibration system of the radial velocity spectrograph HARPS*, **Proc. SPIE** 8151, Techniques and Instrumentation for Detection of Exoplanets, 535–543 (2011).

J. Donati, D. Kouach, M. Lacombe, S. Baratchart, R. Doyon, X. Delfosse, E. Artigau, C. Moutou, G. Hébrard, F. Bouchy, J. Bouvier, S. Alencar, L. Saddlemyer, L. Parès, P. Rabou, Y. Micheau, F. Dolon, G. Barrick, O. Hernandez, S. Y. Wang, V. Reshetov, N. Striebig, Z. Challita, A. Carmona, S. Tibault, E. Martioli, P. Figueira, I. Boisse, F. Pepe, *SPIRou: A NIR Spectropolarimeter/High-Precision Velocimeter for the CFHT*, **Handbook of Exoplanets**, 107 (2018).

Sebastian Schäfer, *Fabry-Pérot etalons for high precision radial velocity calibration*, Ph.D. Thesis, University of Göttingen (2014).

Julian Sturmer, Andreas Seifahrt, Christian Schwab, Jacob L. Bean, *A Rubidium-traced white-light etalon calibrator for radial velocity measurements at the cm/s level*, **Journal of Astronomical Telescopes, Instruments, and Systems** 2, 1–10 (2017)

A. Reiners, R. K. Banyal, R. G. Ulbrich, *A laser-lock concept to reach cm/s*

precision in Doppler experiments with Fabry-Pérot wavelength calibrators, **A** & **A** 569, A77 (2014).

A. Reiners, R. K. Banyal, *A Dual Cavity Fabry–Perot Device for High Precision Doppler Measurements in Astronomy*, **Journal of Astronomical Instrumentation** 6, 1750001 (2017).

B.P. Abbott et. al. *Observation of Gravitational Waves from a Binary Black Hole Merger*, LIGO Scientific Collaboration and Virgo Collaboration, **Phys. Rev. Lett.** 116, 061102 (2016).

John J. Bochanski, Joseph F. Hennawi, Robert A. Simcoe, J. Xavier Prochaska, Andrew A. West, Adam J. Burgasser, Scott M. Burles, Rebecca A. Bernstein, Christopher L. Williams, Michael T. Murphy, *MASE: A New Data-Reduction Pipeline for the Magellan Echellette Spectrograph*, **Pub. Astron. Soc. Pac.** 121, 1409 (2009).

Andrea Modigliani, Paolo Goldoni, Frédéric Royer, Regis Haigron, Laurent Guglielmi, Patrick François, Matthew Horrobin, Paul Bristow, Joel Vernet, Sabine Moehler, Florian Kerber, Pascal Ballester, Elena Mason, Lise Christensen, *The X-shooter pipeline*, **Proc. SPIE** 7737, Observatory Operations: Strategies, Processes, and Systems III, 773728 (2010).

Nikolai Piskunov, Ansgar Wehrhahn, Thomas Marquart, *Optimal extraction of echelle spectra: Getting the most out of observations*, **A** & **A** 646, A32 (2021).

N. E. Piskunov, J. A. Valenti. *New algorithms for reducing cross-dispersed echelle spectra*, **A** & **A** 385, 1095-1106 (2002).

Rosario Cosentino et. al. *Harps-N: the new planet hunter at TNG*, **Proc. SPIE** 8446, Ground-based and Airborne Instrumentation for Astronomy, 84461V (2012).

List of Corrections

I thank the examiners for their valuable comments. I have revised the thesis on the suggested lines and addressed the concerns raised by the reviewers. Following are the list of corrections made in the thesis.

Second Examiner comments:

1. Comment: My main concern is that for the FP, the FSR should be 3-4 times the FWHM, from Fig.5.22 - Fig.5.24, it is less than this. Before installing the calibrator to the spectrograph, improvement should be made.

   Reply: This is a valid concern and the suggestion will be taken into account. We will be using a new Fabry-Perot etalon for the final installation on the spectrograph/telescope.

2. Page 55, Chapter 4, Section 4.4.4. Comment: The sentence "An average reflectivity of 60% was selected because a high reflectivity coating(>90%) produces narrow line-width, leading to the inadequate sampling of FP lines on the CCD" From my understanding, in the spectrograph design, the CCD could resolve the spectra line determined by the PSF, the FP should produce narrow line-width, ideally the delta function.

   Reply: In page 55, the sentence "An average reflectivity of 60% was selected because a high reflectivity coating(>90%) produces narrow line-width, leading to the inadequate sampling of FP lines on the CCD" is replaced by "Although the high reflectivity coating(>90%) can produce narrow lines, an average reflectivity of 60% was selected to ensure a uniform response of the FP over the desired wavelength range of the spectrograph (400-750 nm)" to address the referee's comment.

3. Page 9, Fig.1.5. FP calibration spectra taken with HESP. Comment: If I'm writing the thesis, I would like to use the spectra taken from other spectrograph as an example.

   Reply: As per the suggestion by the referee, the FP calibration spectra

taken with HESP is replaced by FP calibration spectra taken with HARPS spectrograph. A relevant caption has been added along with a new reference (Cosentino *et al.*, 2012) for the figure.

4. Cover page. Comment: Check the date November 2021

Reply: Since the thesis was submitted to the University in November 2021, the month and year of submission has been mentioned on the cover as it is. However, the month of submission (November) has been removed from the cover page as per University guidelines.